Abstract

This Ph.D thesis encompasses a global numerical simulation of the needle-eye float zone process, used to grow silicon single crystals. The numerical models includes coupled electromagnetic and free surface models and a global heat transfer model, with moving boundaries. An axisymmetric fluid flow model, including centrifugal, buoyancy, thermocapillary and electromagnetic forces, is used to determine flow field, after the phase boundaries have been determined, by the heat transfer model. A finite element model for calculating dopant transport, using the calculated unsteady flow field, has been developed within this project. This model has furthermore been expanded to two equations coupled by a non-zero right hand side, for simulating transport of point defects in the crystal during growth.

Free surface shapes and induced electric surface current are calculated for two different 4" configurations and a 0.8" configuration. The heat transfer calculations of the same three configurations, yields the global temperature field, from which temperature gradients are determined. The heat transfer model is furthermore expanded to study convective cooling of the crystal from natural convection in the pressurized surrounding gas, for one of the 4" configurations. The depth of the lower phase boundaries of both 4" configurations have with good agreement to the calculations been measured, to provide experimental verification of the heat transfer model.

Calculations of melt convection within the floating zone is done for the two 4" configurations, for four different setups. The flow is unsteady, but laminar and is seen to be repressed by increased rates of rotation. Gas doping is simulated by prescribing a flux of dopant through the free surface, resulting in unsteady dopant concentration fields, with distinct concentration boundary layers at the lower phase boundaries. The dopant concentrations, at the lower phase boundaries, are used to determine radial resistivity profiles, which with fair agreement are compared to measurements.

Simulations of defect transport are conducted for both of the 4", as well as the 0.8" configuration, for two different values of the recombination factor. The calculation of the 0.8" crystal is compared to DLTS measurements, revealing good agreement for one of the recombination factors, which however does not fit the Voronkov theory. Both factors are used in the simulation of the two 4" configurations, which both have so high growth parameters, that the vacancy domination is relatively unaffected by the recombination.

Abstract (in danish)

Denne Ph.D afhandling indeholder en global numerisk simulering af needle-eye float zone processen, til dyrkning af silicium énkrystaller. De numeriske modeller inkluderer en koblet elektromagnetisk og fri væskeoverflade model, samt en global varmetransmissions model, med bevægelige rande. En aksesymmetrisk strømningsmodel indenholdende, centrifugal, opdrifts, termocapillare og elektromagnetiske kræfter, anvendes til at bestemme strømningsfeltet, efter at fasegrænserne er bestemt af varmetransmissions modellen. En finite element model til at beregne transport af doterstof, udfra det beregnede instationære strømningsfelt, er udviklet i dette projekt. Denne model er ydermere udvidet til to ligninger koblet af højresiden, for at simulere transport af punkt defekter i krystallen under dyrkning.

Formen af frie væskeoverflader og inducerede elektriske overflade strømme er beregnet for to forskellige 4" konfigurationer og en 0.8" konfiguration. Varmetransmissions beregninger af de samme tre konfigurationer giver et globalt temperaturfelt, hvorfra temperaturgradienter bestemmes. Varmetransmissions modellen er ydermere udvidet, for at studere konvektiv køling af krystallen forsaget af naturlig konvektion i dyrkningskammerets tryksatte atmosfære, for en af 4" konfigurationerne. Dybden af den nedre fasegrænse for begge 4" konfigurationer er med god overensstemmelse målt, for at give eksperimentel verifikation af varmetransmissions modellen.

Beregninger af smelte strøming i den flydende zone er udført for de to 4" konfigurationer, i fire forskellige opsætninger. Strømingen er instationær, men laminar og ses undertrykt af øget rotation. Gasdotering simuleres ved at foreskrive en flux af doterstof gennem den frie overflade, resulterende i instationære doterstof koncentrationsfordelinger, med tydelige koncentrations grænselag ved ned de nedre fasegrænser. Doterstof koncentrationerne ved de nedre fasegrænser, anvendes til at bestemme radialle resistivitetsprofiler, som med rimelig overenstemmelse er sammenlignet med målinger.

Simuleringer af defekt transport er gennemført for begge 4" samt 0.8" konfigurationen, for to forskellige værdier af rekombinationsfaktoren. Beregningen for 0.8" krystallen er sammenlignet med DLTS målinger, med god overensstemmelse for én af rekombinationsfaktorene, denne beregning passer dog ikke med Voronkov teorien. Begge faktore anvendes i simuleringen af de to 4" konfigurationer, som begge har så høje dyrkningsparametre, at vacancy domineringen er relativt uberørt af rekombinationen.

Preface

This Ph.D project has been carried out as an industrial Ph.D project, administrated by the Danish Academy of Technical Sciences (ATV) and financially supported by the Danish Agency for Trade and Industry under the Ministry of Business and Industry. The project has been carried out in the period from august 1. 1997 to august 1. 2000, with the following partners

University:

Department of Mathematical Modelling (IMM)
Building 321
Technical University of Denmark (DTU).
2800 Kgs. Lyngby, Denmark
`www.imm.dtu.dk`
Represented by: Associate Professor Mads Peter Sørensen (main advisor)

Industry:

Topsil Semiconductor Materials A/S
Linderupvej 4, P.O. Box 93
3600 Frederikssund, Denmark
`www.topsil.com`
Represented by: R&D Manager Leif Jensen

Third party:

Mikroelectronik Centret (MIC)
Building 345 east
Technical University of Denmark (DTU).
2800 Kgs. Lyngby, Denmark
`www.mic.dtu.dk`
Represented by: Associate Professor Ole Hansen

Acknowledgements

The completion of this Ph.D thesis and the work behind it, has been assisted by many individuals, for whose support I am grateful. First of all I would like to thank my main adviser Mads Peter Sørensen, at the Department of Mathematical Modelling (IMM), for making the project possible and for always taking the time to listen to my problems and results. My adviser at Topsil, Leif Jensen, has shown an untiring enthusiasm and through numerous discussions, he has made sure that the computations were not too far off the reality they tried to simulate. Also at Topsil I would like to thank Anne Nielsen, for always having the ability to tell me if a configuration or result was feasible, or what I had to do to make it so, and furthermore Jan Vedde for some fruitful theoretical discussions.

During this project I have stayed two months at the Institute of Crystal Growth (IKZ) in Berlin and ever since I have had a very fruitful cooperation. At IKZ, I am truly grateful for the help and support I have received from Anke Lüdge, without whom this thesis never would have been written. Thanks are also due to Helge Riemann for bringing me up to speed with the physics of the float zone process and for the pleasant company that he, Anke and the rest of the group provided during my visits in Berlin. Special thanks also goes to Klaus Böttcher for helping to solve some of the early numerical problems. Finally from Berlin I would also like to thank H. Lemke for sharing some of his knowledge on defects and providing experimental data for comparison.

At the Institute of Electroheat in Hannover, I would like to thank Andris Muiznieks and Georg Raming for their help and support in finding the errors in the first versions of the software delivered from Cape Simulations, but also for their invaluable advise, in the development of the FEM-CD finite element code. In the development of FEM-CD, I would also like to thank Vincent Allan Barker at IMM for teaching me the basics of finite element modelling and encouraging me to carry on. For advice in the implementation of the upwind scheme in FEM-CD, I would like to thank James G. Rice of the Virginia Commonwealth University. For good cooperation and support of the MHAC and FZ-Sim codes, I would finally like to thank Ani Worlikar, Ljubomir Vujisic and Shari Motakef at Cape Simulations Inc. in Boston.

Contents

Chapter 1

Introduction

This first chapter provides an introduction and broader view of the topics of this thesis. First the specific physical characteristics and terminology of the float zone process is introduced in section 1.1. Section 1.2, thereafter, goes more into detail with the numerical simulation of the process, giving a brief literature survey of what has been done in this field up till now. Finally this being an industrial Ph.D project, section 1.3 focuses on the commercial aspects of the numerical simulations, which insights can be gained and how that may affect the industrial partner, Topsil Semiconductor Materials A/S.

Before going through the details of the float zone process and the numerical modelling, an overview of the structure of this thesis is given. Chapter 2 provides the mathematical modelling and theoretical basis of the applied numerical models. The implementation of these models and how they are interconnected is discussed in chapter 3, along with the details on the derivation of the developed finite element model.

The first chapter to include simulation results is chapter 4, dealing with the solution of the connected electromagnetic and free surface models, as well as the heat transfer. The solution of the heat transfer problem is the temperature field and the shape of the phase boundaries, which are compared with experiments. Finally chapter 4 also includes a study of the convective cooling of the crystal, caused by natural convection of the ambient gas in the growth champer.

Chapter 5 gives simulations of melt convection, starting with simulations of the effects of the isolated driving forces and moving on to the unsteady flow field of the molten zone.

Figure 1.1. *Photograph of the IKZ 4" float zone process with courtesy of IKZ.*

Connected to melt convection is the transport of dopant, which is also described in this chapter. Experimental comparison is given through calculated and measured resistivity profiles.

The last chapter on results, is on transport of point defects. Simulations of a thin 0.8" crystal are in chapter 6 compared with DLTS measurements for two different recombination factors found in the literature. The model is then applied to thicker 4" crystals, to show defect distributions throughout the crystal during growth. Finally a conclusion and three appendices on physical parameters, dimension analysis and stability and robustness of the numerical models completes the thesis.

1.1 The float zone process

Silicon single crystals are industrially grown from poly crystalline silicon using two different techniques, Czochralski (CZ) and the float zone (FZ). With the CZ technique, the crystal is grown out of a quartz crucible, whereas the FZ crystal is grown without any physical contact, except for the ultra clean atmosphere in the growth chamber, see figure 1.1. One of the important differences between CZ and FZ crystals is therefore a larger oxygen content in the

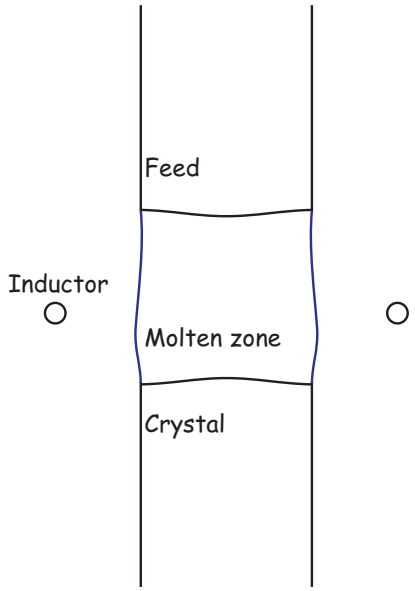

Figure 1.2. *The classical float zone layout.*

CZ crystals, coming from the crucible. The CZ technique accounts for approximately 90% of the world marked of silicon crystals, mainly used for memory chips and other integrated circuits, the remaining 10% are FZ crystals used for power applications and sensors. A comprehensive examination of the float zone process can be found in [25, 30].

The float zone process, which was first patented in 1952 by Theuerer, includes two fundamentally different configurations, the classical, which can be used to grow crystals up to about 2" in diameter, and the needle-eye technique for larger crystals. Silicon crystals are at present industrially grown at diameters up to 6", weighing more than 35 kg. The classical layout, shown in figure 1.2, is no suitable for growing larger diameter crystals, because it is not possible for the heat to keep the thicker floating zone molten all the way through to the core. The classical layout is, however, interesting because of the simpler geometry, which has also made it the object of study for the majority of numerical simulations.

Small diameter silicon crystals are at present not commercially interesting, so the focus of this thesis is on the needle-eye technique, for which the general layout is shown in figure 1.3. Characteristic for the needle-eye technique is that the poly crystalline feed rod is melted by a radio frequency AC-current in an inductor, with a center hole smaller then the diameter of the feed, hence the name – needle-eye.

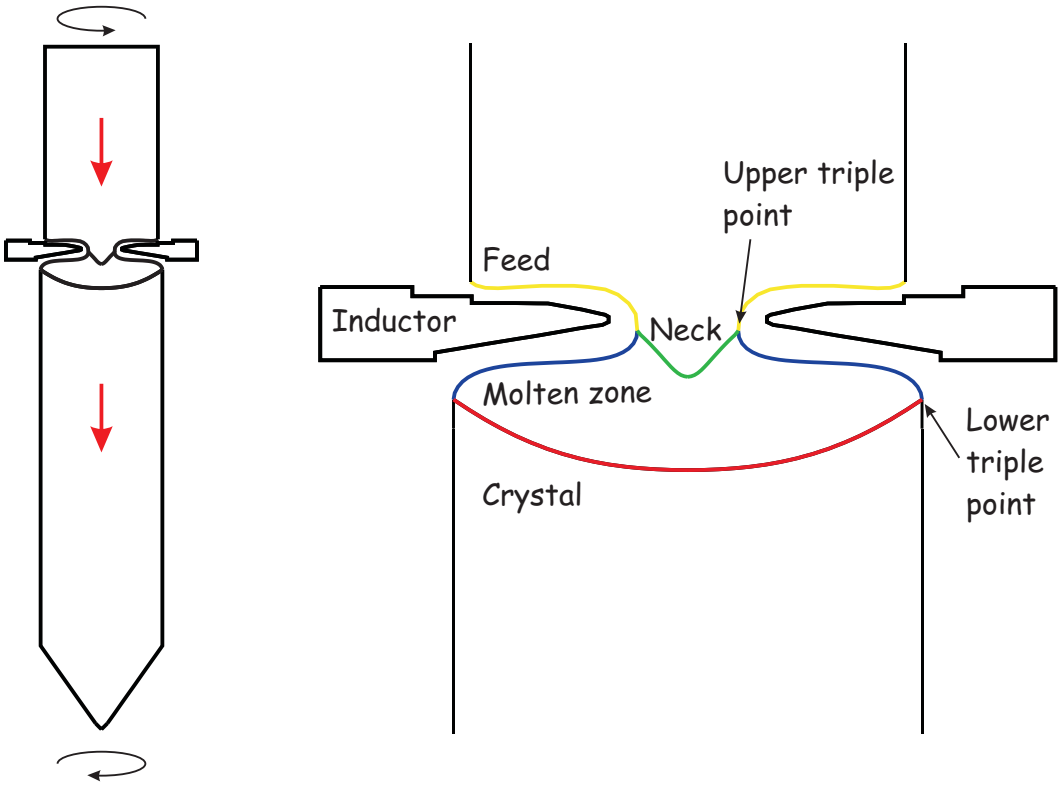

Figure 1.3. *The float zone layout for the needle-eye technique. Melt front (yellow), upper phase boundary (green), free surface (blue) and lower phase boundary (red).*

The *startup of the process* is done by placing a droplet from the tip of the conical end of the feed on a thin seed of single crystal with the desired crystal orientation. At the startup the molten zone is therefore only made up of the droplet, but by adjusting the pull speed of the crystal and feed, the volume of the molten zone and thereby also the diameter of the growing crystal can be increased. To produce dislocation free crystals one must, however, grow 10 - 15 cm thin crystal before increasing the diameter.

When the process is at the desired diameter, the geometry of the molten zone remains almost constant. It is at a steady state, where a constant amount of material melts of the feed and solidifies as crystal. At this stage of the process, the geometry is characterized, by a melt front, where a film of molten silicon slowly flows down to the free surface and there enters the molten zone. The feed is separated from the molten zone by the upper phase boundary, shaped by the heat transfer process. The free surface extends from the lower triple point at the crystal to the upper triple point at the melt front, and is held by surface

tension and an electromagnetic force from the inductor. Finally at the bottom, the molten zone is separated from the crystal by the lower phase boundary. The inductor shown in figure 1.3 is rotational symmetric, but the real inductor must of course have a gap, giving a asymmetric heat input. To minimize the asymmetry and control the flow of the melt, the feed and crystal are counter rotated.

To alter the resistivity of the grown crystal a dopant can be added during growth, most common are phosphorus and boron for N- and P-type, respectively. The dopant can be supplied to the feed prior to the FZ process or added with gas phase doping through the free surface. The distribution of dopant depends on the dynamical flow field in the molten zone and is studied in this thesis.

1.2 Numerical simulation of the float zone process

This section includes a literature survey of some of the important contributions to this field up till now. The survey is not intended to be comprehensive, but is included to give some background for the simulations and models presented in this thesis.

As described in the previous section, the process, and therefore also the numerical modelling, is quite complex. A global modelling of the needle-eye configuration must include several models. A model of the interaction between the free surface and the electromagnetic field generated by the inductor, a global heat transfer model, capable of determining the shape of the phase boundaries and a flow model including transport of dopant. Crystal defects is furthermore a field of increasing interest for the float zone process, so a model for simulating defect transport would also be valuable. The detailed description of the models, used in this thesis, is given in chapter 2, but an overview of the models and their connections can be seen in figure 2.1, page 10.

In a literature survey concerning numerical modelling of the float zone process, one group, from the Institute for Electroheat in Hannover should first be mentioned. They have developed models for simulating the entire process in the needle-eye configuration, except defect modelling. Their work, where many of the simulations have been experimentally supported by The Institute of Crystal Growth (IKZ) in Berlin, has been published in [46, 52–58, 64, 66, 85].

Global modelling of the float zone process is as described, comprised of several models for the different physical situations encountered in the process. Numerical simulations of the float zone process includes models of the free surface shape for the classical FZ configuration, see figure 1.2, where the basic Laplace-Young equation is derived [14, 75]. The stability of the free surface in a classical layout is investigated through a perturbation analysis in [81]. In the needle-eye configuration the heating is done by a radio frequency magnetic field, generating an electric surface current, that in the magnetic field contributes with a normal electromagnetic force. The shape of the free surface in the for the needle-eye configuration including the normal electromagnetic for has been calculated in [45].

In calculations of heat transfer, the shape of the phase boundaries depend on the convective heat transfer from the bulk motion of the crystal and feed and on the release of latent enthalpy. The shape of the phase boundaries is therefore an integral part of the heat transfer simulations, which can be handled by applying moving boundaries [34, 58, 65, 76].

Heat transfer calculations are the input to convection calculations, where a starting point is just to consider isolated Marangoni convection, as has been done in [12, 13, 32, 89]. The historical reason for simulating isolated Marangoni convection is, that it is the strongest driving force for the early developed thin crystals in the classical configuration [15]. Thin crystals have been grown in micro gravity (in space), to investigate growth without the influence of gravity [31, 36]. Investigation on the stability of the Marangoni convection in the classical layout, in the form of bifurcation analysis, has been conducted in [42–44].

Calculations of melt convection including all driving forces for the needle-eye configuration, result in laminar, but depending on the individual process sometimes unsteady flow. The general flow pattern is two counter rotating vortices, with instabilities and individual properties depending on the specific process [4, 57, 84, 85]. In trying to control the melt convection magnetic fields have been applied. For the classical configuration studies of the influence of DC magnetic fields are presented in [50, 51], whereas AC fields were applied in [15]. The needle-eye configuration with both DC and AC magnetic fields was studied in [64].

Calculations of melt convection are of interest, because melt convection govern the distribution of dopant at the lower phase boundary and therefore also the dopant incorporated in the crystal. Beside the Hannover group, who in cooperation with IKZ have made several contributions to this field [46, 56, 57, 64], the influence on dopant distribution has been

studied in [35, 37, 84]. The influence from crystal orientation on the segregation process, through a model of the undercooling, was studied in [28].

Three-dimensional studies of fluid flow and dopant transport is naturally a compromise with respect to numerical accuracy, because the extra dimension implies a coarser mesh. These studies, however, have the potential to investigate phenomena that are not rotational symmetric, as done in [66, 67].

The field of numerical models for defect transport started out for the Czochralski process, but according to the theory of Voronkov[1] [86], the generation and transport of defects should be similar for the float zone process. Numerical simulations of defect transport for the CZ process have been conducted in [8, 17, 78]. One of the first important experimental contributions to defects in float zone material is [1], supporting the Voronkov theory that temperature gradients are crucial to the generation of defects. More recent contributions to defects in float zone crystals, where analytical calculations are compared with DLTS measurements, are given in [40, 41].

1.3 Commercial aspects of numerical simulation

This industrial Ph.D project is a cooperation between the Department of Mathematical Modelling (IMM) at The Technical University of Denmark and Topsil Semiconductor Materials A/S, with the Microelectronics Center (MIC) as third party. The project therefore has a commercial aim as well as an academic.

One of the objectives of the project is to develop numerical models, that can be used as tools for the research and development at Topsil. The advantage of such a tool over development using experiments alone, comes through various experimental limitations. It has in the literature been established, that the distribution of dopant in the crystal is dependent on the flow within the molten zone. Molten silicon is, however, opaque and very hot, so experimental investigations of flow patterns are virtually impossible. Experimental limitations also applies to the vitally important temperature field, because high temperatures and high temperature gradients on the surface of the crystal are hard to measure precisely. Furthermore, surface temperature measurements gives no information on the temperature in the

[1] The Voronkov theory will be dealt with in section 6.1, page 77.

center of the crystal, at least not without some calculation. Finally in the field of crystal defects measurements are likewise very limited and can therefore also be by complemented simulations.

In developing new or improved processes, one of the most important objectives is a low radial variation of the incorporated dopant. In the traditional experimental development, however, one has to grow a *single crystal*, in order to measure a resistivity profile. Experimental expenses are therefore large, because one might have to grow 3 crystals, with a new a promising configuration, before obtaining the measurement, that quantifies whether the configuration is an improvement. The experimental difficulties of obtaining a single crystal, are of course not encountered in the numerical simulation.

Another objective of the work is to gain physical insight of the mechanisms governing the growth process. It is needless to say that physical insight is required for qualified invention, the more knowledge, the more ideas can be rule out, before making any experiments. If the number of experiments required to develop a new product can be reduced, then there is both money and time to save. The expense of the experiments is furthermore increasing with the diameter of the crystal, because more material is required, do future experimental expenses are expected to rise.

As shall be shown in this thesis the numerical modelling can, however, at least at the present state not stand alone. It must be complemented by the traditional experimental development, but it can be used to aid, getting and trying out new ideas, to optimize existing processes and to reduce the number of required experiments.

Chapter 2

Mathematical Models

This chapter describes the different models applied in the numerical simulations. The models are implemented in three different software packages, FZ-Sim, MHAC and FEM-CD, where the first two are commercially available from Cape Simulations Inc. [10, 11] and FEM-CD is developed within this project.

The global modelling of the FZ process is divided into smaller steps, which will be described individually in this chapter. FZ-Sim is made up of models for the electromagnetic field, the free surface and the global heat transfer of the process. With the phase boundaries determined by FZ-Sim, the time-dependent flow of molten silicon is calculated using the second commercial program MHAC. Finally the velocity field from MHAC is used as input to FEM-CD for determining dopant distributions.

The simulation of point defect transport in the single crystal is governed by two coupled transport equations. The general convection-diffusion solver FEM-CD is therefore modified to handle two coupled transport equations, allowing simulation of transport and recombination of interstitial and vacancy type point defects. Figure 2.1 shows how the models are connected to form the simulation.

The following sections describes the physical equations and boundary conditions as well as the assumptions of the individual models, whereas the numerics and implementation of the models is dealt with in chapter 3.

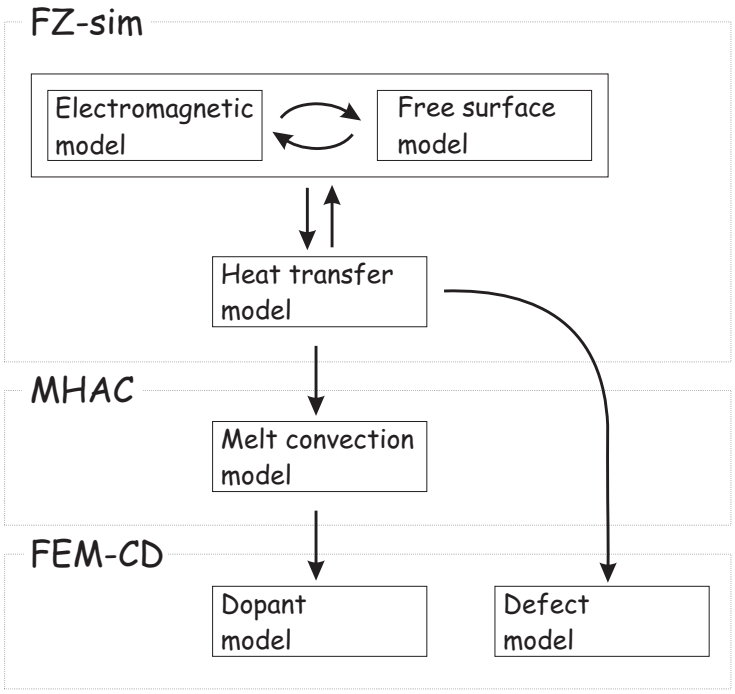

Figure 2.1. *Connection between the different models and software packages.*

2.1 Electromagnetic

The energy to melt the silicon from the feed is provided by an inductor. The purpose of the electromagnetic model is to calculate the heating and the electromagnetic force normal to the free surface. The inductor is powered by an AC-current with a frequency of $\omega = 2 - 3\,\mathrm{MHz}$, resulting in a low penetration depth δ_{el} of the electromagnetic field in the silicon. The penetration depth is given by (2.1)

$$\delta_{el} = \sqrt{\frac{1}{\pi \omega \sigma_l \mu_0}} \tag{2.1}$$

where ω is the applied frequency of the field, σ_l is the electrical conductivity of molten silicon and μ_0 is the vacuum permeability [25].

The Maxwell equations (2.2a–2.2c) and Ohm's law (2.2d) [69], governing the electromagnetic and electric fields, are solved for the domain between the coil and the free surface, resulting in the distribution of the electromagnetic force and inductive heating at the free surface of the molten silicon, see figure 2.2

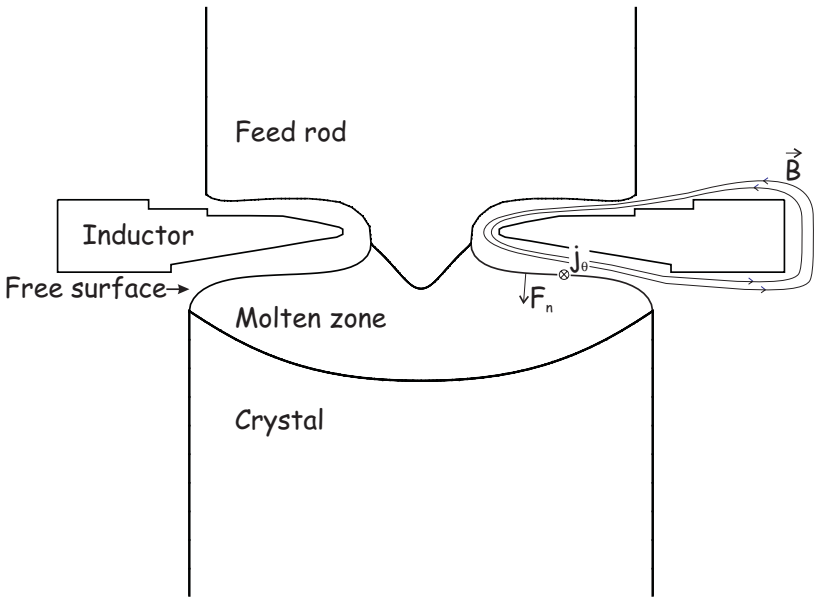

Figure 2.2. *Electromagnetic $\vec{B}$ and electric fields $\vec{E}$. Azimuthal current J_θ and normal electromagnetic force F_n.*

$$\vec{\nabla} \times \vec{E} = -\frac{\partial \vec{B}}{\partial t} \tag{2.2a}$$

$$\vec{\nabla} \times \vec{B} = \mu_0 \vec{j} \tag{2.2b}$$

$$\vec{\nabla} \cdot \vec{B} = 0 \tag{2.2c}$$

$$\vec{j} = \sigma \vec{E} \tag{2.2d}$$

$\vec{B} = (B_r, B_\theta, B_z)$ is the electromagnetic field, $\vec{E} = (E_r, E_\theta, E_z)$ is the electric field, t is time and $\vec{j} = (J_r, J_\theta, J_z)$ is the electric current on the free surface. The equations are solved as in [45], by introducing an electric potential ϕ and a magnetic vector potential $\vec{A} = (A_r, A_\theta, A_z)$, so that

$$\vec{E} = -\vec{\nabla}\phi - \frac{\partial \vec{A}}{\partial t} \tag{2.3}$$

$$\vec{B} = \vec{\nabla} \times \vec{A} \tag{2.4}$$

In assuming rotational symmetry, the electromagnetic field only has nonzero radial and axial components (B_r and B_z) and the electric field has only a nonzero azimuthal component

E_θ [45]. The quantities are non-dimensionalized as follows

$$\begin{aligned}
\tilde{B}_r &= \frac{B_r}{V_0/\omega R_{crystal}^2} & \tilde{B}_z &= \frac{B_z}{V_0/\omega R_{crystal}^2} \\
\tilde{E}_\theta &= \frac{E_\theta}{V_0/R_{crystal}} & \tilde{\phi} &= \frac{\phi}{V_0} \\
\tilde{A}_\theta &= \frac{A_\theta}{V_0/\omega R_{crystal}} & \tilde{r} &= \frac{r}{R_{crystal}} \\
\tilde{z} &= \frac{z}{R_{crystal}} & \tilde{R} &= \frac{R}{R_{crystal}} \\
\tilde{Z} &= \frac{Z}{R_{crystal}} & \tilde{s} &= \frac{s}{R_{crystal}}
\end{aligned} \tag{2.5}$$

where $R_{crystal}$ is the radius of the crystal and V_0 is a reference potential. The surface of the melt is parametricly described by $r = R(s)$ and $z = Z(s)$, see figure 2.3.

In the further modelling the *tildes will be omitted.*

In cylindrical coordinates the electromagnetic and electric fields as functions of ϕ and $\vec{A}$ are [80]

$$B_r = -\frac{\partial A_\theta}{\partial z} \tag{2.6a}$$

$$B_z = \frac{1}{r}\frac{\partial}{\partial r}(rA_\theta) \tag{2.6b}$$

$$E_\theta = \frac{1}{r}\frac{\partial \phi}{\partial \theta} - \frac{\partial A_\theta}{\partial t} \tag{2.6c}$$

Applying an AC-voltage in the induction coil of the form $V_0 \sin \omega t$ leads to the following solution $A_\theta(r, z)$ in the electrically insulating atmosphere [45]

$$A_\theta = \frac{1}{\pi}\cos \omega t \int J_\theta(s)\sqrt{\frac{R}{mr}}\left[K(m) - E(m)\right] ds \tag{2.7a}$$

$$m = \left[1 - (1-k^2)^{1/2}\right]\left[1 + (1-k^2)^{1/2}\right]^{-1} \tag{2.7b}$$

$$k^2 = 4rR\left[(R+r)^2 + (Z-z)^2\right]^{-1} \tag{2.7c}$$

where K and E are complete elliptical integrals and $J_\theta(s)$ is the azimuthal component of the surface current as function of the position s, see figure 2.3.

The solution *inside* the coil and molten silicon are

$$\text{Coil} \qquad A_\theta = \frac{1}{2\pi}\cos\omega t \tag{2.8a}$$

$$\text{Silicon} \qquad A_\theta = 0 \tag{2.8b}$$

Since A_θ is continuous, (2.7) must attain the same value on the surface of the coil as (2.8a) and the same value on the surface of the molten silicon as (2.8b). This provides the integral equation that can be solved for the azimuthal current distribution $J_\theta(s)$.

Once $J_\theta(s)$ is determined, the induced joulean heating $q_{joulean}$ and the electromagnetic force F_n on the free surface of the molten silicon can be calculated as

$$q_{joulean} = \frac{1}{2}\sqrt{\frac{\mu\omega}{2\sigma}}\left(J_\theta^2\right) \tag{2.9}$$

$$F_n = \frac{\mu_0 J_\theta^2}{4\pi^2} \tag{2.10}$$

where subscript n refers to normal direction.

The electromagnetic model is therefore, in summary, based on an assumption on rotational symmetry, which is naturally not true for a real inductor since it must have a gap. The influence on the symmetry has, for a narrow gap ($< 1\,\text{mm}$), however, been shown to be small [72]. Furthermore would the inclusion of the gap, require a three-dimensional model as in [67]. Finally is the frequency assumed high enough to neglected the finite depth of the skinlayer (2.1), see figure A.2 page 108.

2.2 Free surface

The shape of the free surface of the melt is connected to the electromagnetic model because the Joulean heating and the normal electromagnetic force depends on the distance to the coil. The shape is determined by the Laplace-Young equation (2.11), which is a force balance of pressure, surface tension and the induced electromagnetic force in normal direction [45, 69]. The electromagnetic force is averaged over time, since the free surface shape cannot respond to the high frequency

$$P - \rho g z + F_n = \gamma K \tag{2.11}$$

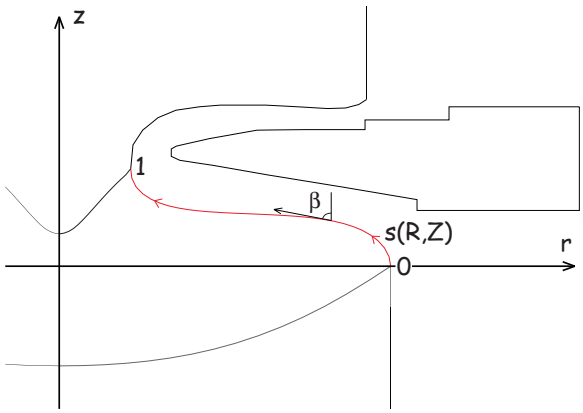

Figure 2.3. *The parametric description of the free surface* $(R(s), Z(s))$ *by dimensionless parameter* s. $\beta(s)$ *is the local angle to vertical.*

where F_n is the electromagnetic force in normal direction, K is the curvature and γ is the surface tension, making the right hand side the surface tension force. $\rho g z$ is the static pressure and P is the pressure difference between the melt and the surrounding gas. The dynamic pressure from the motion of the melt, is negligible compared to the hydrostatic pressure, because of the low velocities [45]. Furthermore is the centrifugal forces from the rotation of the crystal neglected, because of a vanishing Rotational Bond number, see the dimensional analysis in appendix B.

The shape of the free surface is parametricly described by $R(s)$, $Z(s)$ and $\beta(s)$, where s is the dimensionless distance along the free surface, starting at the crystal/melt/atmosphere tri-junction and $\beta(s)$ is the local free surface angle to vertical, see figure 2.3. The parametric description gives the following differential equations [45]

$$\frac{dR}{ds} = \sin\beta \tag{2.12a}$$

$$\frac{dZ}{ds} = \cos\beta \tag{2.12b}$$

$$\frac{d\beta}{ds} = \frac{\cos\beta}{\tilde{R}} + Bo\tilde{Z} + Bo_\epsilon \tilde{J}_\theta^2 - P_0 \tag{2.12c}$$

where P_0 is P non-dimensionlized by $\gamma/R_{crystal}$ and $\tilde{J}_\theta$ is J_θ non-dimensionalized by $2\pi I_0/R_{crystal}$. I_0 is the current in the inductor. Bo and Bo_ϵ are the Bond number and the electromagnetic Bond number, respectively, see appendix B page 109.

The shape of the free surface is therefore, in summary, assumed to be rotational symmetric and independent of dynamic pressure and centrifugal forces.

2.3 Heat transfer

The calculation of heat transfer determines the temperature field in the solid and liquid silicon, as well as the position and shape of the upper and lower phase boundary. The later inclusion of the melt flow does disturb the temperature field in the molten zone, but due to the low Prandtl number ($Pr = 0.013$) the influence on the shape of the phase boundaries is negligible.

The shape of the melt front, see figure 1.3 page 4, is predetermined and the temperature at the melt front is set to melting point. In the real process this boundary is dependent on the state of the process and it might change somewhat during the growth. However, this simplification seems reasonable since it has little impact on the phase boundaries and the temperature field of the crystal, which is of main interest.

The heat transfer is described by (2.13)

$$\rho c_p \, v_z \cdot \vec{\nabla} T = \vec{\nabla} \cdot (\lambda \vec{\nabla} T) \tag{2.13}$$

where v_z is the pull speed of feed and crystal, respectively, ρ the density, c_p the specific heat, k the heat conductivity and the absolute temperature is denoted T.

The *boundary condition* (2.14) is the usual radiative loss, which is used from outer surfaces, except the melt front and the free surface

$$q = \epsilon\sigma \left(T^4 - T_\infty^4\right) \tag{2.14}$$

here q is an outward energy flux, ϵ is the temperature-dependent emissivity and σ is the Stefan-Boltzman constant. On the free surface, some of the radiation is reflected by the nearby inductor. This is modelled by an emperical effective temperature T_{eff} [85]. This boundary condition (2.15) is furthermore comprised of a joulean heat input from the inductor $q_{joulean}$, through the free surface

$$q = \epsilon\sigma \left(T^4 - T_{\mathit{eff}}^4\right) - q_{joulean} \tag{2.15}$$

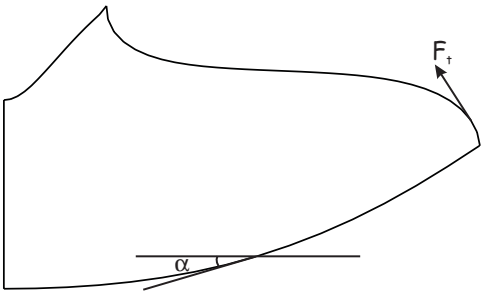

Figure 2.4. *Angle of interface to horizontal α. Direction of tangential electromagnetic force F_t.*

As previously mentioned, the melt front is given a presumed shape and fixed at melting point temperature. This is of course an assumption, but since the shape of the melt front can be determined with good accuracy from photographs and it only influences the temperature field in the feed rod, which is not the main interest, it is acceptable.

Finally there is a release of latent heat at the lower phase boundary (2.16a) and an absorption at the upper (2.16b)

$$q_{released} = \rho V_{crystal} \ell \cos\alpha \tag{2.16a}$$

$$q_{absorbed} = \rho V_{feed} \ell \cos\alpha \tag{2.16b}$$

where α is the local angle of the phase boundary to horizontal, insuring that a constant amount of latent heat is absorbed and released independent of the curvature of the phase boundaries, see figure 2.4. ℓ is the latent enthalpy of the phase shift. $V_{crystal}$ and V_{feed} are the growth or pull velocities of the crystal and feed respectively. Conservation of mass gives the following relation between the pull velocities

$$V_{feed} = \frac{R_{crystal}^2}{R_{feed}^2} V_{crystal} \tag{2.17}$$

The values of all the physical parameters are given in appendix A, page 105.

The heat transfer model for determining the temperature field and the shape of the phase boundaries, is based on the assumption that the influence from the melt convection on the shape of the phase boundaries is negligible, by setting flow velocities to zero. Furthermore the modelling of the radiation reflected by the inductor is based on an effective temperature (2.15). Finally the model is quasi stationary, in assuming constant growth of crystal and constant melt off from feed rod, i.e. no facet growth.

2.4 Melt convection

The melt flow is governed by conservation of mass and momentum, as stated in the continuity equation (2.18) and the Navier-Stokes equations (2.19)

$$\vec{\nabla} \cdot (\rho \vec{V}) = 0 \tag{2.18}$$

$$\frac{\partial \vec{V}}{\partial t} + \vec{V} \cdot \vec{\nabla} \vec{V} = -\frac{1}{\rho} \vec{\nabla} p + \nu \nabla^2 \vec{V} + \vec{g} \beta \Delta T \tag{2.19}$$

where pressure is denoted p, β is thermal expansion and the gravity vector is given by $\vec{g} = (0, 0, -g)$. The model is axisymmetric, laminar, incompressible, but unsteady. Using cylindrical coordinates and the axisymmetric assumption the continuity equation (2.18) transforms into [87]

$$\frac{1}{r} \frac{\partial}{\partial r} (r v_r) + \frac{\partial v_z}{\partial z} = 0 \tag{2.20}$$

where the components of the velocity vector is $\vec{V} = (v_r, v_\theta, v_z)$. Similarly the compact form of the Navier-Stokes (2.19) transforms into (2.21)

$$\frac{\partial v_r}{\partial t} + v_r \frac{\partial v_r}{\partial r} + v_z \frac{\partial v_r}{\partial z} - \frac{1}{r} v_\theta^2 = -\frac{1}{\rho} \frac{\partial p}{\partial r} + \nu \left[\frac{1}{r} \frac{\partial}{\partial r} \left(r \frac{\partial v_r}{\partial r} \right) + \frac{\partial^2 v_r}{\partial z^2} - \frac{v_r}{r^2} \right] \tag{2.21a}$$

$$\frac{\partial v_\theta}{\partial t} + v_r \frac{\partial v_\theta}{\partial r} + v_z \frac{\partial v_\theta}{\partial z} - \frac{v_r v_\theta}{r} = \nu \left[\frac{1}{r} \frac{\partial}{\partial r} \left(r \frac{\partial v_\theta}{\partial r} \right) + \frac{\partial^2 v_\theta}{\partial z^2} - \frac{v_\theta}{r^2} \right] \tag{2.21b}$$

$$\frac{\partial v_z}{\partial t} + v_r \frac{\partial v_z}{\partial r} + v_z \frac{\partial v_z}{\partial z} = -\frac{1}{\rho} \frac{\partial p}{\partial z} - g + \nu \left[\frac{1}{r} \frac{\partial}{\partial r} \left(r \frac{\partial v_z}{\partial r} \right) + \frac{\partial^2 v_z}{\partial z^2} \right] \tag{2.21c}$$

for the r, θ and z directions respectively.

Four driving forces controls the flow:

- Buoyancy forces (natural convection)
- Thermocapillary forces (Marangoni convection)
- Tangential electromagnetic force (electrodynamic convection)
- Centrifugal forces (rotation)

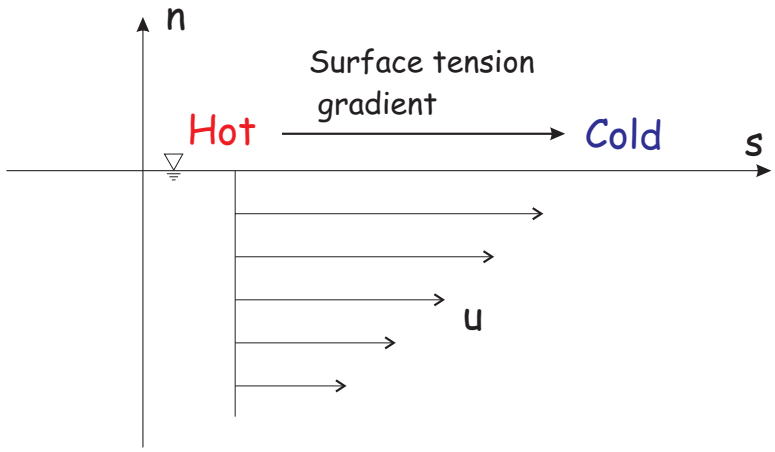

Figure 2.5. *Marangoni convection, drives a surface flow from warmer towards colder areas of the free surface* ($\frac{\partial \gamma}{\partial T} < 0$).

The *natural convection* is driven by buoyancy forces present because of temperature differences within the molten zone and modelled through the body force term $-g$ in (2.21c) and a linear temperature dependence of the density on temperature (2.22)

$$\rho = \rho_0 \beta (T - T_0) \tag{2.22}$$

The *Marangoni* or thermocapillar force τ (2.23) is a surface force that comes from the temperature dependence for the surface tension γ [42]

$$\tau = \mu \frac{\partial u_s}{\partial n} = \frac{\partial \gamma}{\partial T} \frac{\partial T}{\partial s} \tag{2.23}$$

where s is the coordinate along the free surface, see figure 2.3. The Marangoni effect is therefore dynamically dependent on the temperature field, which is part of the solution. The isolated Marangoni effect described by (2.23) is shown on figure 2.5, the temperature gradient results in a shear force driving the flow.

The *tangential electromagnetic force* F_t is caused by the azimuthal electric current J_θ in the magnetic field and is given by [66]

$$F_t = \frac{1}{4} \delta_{el} \mu_0 \frac{\partial (J_\theta^2)}{\partial s} \tag{2.24}$$

In contrast to the Marangoni force the tangential electromagnetic force is therefore independent of the flow and thermal fields. The direction and point of attack is shown in figure 2.4.

Finally the *rotation* contributes with a centrifugal force field, which also acts as a driving force on the flow field. The centrifugal force field is obviously dependent on the rate of rotation, but also on the diameter of the crystal.

A dimensional analysis of the driving forces is given in appendix B, page 109 and a simulation of the individual influence of the four driving forces can furthermore be found in section 5.1, page 59. The analysis of the driving forces is a completion of an early part of this work [38].

The *boundary conditions* are no-slip at the counter-rotating phase boundaries and shear stress at the free surface given by (2.23-2.24).

The main assumption in the melt convection model is that the flow and the driving forces are rotational symmetric, however, studies of three-dimensional flows in the floating-zone configuration [66, 67], show that the three-dimensional effects are limited. The melt convection is furthermore decoupled from the heat transfer and free surface models by assuming negligible convective heat transfer and dynamic pressure.

2.5 Dopant transport

The transport of dopant in the molten silicon is a convection-diffusion problem, with a known velocity field. This decoupling from the momentum equations (2.19) is justified through the low concentrations of dopant and therefore a negligible solutal buoyancy[1]. The mathematical model is transport of a scalar, which in the axisymmetrical case for constant diffusivity is described by [56]

$$\underbrace{\frac{\partial C}{\partial t}}_{transient} \underbrace{- D\left[\frac{1}{r}\frac{\partial}{\partial r}\left(r\frac{\partial C}{\partial r}\right)+\frac{\partial^2 C}{\partial z^2}\right]}_{diffusion} + \underbrace{v_r\frac{\partial C}{\partial r}+v_z\frac{\partial C}{\partial z}}_{convection} = 0 \tag{2.25}$$

where C denotes concentration of dopant. From *experimental* experience it is noted that influence from the doping method, from feed rod or through the free surface, on the final

[1] Concentrations are well below ppm levels.

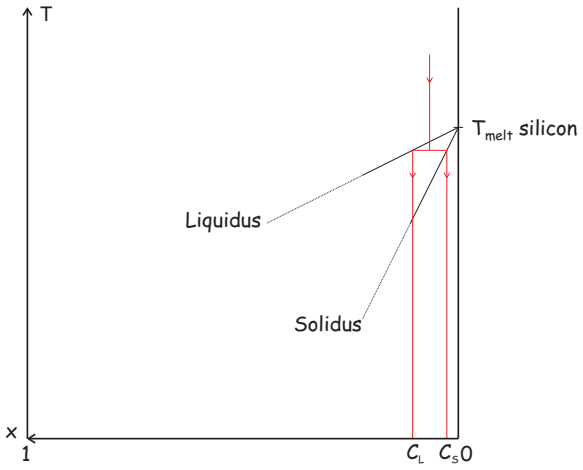

Figure 2.6. *Schematic equilibrium binary phase diagram for Si/P. x is the fraction of P.*

distribution of dopant in the crystal is small. A uniformly doped feed rod that melts at a constant rate can therefore modelled by a fixed concentration or by a prescribed flux through the upper phase boundary, whereas gas phase doping can be modelled by prescribing a flux to a part of the free surface. The boundary condition on rest of the free surface (or the entire free surface if doping is through the feed) is zero flux from the assumption of negligible evaporation or a prescribed flux simulating gas-doping [30].

The reason for studying dopant transport is as previously mentioned to simulate the incorporated dopant in the grown crystal, which primarily depends on the dynamics of the boundary layer near the lower phase boundary. Silicon and the most frequent dopants, phosphorus or boron form an eutectic binary system of limited solid solubility [3]. The phase diagram is fairly complicated, but since the concentration of dopant for this application is dilute, only the vicinity of zero dopant concentration is of interest, see figure 2.6. The physics of the incorporation of phosphorus is a binary composition of phosphorus and silicon that is cooled below the melting point of silicon, which is higher than the melting point of phosphorus. The limited solid solubility then results in a concentration of dopant in the solid silicon lower than that of the molten binary solution [30, 88]. The red line on figure 2.6 shows the process in the phase diagram. This phenomenon is called segregation and is characterized by the equilibrium segregation constant k_0

$$k_0 \equiv \frac{C_S}{C_L} \tag{2.26}$$

The rejection of dopant will dynamically result in a concentration boundary layer of higher concentration near the phase boundary, as will be seen in the simulations. The segregation is modelled with a Robin type boundary condition

$$D\frac{\partial C}{\partial n} = -V_{crystal}(1-k_0)C\cos\alpha \tag{2.27}$$

where the flux out of the molten zone depends on the local concentration C and the pull velocity $V_{crystal}$. The cosine is a projection of the interface upon the growth direction, see figure 2.4. Note that $V_{crystal} < 0$, due to the orientation of the coordinate system, yielding a positive gradient *out* of the molten zone, hence a diffusive flux *into* the molten zone. The direct modelling of the segregation by (2.27) includes the dynamics of the concentration boundary layer, so that the use of an effective segregation [9] can be avoided.

With a known concentration of dopant at the lower phase boundary $C_{Cr}(r)$, the normalized resistivity distribution in the crystal can be calculated as [57]

$$\rho(r) = \frac{1}{C_{Cr}(r)} \tag{2.28}$$

where $\rho(r)$ is the resistivity and $C_{Cr}(r)$ is the non-dimensional dopant concentration at the lower phase boundary.

The assumptions inherent in the dopant model are therefore rotational symmetry, zero evaporation from the free surface, an inward flux of dopant modelled by a constant concentration on the feed rod or a flux through the free surface. Segregation is modelled directly and diffusivity is assumed to be independent of temperature.

2.6 Transport of defects

The defect modelling done in this work limits itself to point defects of two types *self-interstitials* (A-defects) and *vacancies* (D-defects). Self-interstitials are excess silicon atoms present in the crystal, but not incorporated in the lattice and vacancies are atoms in the lattices that "are missing", see figure 2.7. These defects have the ability to cluster together to form for e.g. large voids, which influence the quality of the grown crystal.

The defects are assumed to be generated at the solidification process and incorporated in the crystal at the lower phase boundary at equilibrium concentrations [16, 17, 77]. The defect

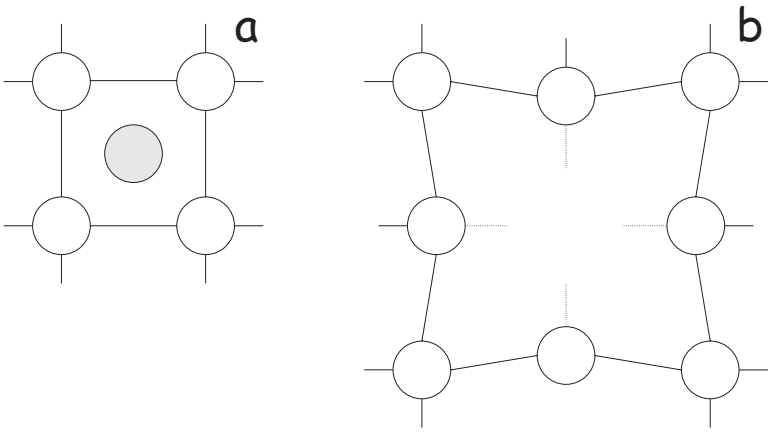

Figure 2.7. *(a) self-interstitial and (b) vacancy type point defects.*

distribution grown into the crystal after the growth process, when it has been cooled to room temperature, is influenced by two different modes of transport and the recombination of an interstitial and a vacancy defect to neutralize each other. The two transport modes are *Fickian diffusion* from gradients of concentration, and *convection* from the bulk motion of the crystal. Some works also include a term of thermodiffusion [8, 78], but according to [16] it is negligible compared to Fickian diffusion.

The transport equations for concentration of vacancies C_V and self-interstitials C_I are given by (2.29)

$$-\vec{\nabla}\cdot\left(D_V\vec{\nabla}C_V\right)+\vec{V}_{crystal}\cdot\vec{\nabla}C_V = -k_{IV}(C_VC_I-C_V^{eq}C_I^{eq}) \tag{2.29a}$$

$$-\vec{\nabla}\cdot\left(D_I\vec{\nabla}C_I\right)+\vec{V}_{crystal}\cdot\vec{\nabla}C_I = -k_{IV}(C_VC_I-C_V^{eq}C_I^{eq}) \tag{2.29b}$$

Concentrations are designated C and subscript V and I indicates vacancies and interstitials, respectively. Superscript eq denote equilibrium concentration, which is only a function of temperature, and k_{IV} is the recombination coefficient. Note that the pull speed $V_{crystal} < 0$ because of the orientation of the coordinate system, see figure 2.3. The diffusivities of vacancies and interstitials are denoted D_V and D_I, respectively. All parameters are strongly temperature dependent and specified in appendix A, page 106.

With the temperature field as input for the calculation, the temperature dependence can be transformed into a spatial dependence

$$D(T) = D(T(r,z)) \tag{2.30}$$

Hereby can the temperature dependence of the diffusivity be handled by expanding the diffusion term, here in (2.29a)

$$-\nabla\left(D_V \nabla C_V\right) = -D_V \frac{1}{r}\frac{\partial}{\partial r}\left(r\frac{\partial C_V}{\partial r}\right) - D_V \frac{\partial^2 C_V}{\partial z^2} - \left[\frac{\partial D_V}{\partial T}\frac{\partial T}{\partial r}\right]\frac{\partial C_V}{\partial r} - \left[\frac{\partial D_V}{\partial T}\frac{\partial T}{\partial z}\right]\frac{\partial C_V}{\partial z} \tag{2.31}$$

With the known temperature field, the terms in square brackets can be calculated a priori, and included as convective terms. The diffusivities D_V and D_I are likewise determined throughout the domain before solving the equations by using (2.30). Since there are no radial velocity component v_r the system of equations (2.29) expands to

$$-D_V\left[\frac{1}{r}\frac{\partial}{\partial r}\left(r\frac{\partial C_V}{\partial r}\right) + \frac{\partial^2 C_V}{\partial z^2}\right] + \left(-\frac{\partial D_V}{\partial T}\frac{\partial T}{\partial r}\right)\frac{\partial C_V}{\partial r} + \left(V_{crystal} - \frac{\partial D_V}{\partial T}\frac{\partial T}{\partial z}\right)\frac{\partial C_V}{\partial z} = -k_{IV}\left(C_V C_I - C_V^{eq} C_I^{eq}\right) \tag{2.32a}$$

$$-D_I\left[\frac{1}{r}\frac{\partial}{\partial r}\left(r\frac{\partial C_I}{\partial r}\right) + \frac{\partial^2 C_I}{\partial z^2}\right] + \left(-\frac{\partial D_I}{\partial T}\frac{\partial T}{\partial r}\right)\frac{\partial C_I}{\partial r} + \left(V_{crystal} - \frac{\partial D_I}{\partial T}\frac{\partial T}{\partial z}\right)\frac{\partial C_I}{\partial z} = -k_{IV}\left(C_V C_I - C_V^{eq} C_I^{eq}\right) \tag{2.32b}$$

The defect model is the convection-diffusion problem from the dopant transport expanded to two dependent variables and with a non-zero right hand side, that couples them.

Defects are incorporated in the crystal at the lower phase boundary in equilibrium concentrations, so here the boundary condition is

$$C_V = C_V^{eq}(T_m) \tag{2.33a}$$

$$C_I = C_I^{eq}(T_m) \tag{2.33b}$$

At the outer surface of the crystal [78] uses a no-flux condition

$$\frac{\partial C_V}{\partial n} = 0 \tag{2.34a}$$

$$\frac{\partial C_I}{\partial n} = 0 \tag{2.34b}$$

which will also be used in this work.

In summary the defect model only treats point defects, not clusters of defects or the complicated subspecies [22]. It is based on a continuum assumption applying convective and diffusive transport, with zero flux of defects through the surface of the crystal.

Chapter 3

Numerical implementation

This chapter describes how the mathematical models from the previous chapter are implemented. It elaborates on the numerical schemes in the finite element approximation and especially how the individual models are linked together to form the simulation. The level of detail in the description of the commercial parts of the models is limited, because the source code is not available and the manuals are focused on the application of the programmes. For the model for transport of dopant and defects, developed within this project, a more detailed description is provided. Figure 2.1, page 10, gives an overview of the models and how the are connected.

3.1 Electromagnetic and free surface model

The electromagnetic model is part of the commercial FZ-Sim software and is implemented as a *boundary element model*. The surfaces of inductor, free surface and melting front are therefore parted in surface elements, where each element interacts with all the other surface elements to form the system to be solved.

The free surface model, which is also part of FZ-Sim, uses a *Runge-Kutta* method that tracks the free surface from the lower triple point until it falls within the radius of the predefined upper triple point ($r < R_{upper\ tripple}$) using (2.12). The pressure difference P_0 is then adjusted and the procedure repeated until the free surface ends at the upper triple point, see figure 2.3.

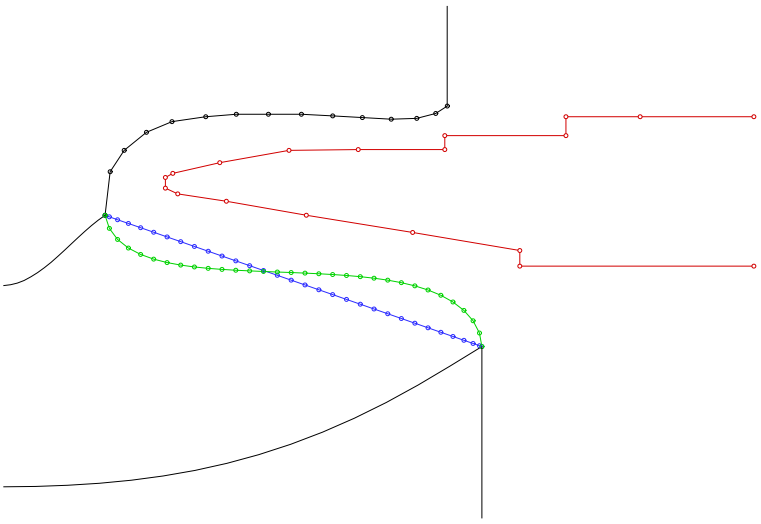

Figure 3.1. *Interaction between the electromagnetic and free surface models. The blue line is the initial guess on a free surface shape and the green is the converged solution. The boundary elements shown on the inductor, free surface and melting front are subdivided in the calculation to increase accuracy.*

These two models are connected because the shape of the free surface influences the normal electromagnetic force F_n and the current distribution J_θ and vice versa. After the electromagnetic force has been calculated, then the shape of the free surface can be determined. Thereafter, using the newly calculated free surface shape, the electromagnetic model is solved again, forming an iteration that is continued until the changes to the free surface falls below a predefined limit. The iteration converges fast (3-5 iterations) because the electromagnetic force is weak compared to the remaining terms in (2.11), thus resulting in a weak coupling. The interaction between the two models is shown in figure 3.1.

The free surface is assumed not to be affected by convection, but only by the electromagnetic field, the static pressure and the surface tension. The temperature dependence of the surface tension is furthermore too weak to have any influence on the shape of the free surface. This implies that the free surface shape can be uncoupled from the temperature field and therefore calculated a priori.

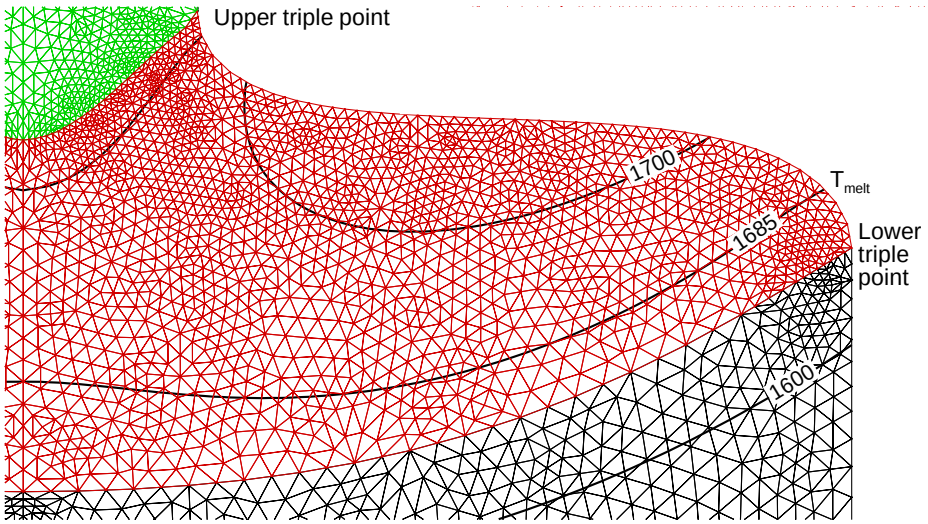

Figure 3.2. *During inner iteration loop. The red mesh is the molten zone, green is feed rod and black is the crystal. In this iteration some of the free surface is frozen, so for the next iteration more heat is added by increasing the gain factor. The iteration is continued until the melting point isotherm is at the lower triple point.*

3.2 Heat transfer with moving boundaries

In order to handle the alteration of the upper and lower phase boundaries, the heat transfer model employs *moving boundaries*. The approach is Lagrangian, in the sense that the mesh deforms corresponding to the physics, rather than Eulerian, where a fixed mesh is used and the boundary is made up of physical properties varying in space [76]. As described in section 3.1, the shape of the free surface is decoupled from the heat transfer calculation.

For a given joulean heat input and a given shape of the phase boundaries, the heat transfer can be solved without iteration. This solution, however, is *not* restricted to yield melting point temperature in the lower triple point. To achieve melting point temperature in the lower triple point, the joulean heat input is adjusted by multiplying the current distribution by a *gain factor*. An *inner loop* is thereby formed by starting out with some value of the gain factor, calculate the temperature field and then adjust the gain factor up if the melt is too cold or down if the melt is too hot. Figure 3.2 shows an early step in the iterations

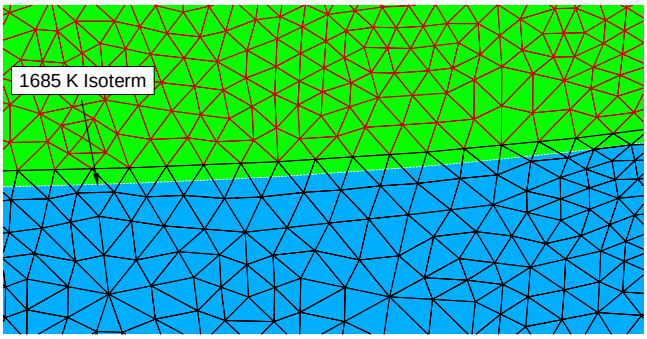

Figure 3.3. *The moving phase boundary at the melt/crystal interface. After convergence the mesh is regenerated, so that the phase shift, transition between the red and black mesh, is placed on the melt point isotherm (1685 K).*

where the melt is too cold, the gain factor is therefore increased and the calculation is done again[1].

The result of the inner loop is therefore a temperature field where the lower triple point is at melting point temperature. The inner loop can be done in 20-50 iterations depending on how damped the algorithm is. If the position of the upper triple point, which is placed by hand, matches the real physical situation then it will also be at melting point temperature, otherwise it will have to be moved and the coupled electromagnetic and free surface model will have to be employed again. Placing the upper triple point correctly is the more delicate part of the heat transfer modelling.

Assuming that the upper triple point is placed correctly and the inner loop determines a gain factor giving both triple points melting point temperature, then the calculation still has to determine the shape of the phase boundaries. This is done in an *outer loop*, where tracking of the phase boundaries is done through positioning them on the melting point isotherm after each inner loop, see figure 3.3. This procedure converges rapidly, ensuring the right position of the phase shift. Depending on the accuracy, wanted 20-30 iterations starting from flat phase boundaries, give a converged solution.

The more curved upper phase boundary is very sensitive to changes and therefore a relaxation of the phase boundary update is implemented. Initially FZ-Sim did not contain a movable upper phase boundary. It was, as the melt front, fixed to a prescribed shape and held at melt point temperature. However shape of the upper phase boundary is an

[1] This is in fact similar to the manner the operator dynamically control the heat input to the real process.

integral part of the solution, so to yield realistic results it *must* be allowed to move. An updated version of FZ-Sim therefore includes this feature. Furthermore, in contrast to the melt front, the shape of the upper phase boundary can not be photographed and is therefore more difficult to prescribe.

3.3 The melt convection model

The calculation of unsteady melt convection is done using MHAC from Cape Simulations Inc [11]. Only unsteady convection is considered, since both the investigated configurations exhibit time dependent behaviour. MHAC is a finite element code that utilizes an unstructured mesh of six-node triangles for these calculations. The formulation is in primitive variables $(\vec{V}, p)$ and the pressure correction of the Navier-Stokes is handled through a Lagrangian multiplier method [68]. MHAC offers the possibility of both, semi implicit time stepping, where time is explicit in the predictor and implicit in the corrector steps and fully implicit time stepping, where time is implicit in both [61]. Fully implicit time stepping being recommended by Cape Simulations Inc. is applied for the convection calculations.

The Marangoni and the tangential electromagnetic forces are implemented through stress boundary conditions. These are accessible through user subroutines, with the Marangoni already present and the electromagnetic force implemented within this project. Besides the stress conditions a zero normal velocity on the free surface is prescribed. The original flow solver, predecessor of MHAC, delivered by Cape Simulations Inc. did not include the constraint on zero normal velocity, leading to unphysical results with flow through the free surface.

The procedure for flow calculations with MHAC is to use the phase boundaries and joulean heat input, as calculated by FZ-Sim, and then assume melting point temperature on the now *fixed phase boundaries*. The initial guess for the energy equation is zero temperature, but due to the high heat conductivity and the joulean heat input, a quasi stationary temperature field is reached within 10-15 seconds. Likewise the initial guess for the velocity field is zero, but the startup procedure is more complicated. Buoyancy is the strongest of the driving forces, so strong that to remain within the radius of convergence, gravity has to be slowly ramped up from zero to normal gravity. This is done linearly over a period of 45 seconds,

which is slow enough to ensure convergence. The Marangoni, electromagnetic and rotational forces are all present from startup.

3.4 Finite element model of transport equation

This section contains a derivation of the finite element model for the axisymmetric transport equation in the dopant model of FEM-CD. FEM-CD takes the velocity field from MHAC as input for the calculations.

The velocity field from MHAC consists of finite element nodes and matching velocities, so for obvious reasons the mesh generated by MHAC is reused by FEM-CD. In creating FEM-CD, the programme was made general, in the sense that it is able to handle cartesian as well as cylindrical coordinates, and 6 node as well as 3 node elements. However, in the course of implementing and testing the code, it became apparent that the conversion from 6 node elements to 3 node elements, shown on figure 3.4, was as successful as using the second order 6 node triangles. Therefore linear triangles are applied in the simulations.

The mathematical model of the dopant transport is described by (3.1) and consists of transient, diffusive and convective terms

$$\underbrace{\frac{\partial C}{\partial t}}_{transient} \underbrace{-D\frac{1}{r}\frac{\partial}{\partial r}\left(r\frac{\partial C}{\partial r}\right) - D\frac{\partial^2 C}{\partial z^2}}_{diffusion} + \underbrace{v_r\frac{\partial C}{\partial r} + v_z\frac{\partial C}{\partial z}}_{convection} = q(r,z) \tag{3.1}$$

where v_r is the r-component and v_z is the z-component of the velocity field. The right hand side of (3.1) contain a source term $q(r,z)$. A finite element model discretizes a continuous equation into a matrix equation, where each degree of freedom corresponds to a node in the mesh, hence (3.1) is transformed into (3.2)

$$(\mathbf{A}^{trans} + \mathbf{A}^{dif} + \mathbf{A}^{conv})\,\vec{\hat{C}} = \vec{B} \tag{3.2}$$

Here $\mathbf{A}^{trans}$, $\mathbf{A}^{dif}$ and $\mathbf{A}^{conv}$ are the transient, diffusive and convective parts of the coefficient matrix, $\vec{B}$ is the right hand side and $\vec{\hat{C}}$ is the nodal values of the solution. The resulting linear system (3.2) will be sparse for the general unstructured mesh applied, with about 99.8% zeros. It is therefore in terms of computational efficiency recommendable to

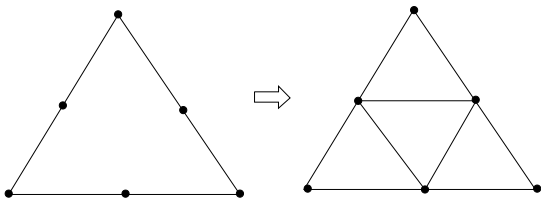

Figure 3.4. *Conversion of 6 node elements to 3 node elements.*

apply a sparse solver and sparse storage. The sparse solver used in FEM-CD is MA41 by AEA Technology [2]. Efficient ways to store sparse vectors and matrices can be found in [18].

The computation of the three matrices in (3.2) will be derived separately in sections 3.4.1-3.4.3 and the implementation of the boundary conditions is dealt with in section 3.4.4.

3.4.1 Diffusion

The approach for the diffusion is the standard *Galerkin* [6, 29, 68]. Using the following notation

$$C_r = \frac{\partial C}{\partial r}, \qquad C_z = \frac{\partial C}{\partial z}$$

the weak form of (3.1) is given by (3.3) where ψ is a shape or base function on the computational domain Ω, $\psi \in C^1(\Omega)$. Furthermore $\psi = 0$ on $\partial\Omega$.

$$D \int_V \left[\frac{1}{r} \left(rC_r \right)_r + C_{zz} \right] \psi dV = - \int_V q\psi \; dV \tag{3.3}$$

$$D \int_0^R \int_0^{2\pi} \int_0^L \left[\frac{1}{r} \left(rC_r \right)_r \psi + \frac{1}{r} (rC_z)_z \psi \right] r dr d\theta dz = - \int_0^R \int_0^{2\pi} \int_0^L q\psi \; r dr d\theta dz$$

$$2\pi D \int_0^R \int_0^L \left[\left(rC_r \right)_r \psi + (rC_z)_z \psi \right] dr dz = -2\pi \int_0^R \int_0^L q\psi \; r dr dz$$

$$D \int_\Omega \int \left[\left(rC_r \right)_r \psi + (rC_z)_z \psi \right] dr dz = - \int_\Omega \int q\psi \; r dr dz \tag{3.4}$$

Integration by parts

$$\int_\Omega \int \left(rC_r \right)_r \psi dr dz = \int_{\partial\Omega} rC_r \psi ds - \int_\Omega \int rC_r \psi_r dr dz \tag{3.5}$$

$$\int_\Omega \int \left(rC_z \right)_z \psi dr dz = \int_{\partial\Omega} rC_z \psi ds - \int_\Omega \int rC_z \psi_z dr dz \tag{3.6}$$

The surface integrals over $\partial\Omega$ are seen to be zero since $\psi = 0$ on $\partial\Omega$. Inserting (3.5) and (3.6) into (3.4) gives

$$D \int_\Omega \int \left[C_r \psi_r + C_z \psi_z \right] r dr dz = \int_\Omega \int q\psi \; r dr dz \tag{3.7}$$

Let M denote the total number of nodes, then C can be approximated by $\hat{C}$ where

$$\hat{C}(r,z) = \sum_{j=1}^{M} \hat{C}_j \; N_j(r,z), \qquad \psi = N_j(r,z) \tag{3.8}$$

$\hat{C}$ given by (3.8) is inserted into (3.7)

$$D \int_\Omega \int \left[\sum_{j=1}^{M} \hat{C}_j \; (N_j)_r (N_i)_r + \sum_{j=1}^{M} \hat{C}_j \; (N_j)_z (N_i)_z \right] r dr dz = \int_\Omega \int q N_i \; r dr dz \tag{3.9}$$

(3.9) corresponds to a system of linear equations

$$\sum_{j=1}^{M} a_{ij}^{dif} \hat{C}_j = b_i$$

The components of $\mathbf{A}^{dif}$ and $\vec{B}$ is therefore given by (3.10) and (3.11)

$$a_{ij}^{dif} = D \int_\Omega \int \left[(N_j)_r (N_i)_r + (N_j)_z (N_i)_z \right] r dr dz \tag{3.10}$$

$$b_i = \int_\Omega \int q N_i \; r dr dz \tag{3.11}$$

The diffusive matrix A^{dif} and the right hand side $\vec{B}$ are then generated elementwise, by calculating the entries using (3.10) and (3.11).

3.4.2 Convection

This section contains the analysis for the standard Galerkin and the monotone streamline upwind approach to the convection. The Galerkin method is similar to the central-difference approximation from the finite difference method and produces non-physical wiggles for convection-dominated problems. In trying to manage the convection-dominated nature of the problem, a streamline diffusion model was also tried [21, 29]. This model, however, did not perform satisfactory at the high solutal Peclét numbers realized in FZ modelling ($Pe_C \approx 1.5 \cdot 10^4$). The preference of an *upwind scheme* at high Peclét numbers

was suggested by [70]. Other approaches to avoid oscillatory and unphysical solutions to convection-dominated problems include, upwinding through modifying the weight functions, to incorporate some Peclét number dependence or asymmetry [24, 26, 60, 63, 74]. An approach where the base and weight functions differ is denoted Petrov-Galerkin[1].

Galerkin approach to convection

The analysis for the convection in a Galerkin approach is quite similar to the diffusion. The weak form of the convective terms of (3.1) is

$$\int_V [v_r C_r + v_z C_z]\, \psi dV = 0 \tag{3.12}$$

$$\int_0^R \int_0^{2\pi} \int_0^L [v_r C_r \psi + v_z C_z \psi]\, r dr d\theta dz = 0$$

$$\int_0^R \int_0^L [v_r C_r \psi + v_z C_z \psi]\, r dr dz = 0$$

using same notation as in the previous section. By using partial integration similar to (3.5) and (3.6) one obtains

$$\int_\Omega \int [v_r C \psi_r + v_z C \psi_z]\, r dr dz = 0 \tag{3.13}$$

which results in the following equation for a_{ij}^{conv}

$$a_{ij}^{conv} = \int_\Omega \int [v_r (N_j)_r (N_i) + v_z (N_j)_z (N_i)]\, r dr dz \tag{3.14}$$

Base functions are usually polynomials, so, for a mesh consisting of 3 node triangular elements, $N(r, z) = ar + bz + c$ would be standard, hence these are also called linear elements. The derivative of a linear function is a constant, so for the diffusion the integral in (3.10) is a constant times r, where the convection gives a slightly more complex integral. For the 6 node triangular elements, where the base functions are second order, the integral will be yet more elaborate, but still a polynomial.

[1] The streamline diffusion model is also Petrov-Galerkin, since the inclusion of the extra diffusion in the streamwise direction is done through modifying the weight functions.

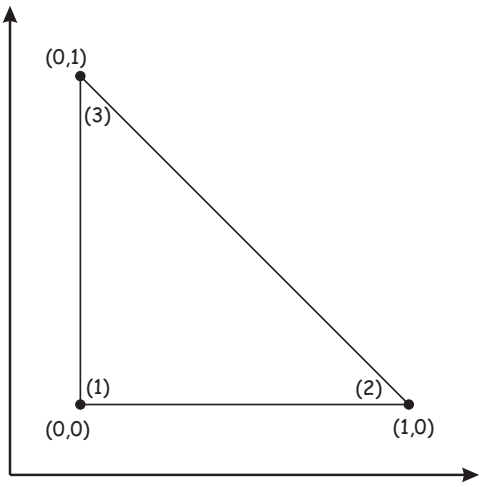

Figure 3.5. *Three node finite element, the standard element* $\tilde{e}$.

To deal with the integrals in (3.14), FEM-CD includes a coordinate transformation, in which a general element is mapped onto a standard element as in [5], see figure 3.5. The integral can then be transformed from the general element e_n to the standard element $\tilde{e}$ using (3.15)

$$\int_{e_n} f(r,z) r dr dz = |J_{rz}| \int_{\tilde{e}} f(r(\tilde{r},\tilde{z}), z(\tilde{r},\tilde{z}))\, r(\tilde{r},\tilde{z}) d\tilde{r} d\tilde{z} \tag{3.15}$$

where J_{rz} is the jacobian [62]. In assembling the coefficient matrix (3.14) all integrants are polynomial, so the integrals are calculated analytically to reduce the computational load. For the right hand side (3.11) the source term q is an arbitrary continuous function, which necessitates numerical integration, for this a second order Simpson formula is implemented [62].

Monotone streamline upwind approach to convection

The upwind scheme applied to handle convection-dominated situations is the monotone streamline upwind scheme, taken from [70]. The scheme has been adapted to an axisymmetric geometry with triangular elements and only implemented for 3 node triangles.

In order to explain the method, one can think of the case without diffusion (infinite solutal Peclét number), here the governing equation (3.1) without source terms reduces to

$$v_r \frac{\partial C}{\partial r} + v_z \frac{\partial C}{\partial z} = u_s \frac{\partial C}{\partial s} = 0 \tag{3.16}$$

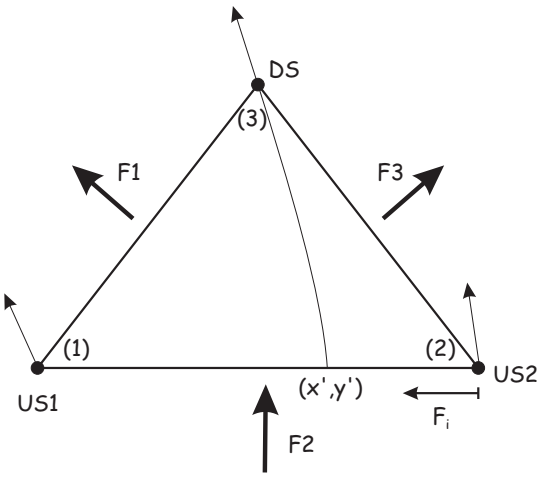

Figure 3.6. *Streamline upwinding definitions. DS is the downstream node, US1 and US2 are upstream nodes and* (x', y') *are the coordinates of the upstream point.* $F1$ *-* $F3$ *are fluxes used to determine the position of* (x', y')*.*

where s is the coordinate along the streamline and u_s is the velocity along s. Within an element it is assumed that

$$u_s \frac{\partial C}{\partial s} = \text{constant} \tag{3.17}$$

In this manner the weak form (3.12) can be written as

$$\int_V \left[v_r C_r + v_z C_z\right] \psi dV = \underbrace{u_s \frac{\partial C}{\partial s}}_{upwind} \int_V \psi \; dV \tag{3.18}$$

where the term outside the integration can be approximated by a simple upwind difference. To evaluate the upwind difference, a streamline going through the element needs to be identified. The definitions of the geometry required are given in figure 3.6. The position of the upstream point (x', y') determines the weighting F_i between the two upstream nodes and therefore it needs to be found. This can, at a very low computational effort, be done for linear elements using the fluxes through the three faces of the element. Since the density

is constant, the fluxes are merely curve integrals along the faces, as given in (3.19).

$$F_1 = \int_{DS}^{US1} -v_z \; r \; dr + \int_{DS}^{US1} v_r \; dz \tag{3.19a}$$

$$F_2 = -\left\{ \int_{US1}^{US2} -v_z \; r \; dr + \int_{US1}^{US2} v_r \; dz \right\} \tag{3.19b}$$

$$F_3 = -\left\{ \int_{DS}^{US2} -v_z \; r \; dr + \int_{DS}^{US2} v_r \; dz \right\} \tag{3.19c}$$

The weighting represented by F_i, see figure 3.6, is thereafter calculated by (3.20).

$$\frac{F_3}{F_2} = F_i \quad , \qquad \frac{F_1}{F_2} = 1 - F_i \tag{3.20}$$

The position (x', y') found by (3.21) is used to calculated the upwind term in (3.18).

$$x' = F_i \cdot x_{US1} + (1 - F_i) \cdot x_{US2} \tag{3.21a}$$

$$y' = F_i \cdot y_{US1} + (1 - F_i) \cdot y_{US2} \tag{3.21b}$$

With the distance ds between the downstream DS node and the upstream point (x', y'), the three contributions to the coefficient matrix are given by

$$\begin{bmatrix} 0 & 0 & 0 \\ 0 & 0 & 0 \\ (1 - F_i)\frac{u_s}{ds} \int N_{DS} \; dA & F_i \frac{u_s}{ds} \int N_{DS} \; dA & \frac{u_s}{ds} \int N_{DS} \; dA \end{bmatrix} \tag{3.22}$$

Here the local numbering of the nodes is $US1$: 1, $US2$: 2 and DS: 3, see figure 3.6. It is important to notice, that the weight function being integrated is the local basis function of the downstream node *for all* contributions. The value for u_s is also taken from the downstream node.

The downstream node receives contributions from all the elements that it is a part of, where the integration in the given element involves the local basis function that corresponds to the downstream node. Every contribution to DS is followed by additions to the two upstream nodes, even though they are not part of the the element, where the downstream node is present.

3.4.3 Transient term

The transient term $\mathbf{A}^{trans}$ of (3.2) is handled in a backward difference scheme similar to the upwind scheme for the convection. It is elementwise assumed that

$$\frac{\partial C}{\partial t} = C_t = \text{constant} \tag{3.23}$$

So as in (3.18) the time derivative of the concentration can be placed outside the integration.

$$\int_V C_t \psi dV = \frac{\partial C}{\partial t} \int_V \psi \; dV \tag{3.24}$$

The finite difference approximation of $\partial C/\partial t$ is implemented in two versions using information from previous time steps [61].

$$\frac{\partial C}{\partial t} = \frac{C^n - C^{n-1}}{\Delta t} \tag{3.25}$$

$$\frac{\partial C}{\partial t} = \frac{3C^n - 4C^{n-1} + C^{n-2}}{2\Delta t} \tag{3.26}$$

n denotes the current time step and Δt the size of the time steps. It is therefore evident, that the transient term besides a contribution to the coefficient matrix, also has a contribution to the right hand side. For the finite difference approximation in (3.25) the componentwise contributions to $\mathbf{A}^{trans}$ and $\vec{B}$ are

$$a_{ii}^{trans} = \frac{1}{\Delta t} \int_V \psi \; dV \tag{3.27}$$

$$b_i = \frac{C^{n-1}}{\Delta t} \int_V \psi \; dV \tag{3.28}$$

3.4.4 Boundary conditions

FEM-CD is able to handle three basic types of boundary conditions.

$$\begin{array}{lrcl} \textit{Dirichlet:} & C & = & f(r,z) \\ \textit{Neumann:} & \partial C/\partial n & = & -q(r,z) \\ \textit{Robin:} & \partial C/\partial n & = & -h(r,z)(C - C_0) \end{array}$$

These are all added to the linear system after the coefficient matrix $\mathbf{A}$ and the right hand side $\vec{B}$ are completed.

The Dirichlet boundary condition

In a general system of 4 linear equations, the equations without boundary conditions would be

$$\begin{bmatrix} a_{1,1} & a_{1,2} & a_{1,3} & a_{1,4} \\ a_{2,1} & a_{2,2} & a_{2,3} & a_{2,4} \\ a_{3,1} & a_{3,2} & a_{3,3} & a_{3,4} \\ a_{4,1} & a_{4,2} & a_{4,3} & a_{4,4} \end{bmatrix} \begin{bmatrix} \hat{c}_1 \\ \hat{c}_2 \\ \hat{c}_3 \\ \hat{c}_4 \end{bmatrix} = \begin{bmatrix} b_1 \\ b_2 \\ b_3 \\ b_4 \end{bmatrix} \tag{3.29}$$

If node 3 was a boundary point with a Dirichlet boundary condition forcing $\hat{c}_3 = f_3$ then it corresponds to

$$\begin{bmatrix} a_{1,1} & a_{1,2} & 0 & a_{1,4} \\ a_{2,1} & a_{2,2} & 0 & a_{2,4} \\ 0 & 0 & 1 & 0 \\ a_{4,1} & a_{4,2} & 0 & a_{4,4} \end{bmatrix} \begin{bmatrix} \hat{c}_1 \\ \hat{c}_2 \\ \hat{c}_3 \\ \hat{c}_4 \end{bmatrix} = \begin{bmatrix} b_1 - a_{1,3} f_3 \\ b_2 - a_{2,3} f_3 \\ f_3 \\ b_4 - a_{4,3} f_3 \end{bmatrix} \tag{3.30}$$

This is the general procedure used to add Dirichlet boundary conditions to the system.

The Neumann boundary condition

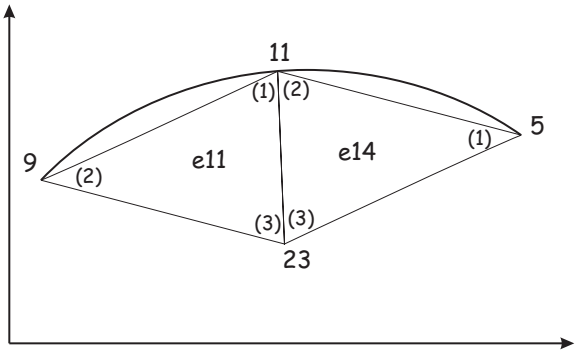

Figure 3.7. *Two elements on a boundary where a Neumann boundary condition is present.*

A Neumann boundary condition corresponds to a specified flux through a boundary, and therefore it has to be implemented through the right hand side b_i, so (3.11) becomes

$$b_i = \int_\Omega \int q N_i \; r dr dz + \underbrace{\int_{\partial\Omega} \tilde{q} N_i \; r dr dz}_{Neumann} \tag{3.31}$$

where $\tilde{q}$ is the flux out of the domain at node i. The Neumann contribution for node 11 in figure 3.7 is calculated as

$$\int_{\partial\Omega} \tilde{q} N_{11}\ r dr dz = \int_{(r5,z5)}^{(r9,z9)} \tilde{q} N_{11}\ ds \tag{3.32}$$

The integration of the local base function for node 11 is in element $e11$ and $e14$, respectively. With the integration in (3.32) the flux $\tilde{q}$ can be any continuous function of space.

For a given problem, the application of only Neumann conditions *does not* provide for a unique solution, they have to be combined with one of the other types, Dirichlet or Robin.

The Robin boundary condition

Applying Robin boundary conditions implies updating not only the right hand side $\vec{B}$, but also the coefficient matrix $\mathbf{A}$.

$$a_{ij} = a_{ij}^{dif} + a_{ij}^{conv} + a_{ij}^{trans} + \underbrace{\int_{\partial\Omega} h(r,z) N_i N_j r dr dz}_{Robin} \tag{3.33}$$

$$b_i = \int_\Omega \int q N_i\ r dr dz + \underbrace{\int_{\partial\Omega} h(r,z) C_0 N_i\ r dr dz}_{Robin} \tag{3.34}$$

The implementation of the integration along $\partial\Omega$ is similar to that of the Neumann boundary condition.

If a model requires the application of a Robin along with a Dirichlet boundary condition, then it is necessary that the Dirichlet condition is applied last, since Robin conditions merely *adds* a contribution to $\mathbf{A}$, whereas the Dirichlet condition *prescribes* certain values to entries in $\mathbf{A}$.

3.4.5 Mesh refinement

In order to resolve the concentration boundary layer, a refinement on the mesh from the convection calculations (MHAC) is applied. The procedure of adding extra elements is shown on figure 3.8. The need for the mesh refinement arises from the fact that a stable solution (quasi stationary) is based on the gradient from the segregation (2.27) being

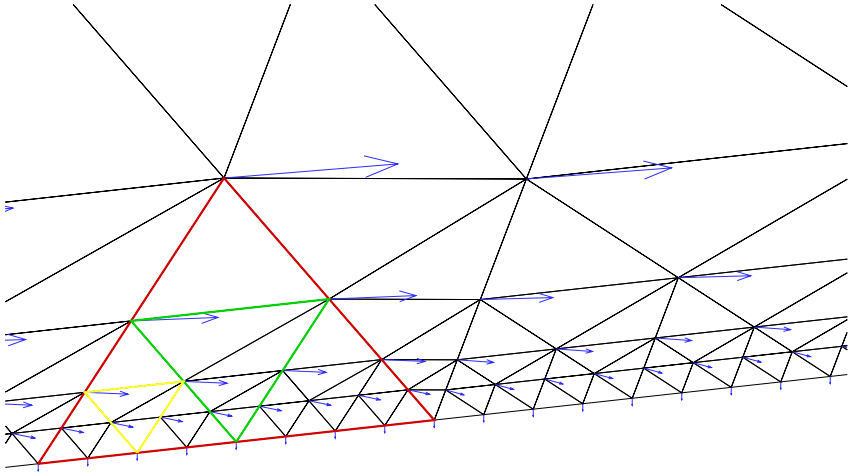

Figure 3.8. *The applied mesh refinement in the concentration boundary layer at the lower phase boundary. The red element is parted into four elements by adding the green element. The yellow element is thereafter added and so forth. Minimum element size is about 0.03 mm.*

balanced by the convective transport through the boundary layer into the crystal. If the convective transport in the elements in the concentration boundary layer is not uniform in the direction into the crystal, then the model fails to converge. The mesh generator in MHAC unfortunately does not provide the ability to increase the mesh density in the normal direction, hence the need for the extra refinement within FEM-CD.

3.5 Transport of defects

FEM-CD is also used to simulate the transport of point defects, but in a modified version. The defect types are shown on figure 2.7, page 22. This model differs from convection diffusion model of dopant transport in the sense that it is stationary, the diffusivities are spatial functions (2.30) and that two coupled equations (3.35) needs to be solved.

$$-D_V\left[\frac{1}{r}\frac{\partial}{\partial r}\left(r\frac{\partial C_V}{\partial r}\right)+\frac{\partial^2 C_V}{\partial z^2}\right]+\left(-\frac{\partial D_V}{\partial T}\frac{\partial T}{\partial r}\right)\frac{\partial C_V}{\partial r}+\left(V_{crystal}-\frac{\partial D_V}{\partial T}\frac{\partial T}{\partial z}\right)\frac{\partial C_V}{\partial z}$$

$$=-k_{IV}(C_V C_I - C_V^{eq} C_I^{eq}) \qquad (3.35a)$$

$$-D_I\left[\frac{1}{r}\frac{\partial}{\partial r}\left(r\frac{\partial C_I}{\partial r}\right)+\frac{\partial^2 C_I}{\partial z^2}\right]+\left(-\frac{\partial D_I}{\partial T}\frac{\partial T}{\partial r}\right)\frac{\partial C_I}{\partial r}+\left(V_{crystal}-\frac{\partial D_I}{\partial T}\frac{\partial T}{\partial z}\right)\frac{\partial C_I}{\partial z}$$

$$=-k_{IV}(C_V C_I - C_V^{eq} C_I^{eq}) \qquad (3.35b)$$

The coupling of (3.35a) and (3.35b) comes from the recombination, being the process where a self-interstitial moves into a vacancy and the two thereby neutralize each other. The recombination is handled by the right hand side which is identical for both equations.

The coefficient matrices for the two equations consist of a diffusive and a convective term as in (3.2), these are invariant to the iterations and need only be generated once. Thereafter the equations are solved sequentially as in (3.36).

$$(\mathbf{A}_V^{dif} + \mathbf{A}_V^{conv})\,\vec{\hat{C}}_V^{\,n+1} = \vec{B}(\vec{\hat{C}}_V^{\,n}, \vec{\hat{C}}_I^{\,n}) \qquad (3.36a)$$

$$(\mathbf{A}_I^{dif} + \mathbf{A}_I^{conv})\,\vec{\hat{C}}_I^{\,n+1} = \vec{B}(\vec{\hat{C}}_V^{\,n+1}, \vec{\hat{C}}_I^{\,n}) \qquad (3.36b)$$

$$n = 0, 1, 2, \ldots$$

To improve convergence a relaxation of the solution update (3.37) is used.

$$\vec{\hat{C}}^{\,n+1} = \alpha\vec{\hat{C}}^{\,n+1} + (1-\alpha)\vec{\hat{C}}^{\,n} \qquad (3.37)$$

where the relaxation factor $\alpha \in [0;1]$. The boundary conditions are added for each equation after a new right hand side has been determined. The implementation of the boundary conditions is as described in section 3.4.4.

Chapter 4

Conduction solution

This chapter describes the solution of the heat transfer as well as the electromagnetic and free surface models. The current distribution and free surface shapes are dealt with in section 4.1 and the temperature fields and phase boundary shapes in section 4.2. The lateral photovoltage scanning (LPS) technique [72] has been used at the Institute of Crystal Growth (IKZ), to measure the shape of the lower phase boundary for two different 4" configurations, in order to provide indirect experimental verification of the calculations. Section 4.3 contains simulations of the effect of convective cooling from flow in the pressurized surrounding gas in the chamber.

The calculations in this chapter consists of three fundamentally different configurations, two with 4" crystal diameter and one with a 0.8" crystal diameter. The three configurations and their growth conditions are listed below.

IKZ 4": Using the IKZ 4" configuration, *one crystal* has been grown at *three different rates of rotation*. A piece of crystal has been grown for each rotation to ensure adaption to the change of the growth conditions, hence the significant difference, for the conduction solution, is the length of the crystal and feed, which influences the heat transfer as shall be shown.

Topsil 4" The experiment using the Topsil 4" configuration was performed at constant rotation, but with *varying pressurization of the surrounding gas* to study the effect of convective cooling from the ambient gas. Again, the adaption to the change of growth

		IKZ 4"			Topsil 4"		IKZ 0.8"
		5 rpm	10 rpm	15 rpm	1.9 bar	3.3 bar	
Radius of crystal	[cm]	5.1	5.1	5.1	5.3	5.3	1.0
Radius of feed	[cm]	4.7	4.7	4.7	4.7	4.7	1.1
Radius at neck	[cm]	1.1	1.1	1.1	0.7	0.7	0.7
Length of crystal	[cm]	20.2	30.1	37.1	50.0	60.0	20.5
Length of feed	[cm]	38.7	26.7	18.4	32.7	20.0	15.0
Pull speed	[mm/s]	3.4	3.4	3.4	3.2	3.2	3.4
Rotation crystal	[rpm]	5.0	10.0	15.0	6.0	6.0	
Rotation feed	[rpm]	−15.0	−15.0	−15.0	−0.6	−0.6	
Frequency in coil	[MHz]	2.8	2.8	2.8	2.5	2.5	2.8

Table 4.1. *Configurations used for the simulations. The crystal from the IKZ 4" configuration is grown with three different rates of rotation and the crystal from the Topsil 4" configuration is grown at two different pressures, hence the designations.*

conditions causes different crystal and feed lengths for the two different pressures. The Topsil 4" configuration is dealt with in section 4.3.

IKZ 0.8" *The IKZ 0.8" configuration has been used to grow a crystal for the study of the formation of point defects using the DLTS technique. It will be used in chapter 6, with the temperature field calculated here as input.*

The IKZ 4" and the IKZ 0.8" crystals were not grown as part of this work, but the experimental results and geometrical input have been provided with the courtesy of IKZ. Table 4.1 gives an overview of the configurations and growth conditions.

4.1 Electromagnetics and free surface

The solution of the electromagnetic model is the azimuthal current distribution J_θ on the free surface, which depends on the shape of the free surface. The azimuthal current in the magnetic field causes a normal force on the free surface, affecting its shape and thereby linking the the two models, see figure 2.2 page 11. The simulation procedure is described in section 3.1, page 25.

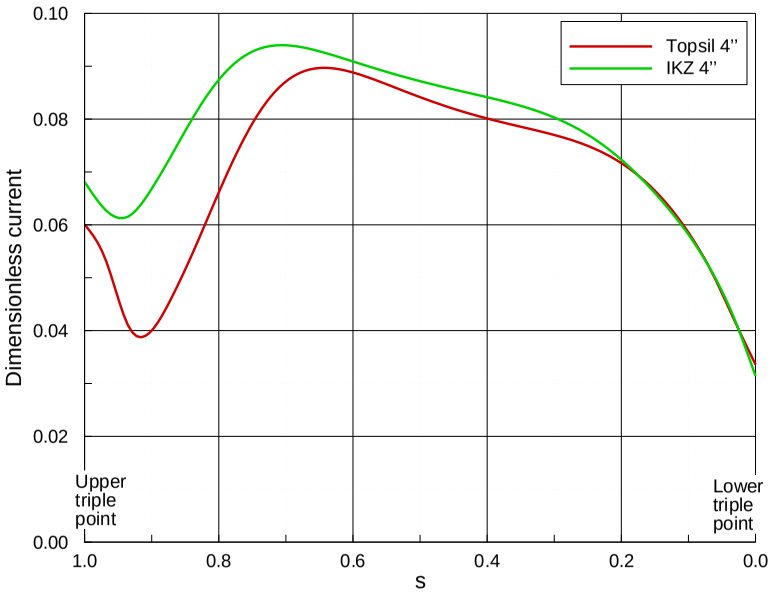

Figure 4.1. *Distribution of dimensionless electric current* $\tilde{J}_\theta = J_\theta/(2\pi I_0/R_{crystal})$ *on the free surfaces of the two 4" configurations. Definition of independent variable s can be found in figure 2.3, page 14.*

The dimensionless current distributions for the IKZ 4" and Topsil 4" configurations are shown in figure 4.1. Keeping in mind, that the current distribution is independent of crystal length and the surrounding pressure, there is only *one* current distribution for each configuration. The general course of the two current distributions is similar, but with distinctions due to geometrical differences of the inductors.

The tangential electromagnetic force (2.24) depends on the derivative of the squared current, so figure 4.1 indicates a positive force until $s \approx 0.7$ and then a negative force until about $s \approx 0.9$, where it then turns positive again. This means that the isolated electromagnetic convection will drive two counter rotating vortices, meeting in a stagnation point at about $s \approx 0.7$, perhaps with a small third vortex at the upper stagnation point. The isolated driving forces are simulated in section 5.1.

The shapes of the free surfaces for the two 4" processes, shown in figure 4.2, are primarily dictated by the surface tension and the hydrostatic pressure, whereas the differences in the electric current, from figure 4.1, has only little influence on the shape. This limited influence on the shape of the free surface from the electric current, can not be deduced

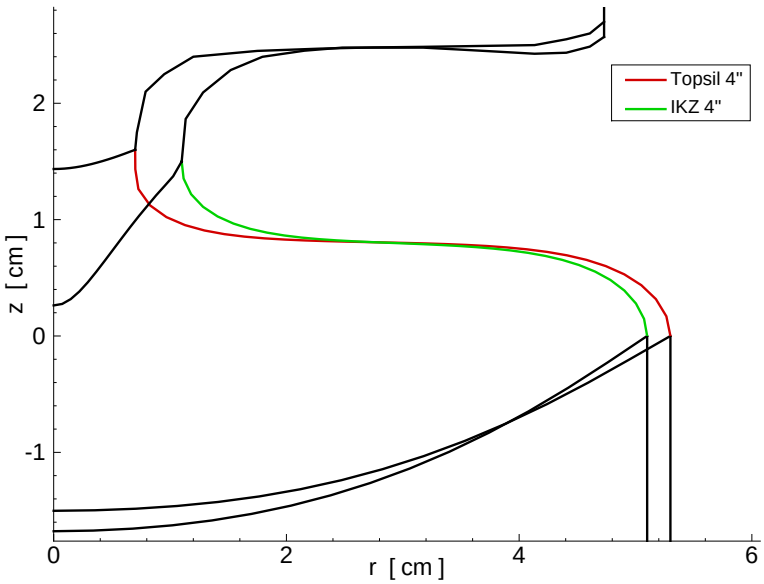

Figure 4.2. *Shape of the free surfaces for the IKZ 4" and Topsil 4" configurations.*

from figure 4.2, but is known from numerical experiments with different inductors and the dimensional analysis in appendix B.

The two 4" crystals are grown with the needle-eye technique, where the inner diameter of the inductor is much smaller than the diameter of the feed. The needle-eye technique was invented to facilitate a thin neck even when growing large crystals, in order to keep the floating zone molten all the way through, avoiding solidification of the core. The diameter of the feed for the IKZ 0.8" configuration, however, is small enough to avoid a solid core, without the pronounced needle-eye shape. The shape of the free surface for the IKZ 0.8" configuration is shown in figure 4.3.

The difference in the 0.8" and 4" free surfaces therefore clearly shows the principle of the needle-eye technique, in the sense that the increased crystal diameters do not make the floating zone much higher, but mainly wider. In principle the needle-eye technique does not contain any restrictions on the diameter of the crystals that can be grown, with respect to the free surface. In the extreme case of very large diameters, the free surface will have a completely horizontal part and curving ends.

It is to be kept in mind that the two triple points are *prescribed input* for the free surface modelling and that the calculated free surface shape and the current distribution is not final

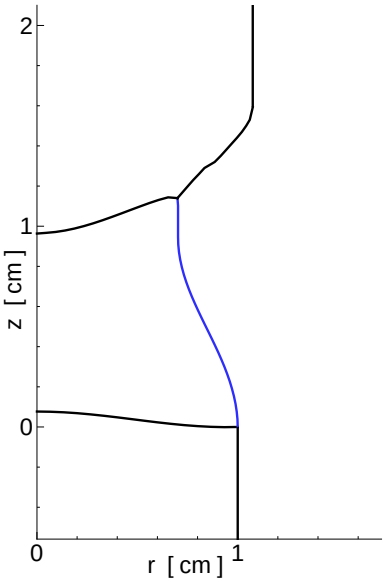

Figure 4.3. *Free surface (blue) of the IKZ 0.8" configuration.*

until it leads to melting point temperature at the upper triple point in the heat transfer calculation. If this is not the case, then it has to be moved using a "qualified guess", until the right position is found. This makes up the feed back loop between the free surface / electromagnetic models and the heat transfer in figure 2.1, page 10.

4.2 Heat transfer

After determining the joulean heat input and the shape of the free surface, the heat transfer is considered in this section. The heat transfer calculations are all stationary, since the geometrical changes from the advancing growth are slow compared to the time it takes to reach equilibrium. As previously mentioned, the Topsil 4" crystal has been grown to study convective cooling of the crystal, and the heat transfer of this configuration will be treated separately in section 4.3. This section therefore contains heat transfer calculations of the IKZ 4" and the IKZ 0.8" configurations, as well as LPS measurements of the lower phase boundary of the IKZ 4" configuration.

The temperature field of the IKZ 4" configuration in the three different stages of growth is shown in figure 4.4. Since the crystal is grown at a finite pull velocity there is a Peclét

number of $Pe \approx 0.2$, relating the convective and diffusive heat transfer. The convective heat transfer from the bulk motion of the crystal and feed is seen in figure 4.4, e.g. for the 10 rpm configuration, where the 1000 K isotherm is about 6 cm away from the melt front in the feed and about 10 cm from the lower triple point in the crystal. For a zero Peclét number the distances would be the same. Heat transfer calculations on this experiment has earlier been published in [58].

A closer look at the temperature field in the molten zone is given in figure 4.5. The point of maximum temperature is seen to be identical to where the current has its maximum value, $s \approx 0.7$. The depth of the upper phase boundary is 10.7 mm, at this pull speed of $V_{crystal} = 3.4$ mm/min. If the pull speed is increased to about 4 mm/min, the depth of the upper phase boundary will extend all the way to the lower one giving a solid core of the molten zone[1]. The reason that both phase boundaries deflect further by increasing pull speeds, is primarily the latent heat release and absorbtion being dependent on the mass flux (2.16), but also because of the increasing Peclét number.

Another observation that can be made from figure 4.5, is a very fast cooling of the crystal at the high temperatures, just below the lower triple point. The surface temperature falls 315 K in the first 3 cm from the triple point. This very rapid cooling at high temperatures can be attributed to the fourth order temperature dependence of the radiative heat loss (2.14). Rapid cooling gives rise to large temperature gradients in the crystal at the phase boundary, as shown on figure 4.6. Very large temperature gradients may cause the crystal to crack, but that is usually not a problem, unless the process is contaminated, thereby lowering the critical threshold.

Temperature gradients, however, do have significant influence on the incorporation of point defects in the crystal, as will be discussed in section 4.3 and chapter 6. The left part of figure 4.6 shows the magnitude of the temperature gradient vector $|\vec{\nabla}T|$, which reaches levels of about 150 K/cm near the phase boundary. In the Voronkov theory of defects [86], which will be introduced in chapter 6, only the axial component of the temperature gradient is considered. The axial gradient is therefore shown in the right part of figure 4.6, it reaches a maximum value of about 140 K/cm.

[1] This calculated maximum possible pull speed corresponds to the experience from growing the crystals, so the simulation "breaks down" at the same pull speed at the real process does.

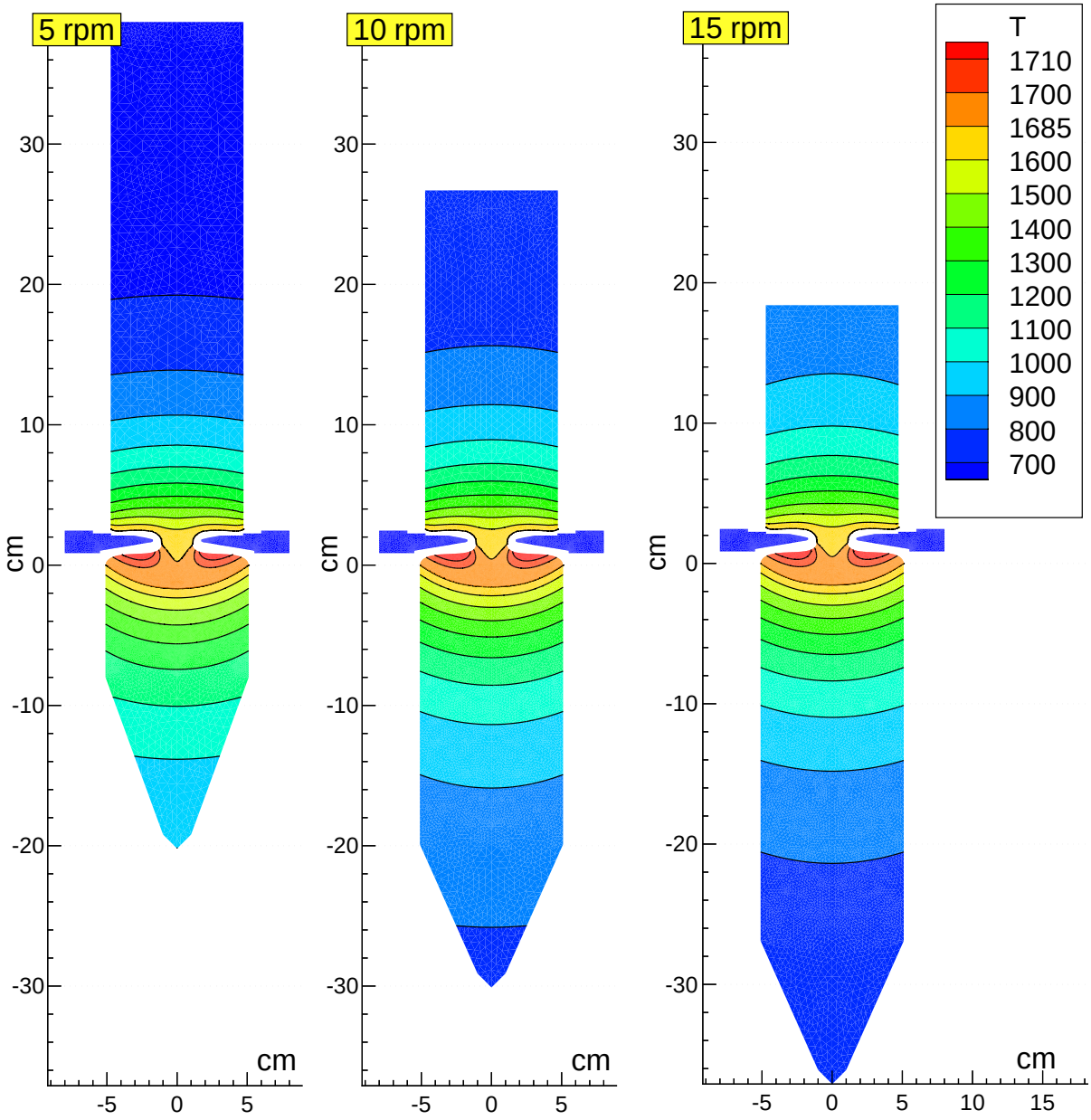

Figure 4.4. *Temperature field for the IKZ 4" configuration at the three stages of growth, calculated with FZ-Sim. Temperatures in* [K].

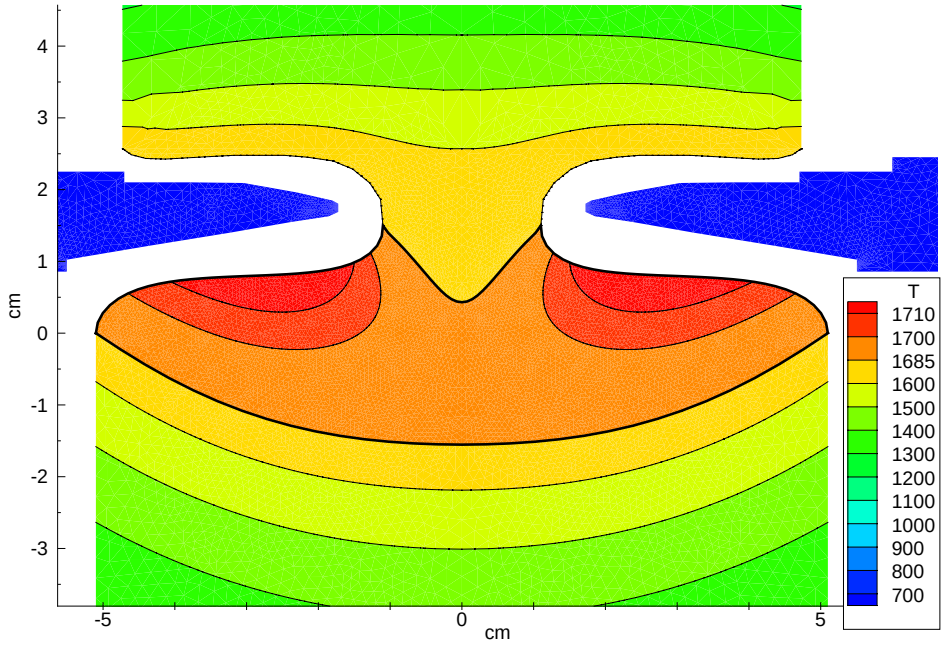

Figure 4.5. *Temperature field in the molten zone for the IKZ 4"-10rpm configuration. Temperatures in* [K].

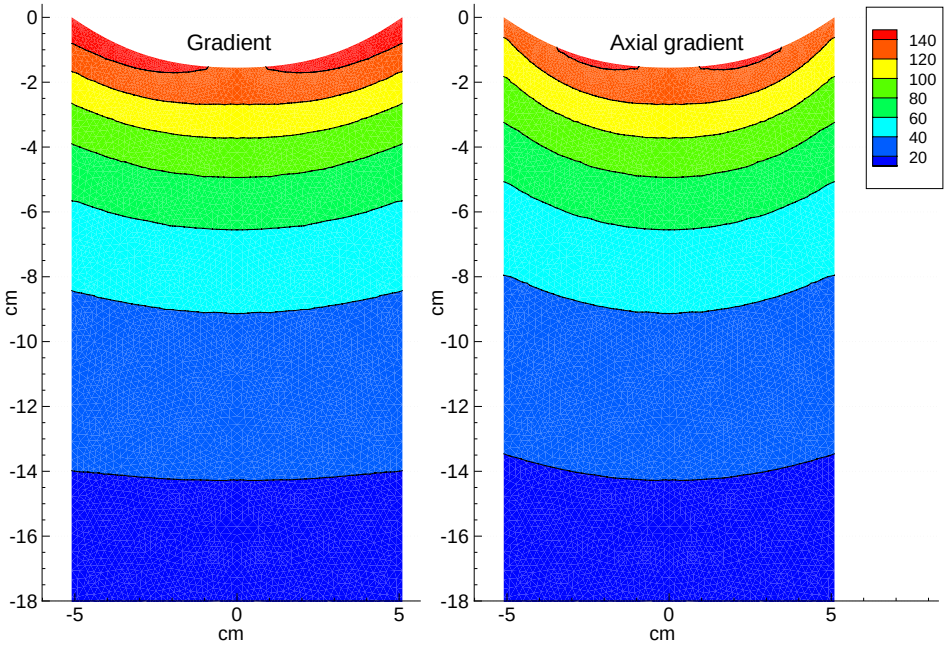

Figure 4.6. *Temperature gradients of the IKZ 4"-10rpm configuration. Left:* $|\vec{\nabla}T|$*, right:* $\partial T/\partial z$*. Gradients in* [K/cm].

	IKZ 4"-5 rpm	IKZ 4"-10 rpm	IKZ 4"-15 rpm
Experiment	17.2	15.7	15.4
Calculation	16.8	15.5	15.4

Table 4.2. *Depth of the lower phase boundary in* [mm] *for the IKZ 4" configuration. Measured in center,* $r = 0$.

The cooling of the crystal after solidification is handled by radiative heat loss (2.14), so the surface area of the crystal, being the limiting factor, is important for the temperature field. The three temperature fields in figure 4.4 show the influence of the length of the crystal on the temperature field, the longest crystal 15 rpm, has a larger surface area and therefore is cooled faster. The same situation is seen at the feed, where the longer feed is better cooled.

The dependence from the length of the crystal, on the cooling, can be verified by comparing measured and calculated depths of the lower phase boundary, as done in table 4.2. It is seen that there is good accordance between the measured and calculated lower phase boundary depths, supporting the assumption that the convection can be neglected in the determination of the phase boundaries. If the rotation, or convection at all, had a decisive impact on the shape of the lower phase boundary, then the good agreement between experiment and calculation in table 4.2 could not be obtained. The believe is therefore that convective heat transfer from the flow within the molten zone has negligible influence on the phase boundaries.

The phase boundary depths listed in table 4.2 have been measured using the LPS technique at IKZ. The actual scanning of the phase boundaries are shown in figure 4.7, where also the calculated phase boundaries are inserted. The figure shows good agreement between the experiment and the calculation, not only in the center, where the depth is measured, but over the full extent of the phase boundary.

Finally the temperature field for the IKZ 0.8" configuration is shown in figure 4.8. As mentioned the cooling of the crystal is handled by radiative losses, the surface area being the limiting factor. When the characteristic length scale, the radius of the crystal increases, then the volume of the crystal is scaled with $R^2_{crystal}$, but the surface area only scales with $R_{crystal}$. The surface area to volume ratio is therefore larger for the thin crystals, yielding faster cooling. This faster cooling can be seen by comparing figure 4.5 and figure 4.8. In the

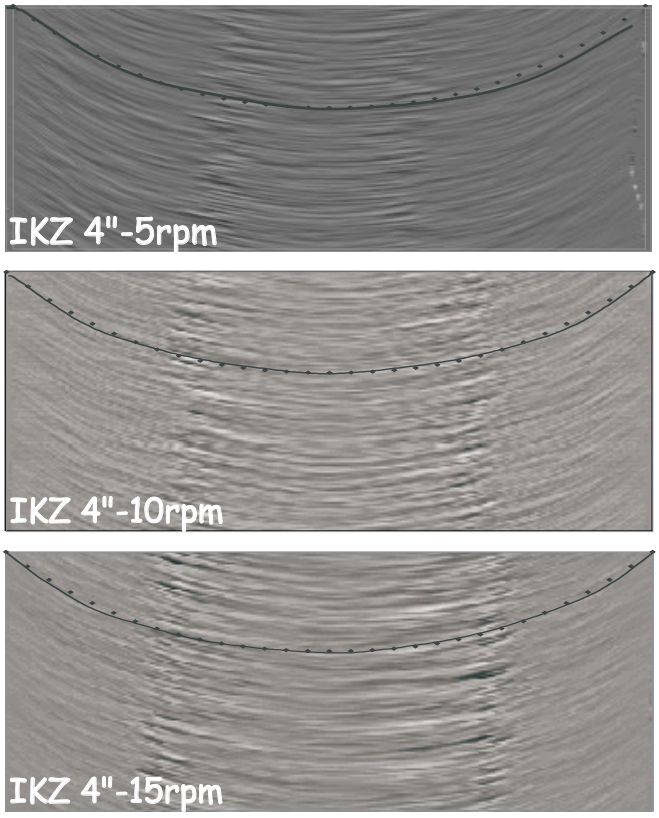

Figure 4.7. *LPS; measured (line) and calculated phase boundaries (dots) of the IKZ 4" configuration.*

4" process the temperature 3 cm below the triple point falls 315 K, whereas it falls 630 K for the 0.8" process.

In summary, the indirect verification of the heat transfer calculations using LPS measurements shows good agreement. The cooling of the crystal is handled by radiation, resulting in large temperature gradients in the high temperature area, just below the lower triple point. For the radiative cooling the surface area is the limiting factor, so there is an effect of length, where the longer crystal is cooled faster. This dependence on surface area can be extended to a thickness effect, where a thinner crystal has a larger surface to volume ratio, and hence is cooled faster. Finally there is an effect of the bulk motion of the crystal and feed giving a convective heat transfer, that can be seen on the temperature field.

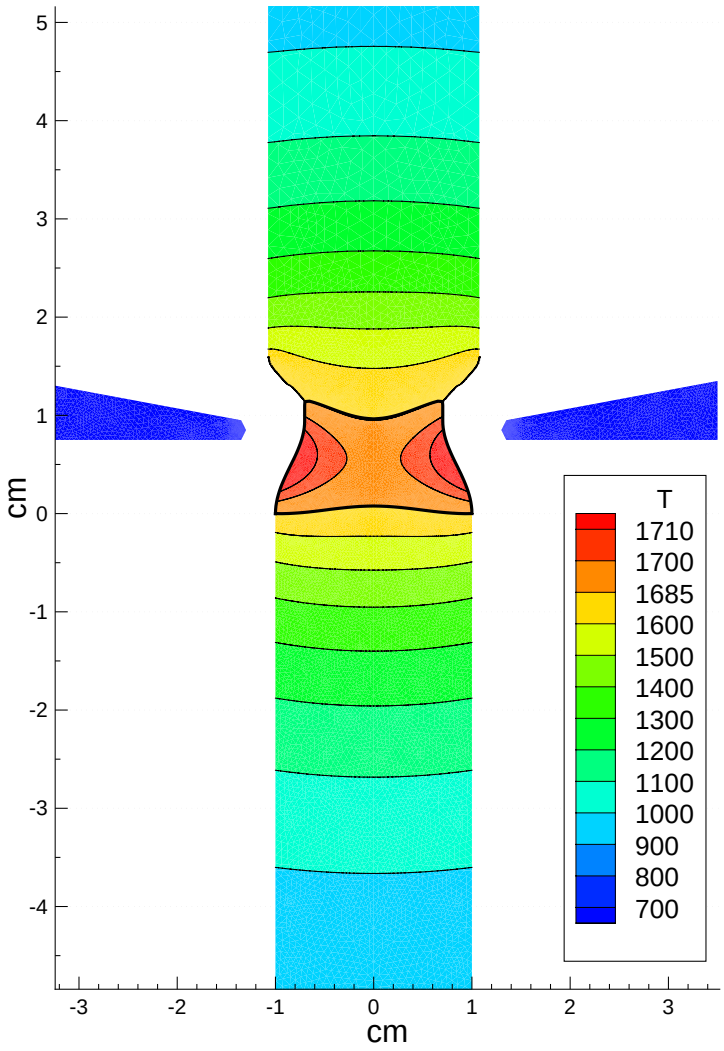

Figure 4.8. *Temperature field for the IKZ 0.8" configuration. Temperatures in* [K].

4.3 Convective cooling of the crystal

Floating zone crystals are commonly grown in a clean atmosphere comprised of mainly argon. After the crystal is pulled out of the molten zone, it is as shown in the previous section primarily cooled by radiation. However, the surrounding atmosphere is involved in an additional cooling, because the warm crystal induces a natural convection of gas, flowing along the crystal. Furthermore, in order to prevent arcing, floating zone crystals are often grown at gage pressures, which increases the density of the surrounding gas and hence the additional convective cooling.

It is the purpose of this study of convective cooling, published in [39], to investigate the influence of this convective cooling on the phase boundaries, the temperature field and the growth parameter $\xi = V_{Crystal}/G_0$, $V_{Crystal}$ being the pull speed of the crystal and $G_0 = |\vec{\nabla}T|$ the temperature gradient at the phase boundary.

Correlations for pressurized cooling

In order to model the effect of an increased pressure, a second term was added to the equation of heat loss to the surroundings (2.14), corresponding to a convective heat transfer

$$q_{loss} = \epsilon\sigma(T^4 - T_\infty^4) + \underbrace{h(T_S - T_\infty)}_{convection} \tag{4.1}$$

where T_S is the surface temperature of the crystal and T_∞ is the reference temperature of the surroundings. For giving an estimate of the local heat transfer coefficient h, the crystal is assumed to be a vertical and isothermal cylinder, using the logarithmic mean temperature difference $\Delta T_{logmean}$ [27], to determine the Grashof number Gr.

According to [20], the average Nusselt number $\overline{Nu}_l$ for a vertical isothermal cylinder can be calculated as

$$\overline{Nu}_l = \frac{4}{3} 0.508 Pr^{0.5} \left(0.952 + Pr\right)^{-0.25} Gr_l^{0.25} \tag{4.2}$$

where Gr_l and $\overline{Nu}_l$ are given by

$$Gr_l = \frac{g\beta l^3 \Delta T_{logmean}}{\nu^2} \qquad \overline{Nu}_l = \frac{\overline{h}_l \; l}{k_\infty} \tag{4.3}$$

Variable	Unit	1.9 bar	3.3 bar	8.0 bar
k	$[W/mK]$	0.034	0.034	0.034
Pr	-	0.661	0.661	0.661
β	$[1/K]$	$1.43 \cdot 10^{-3}$	$1.43 \cdot 10^{-3}$	$1.43 \cdot 10^{-3}$
ν	$[m^2/s]$	$3.26 \cdot 10^{-5}$	$1.86 \cdot 10^{-5}$	$7.69 \cdot 10^{-6}$
μ	$[kg/ms]$	$4.23 \cdot 10^{-5}$	$4.23 \cdot 10^{-5}$	$4.23 \cdot 10^{-5}$
ρ	$[kg/m^3]$	1.30	2.27	5.50
l	$[m]$	0.45	0.55	0.55
$\overline{Nu}_l$	-	84	125	194
$\overline{h}_l$	$[W/(m^2 \cdot K)]$	6.3	7.7	12

Table 4.3. *The physical properties of argon at 700 K and various absolute pressures [7, 33] and the calculated heat transfer. The length of the crystal l has been reduced 5cm from the real lengths, to accommodate for the reduced surface area of the conical part.*

An averaged heat transfer coefficient $\overline{h}_l$ can therefore be calculated for the new boundary condition (4.1) from (4.2) and (4.3).

The effect of the pressure change arises from the change in density of the surrounding gas, affecting the kinematic viscosity and therefore the Grashof number. For the regime considered, argon can be treated as an ideal gas, hence the density and expansion coefficient may be calculated according to the ideal gas law. The physical parameters used in the study are listed in table 4.3.

Results

The calculations including the extra convective term were conducted for the Topsil 4" configuration at absolute pressures of 0, 1.9, 3.3 and 8.0 bar. A crystal was grown at 1.9 and 3.3 bar, to be able to compare the depth of the phase boundaries with the numerics, see table 4.4. Phase boundaries of the grown crystal were measured using the LPS method. The two measured phase boundary profiles, overlayed with the calculated profiles, are shown

	0 bar	1.9 bar	3.3 bar	8.0 bar
Experiment	–	14.7	14.4	–
Calculation	15.4	15.0	14.8	14.5

Table 4.4. *Depth of lower phase boundary in [mm] for the pressurized Topsil 4" configuration. Measured in center, $r = 0$.*

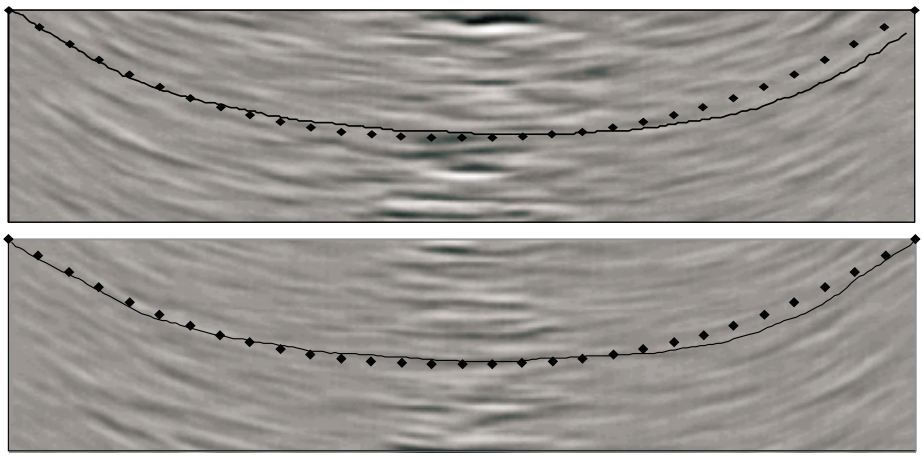

Figure 4.9. *LPS; measured (line) and calculated phase boundaries (dots).* Top: *1.9 bar.* Bottom: *3.3 bar.*

in figure 4.9. The calculations are seen to show good agreement with the experiments, indicating that the order of magnitude of the calculated convective cooling corresponds to the order of magnitude of the real cooling from the surrounding gas.

The calculation for 8.0 bar is included to show the extreme situation and is, as vacuum, *not* yet verified experimentally. Figure 4.10 shows the calculated temperature fields in the crystal for the four different situations considered. The pressure-induced additional cooling is clearly seen as the isotherms move upwards with higher pressure.

In the formation of point defects, the temperature gradients G_0 in form of the growth parameter ξ determines the type of generated defects, see section 6.1 page 77. The temperature gradients for different pressures, shown in figure 4.11, reveals larger gradients for increased pressure, corresponding to the increased cooling. These larger temperature gradients results in smaller values of ξ, see figure 4.12, and hence a larger probability for the generation of the undesired interstitial defects. The effect of going from 1.9 to 3.3 bar is seen to be small, but at higher pressure there is a definite lowering of the growth parameter.

More recent values of the critical growth parameter are substantially lower than the one used in the original Voronkov model [86]. A value of $\xi_{crit} = 2.23 \cdot 10^{-5} cm^2/K \cdot s$ has been reported by [16]. This results in vacancy dominated crystals for the 4" configurations considered, regardless of the pressure.

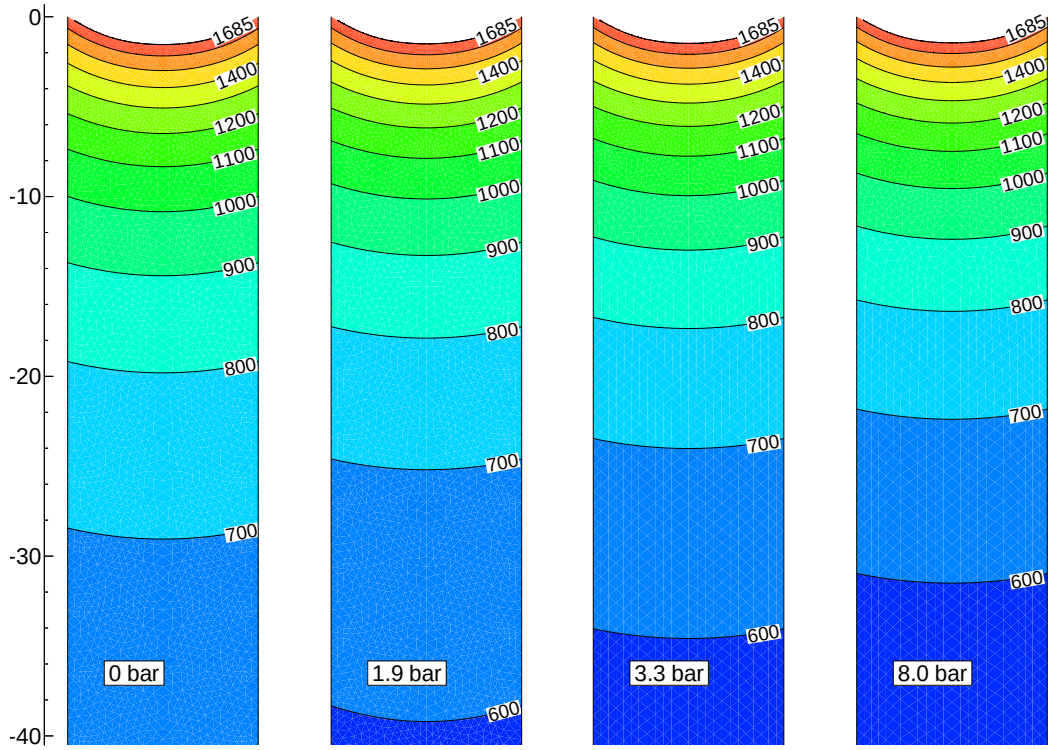

Figure 4.10. *Temperature fields of the Topsil 4" crystal in [K].*

In summary, the applied convective cooling seems to be of the right order of magnitude, because the calculation with the additional convective cooling matches the measurements. The effect on the generation of point defects is small, since the considered configuration is well within the vacancy region and the realized pressures are relatively small.

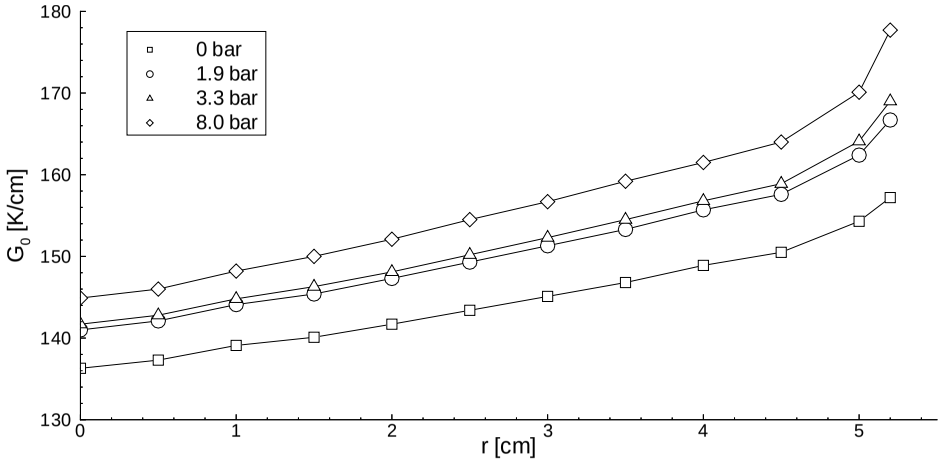

Figure 4.11. *Temperature gradients* $|\vec{\nabla}T|$ $2mm$ *below the lower phase boundary.*

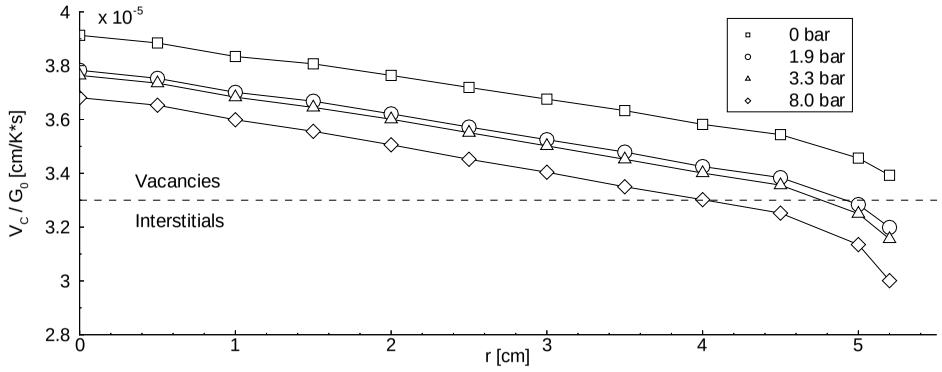

Figure 4.12. *The growth parameter* ξ. $V_{crystal} = 3.2mm/min$. *The critical value* $\xi_{crit} = 3.3 \cdot 10^{-5} cm^2/K \cdot s$ *is taken from [86].*

Chapter 5

Melt convection and dopant transport

This chapter describes the flow of molten silicon and the transport of dopant governed by the flow. The four driving forces of the flow are simulated individually in section 5.1, to elucidate their individual contribution to the total flow pattern qualitatively as well as quantitatively. Section 5.2 puts all the driving forces together to form the real unsteady flow. It encompassed the IKZ 4" and the Topsil 4" configurations to show the evolution of the flow in time. Finally section 5.3 provides simulations of unsteady dopant transport and the resulting resistivity profiles.

5.1 The driving forces of melt convection

Section 2.4 describes the mathematical models behind the four individual driving forces of the flow field.

- Buoyancy forces (natural convection)
- Thermocapillary forces (Marangoni convection)
- Tangential electromagnetic force (electrodynamic convection)
- Centrifugal forces (rotation)

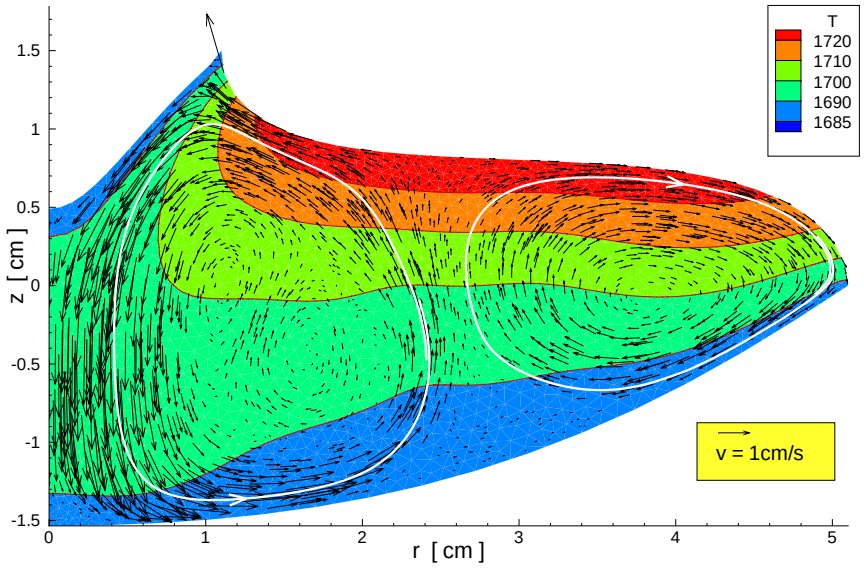

Figure 5.1. *Simulation of isolated natural convection, all other effects omitted. Velocities are of the order* 1 cm/s. *IKZ 4" configuration.*

Their isolated effect and magnitude will be simulated here for the IKZ 4" configuration. Appendix B provides a dimensional analysis of the driving forces.

For large crystals *buoyancy* is the strongest of the four driving forces, for a 4" configuration it is strong enough to produce an unsteady flow. There is, however, no evidence that the flow is turbulent and it is indeed solvable under laminar conditions. Furthermore there are no edges or other obstacles in the molten zone, that could act as vorticity generators to trip a transition to a turbulent flow.

The buoyancy flow shown in figure 5.1 is caused by a *radial temperature difference*, where the relatively colder fluid at the center flows downwards creating the inner vortex. The outer counter rotating vortex is simply driven by the inner vortex. An increased crystal diameter will have a strong effect on encountered velocities, because the maximum temperature is increased and the Grashof number, describing natural convection, scales with $R^3_{crystal}$. Therefore, sufficiently large diameters perhaps 8", might produce turbulent flow.

In contrast to natural convection, *Marangoni convection* is a surface driven flow, so the highest velocities are seen on the free surface. Figure 5.2 shows the isolated Marangoni flow, with all other driving forces omitted. The nature of the Marangoni convection is flow from areas of low surface tension towards areas of relatively higher surface tension. A

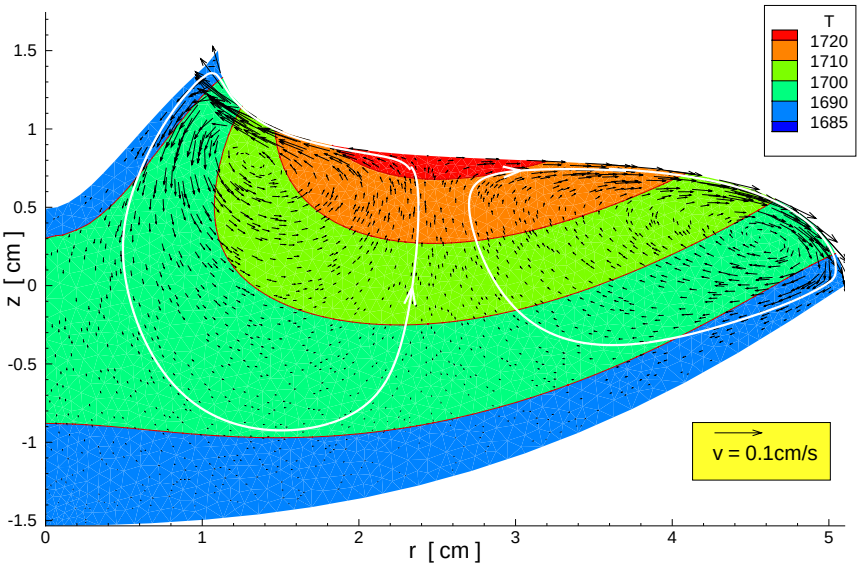

Figure 5.2. *Simulation of isolated Marangoni convection, all other effects omitted. Velocities are of the order* 0.1 cm/s. *IKZ 4" configuration.*

stagnation point is therefore seen at the point of highest temperature ($r \approx 2.6\,\mathrm{cm}$), from this point the flow splits, forming two counter rotating vortices driven by the variation of surface tension.

The effect of the Marangoni flow is weaker than the natural convection with velocities in the order of 0.1 cm/s, hence the flow is stationary. The effect of a larger crystal diameter is not expected to be as strong as for the natural convection, while the gradient of surface tension will remain in the same order of magnitude, and only the size of the free surface will increase, allowing for a larger area of attack. The Marangoni number scales linearly with $R_{crystal}$.

The *electromagnetic convection* driven by the tangential electromagnetic force is an effect in the same order of magnitude as the Marangoni convection, resulting in velocities around 0.1 cm/s. The pure electromagnetic convection, shown on figure 5.3 without other driving forces, is a surface-driven flow, since the skin layer of interaction is very thin ($\delta_{el} < 0.5\,\mathrm{mm}$, see figure A.2 page 108). The flow is independent of the temperature field and only a function of the geometry of the inductor, the applied frequency and power.

The azimuthal electric current on the free surface, which controls the electromagnetic force, is weak at the lower triple point, strongest at the point where there is the smallest distance

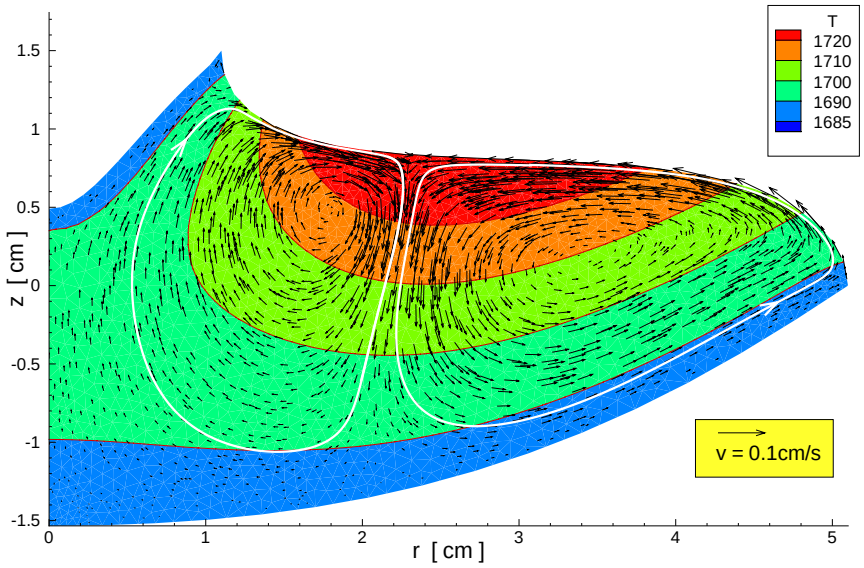

Figure 5.3. *Simulation of isolated electromagnetic convection ($f = 2.8\,\mathrm{MHz}$), all other effects omitted. Velocities are of the order* $0.1\,\mathrm{cm/s}$. *IKZ 4" configuration.*

to the inductor and then weak again at the upper triple point, see figure 4.1 on page 45. The eletromagnetic force is proportional to the derivative of the current (2.24), so it will be positive at the outer part of the free surface and then negative on the inner part, with a stagnation point at $r \approx 2.9\,\mathrm{cm}$. The outcome is therefore two counter rotating vortices, with opposite direction compared to the vortex pair for the Marangoni convection in figure 5.2.

The fourth and last driving force of the melt convection is the *centrifugal force* field, produced by rotation. The isolated effect of a 5 rpm crystal and -1 rpm poly rotation is shown on figure 5.4. The flow is driven from the two phase boundaries, with the lower phase boundary moving faster (5 rpm) and with a larger diameter, thus generating the larger vortex. The velocities generated by the rotation are in the order of $0.1\,\mathrm{cm/s}$.

One important property of the rotational flow is that it generates a flow at the lower phase boundary. This feature makes the rate of rotation important for the incorporation of dopant into the crystal, because the dynamics of this particular region determines the distribution of dopant in the grown crystal. The rotational effect scales quadratically with the radius of the crystal, so a change of diameter is expected to have an influence. The rate of rotation is, however, within some limits a parameter that can be chosen to engineer the desired flow pattern.

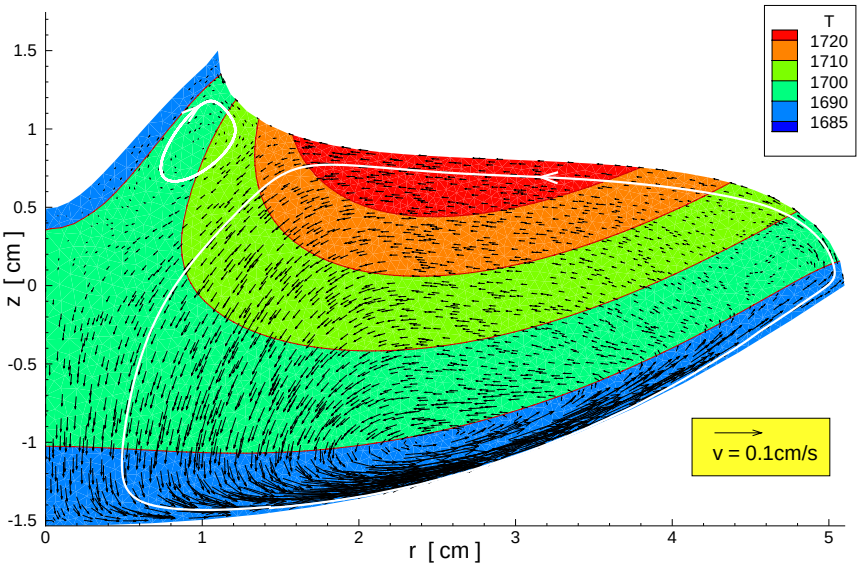

Figure 5.4. *Simulation of isolated rotation. 5 rpm crystal and -1 rpm poly rotation, all other effects omitted. Velocities are of the order* 0.1 cm/s. *IKZ 4" configuration.*

	IKZ 4"-5 rpm	IKZ 4"-10 rpm	IKZ 4"-15 rpm	Topsil 4"
Rotation of crystal [rpm]	5.0	10.0	15.0	6.0
Rotation of feed [rpm]	−15.0	−15.0	−15.0	−0.6
Pull speed [mm/s]	3.4	3.4	3.4	3.2

Table 5.1. *Configurations used for the unsteady flow simulations, geometrical data can be found in table 4.1, page 44.*

5.2 Unsteady melt convection

This section will provide simulations of the unsteady flow for the IKZ 4" and the Topsil 4" configurations, which are results of the interaction of all the four driving forces described in the previous section. With respect to melt convection, the difference in the two versions of the Topsil 4" configuration is only the small difference in the depth of the phase boundary, hence the calculation will be only on the 1.9 bar pressure, designated: Topsil 4". This section is connected to section 5.3, that treats the unsteady dopant transport, in the sense that the velocity fields calculated here are used for the dopant transport. Table 5.1 provides the details of the different configurations simulated here and in section 5.3.

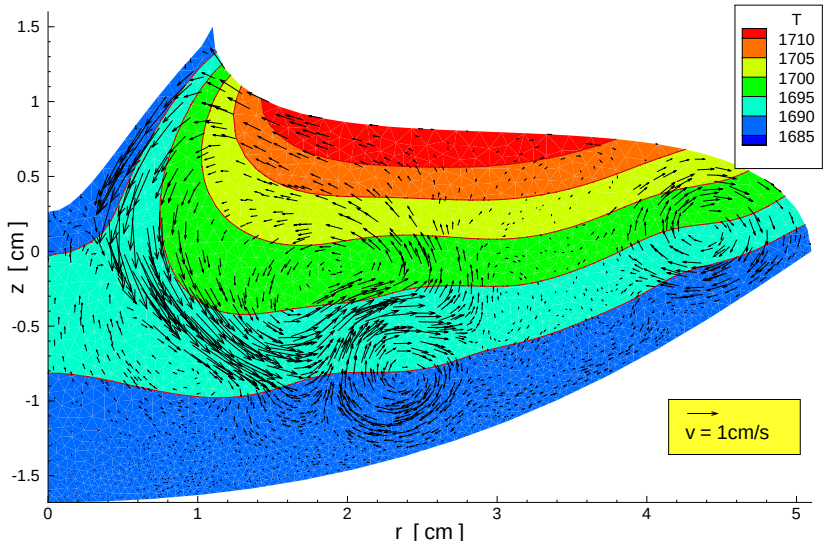

Figure 5.5. *Temperature field influenced by the unsteady flow of the IKZ 4"-5rpm configuration.* $t = 213.0\,\mathrm{s}$ *as in the first frame of figure 5.6.*

The temperature field of the molten zone is affected by the melt convection, as shown for the IKZ 4" - 5rpm configuration in figure 5.5. Even with the low Prandtl number ($Pr = 0.013$), the convection perturbs the temperature field of the quiescent molten zone, used in the conduction solution, see figure 4.5 page 50. However, the perturbation has negligible influence on the shape of the phase boundaries, as shown by the comparison with the LPS measurements. Both natural and Marangoni convection are driven by temperature differences, so the varying temperature field yields driving forces varying in time.

The stream function of the fully developed unsteady flow for the IKZ 4"-5rpm configuration is shown in figure 5.6. The flow consists of two counter rotating vortices, the outer rotating clockwise. Even though the rotational symmetric melt convection model does not include the varying heat input from rotating past the inductor gap, the flow is still unsteady, but fortunately laminar. The instability is seen as vortices sweeping the lower phase boundary at $1 < r < 3$. The pattern that is seen for the 7 second time frame shown in figure 5.6, where a small torus-shaped[1] vortex is generated and then transported outwards around the larger inner (red) vortex, repeats itself indefinitely. The generation and transport of these small vortices affects the shape of the larger inner vortex, whereas the more concentrated outer vortex remains undisturbed.

[1]Note that the flow is rotational symmetric and therefore constant in the azimuthal θ direction.

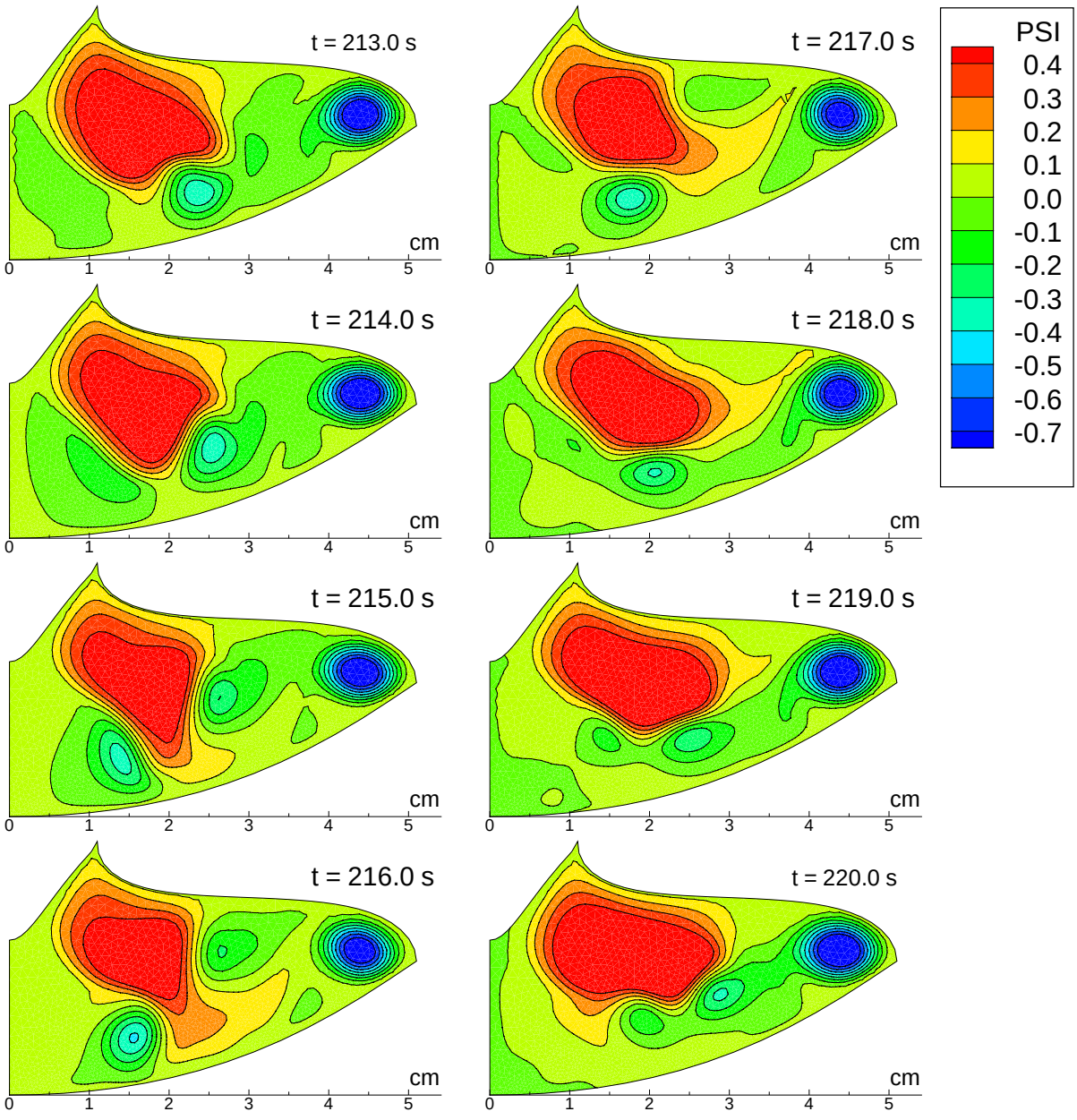

Figure 5.6. *Unsteady flow of the IKZ 4" - 5 rpm configuration. The stream function (psi) is positive for counter-clockwise and negative for clockwise rotation.*

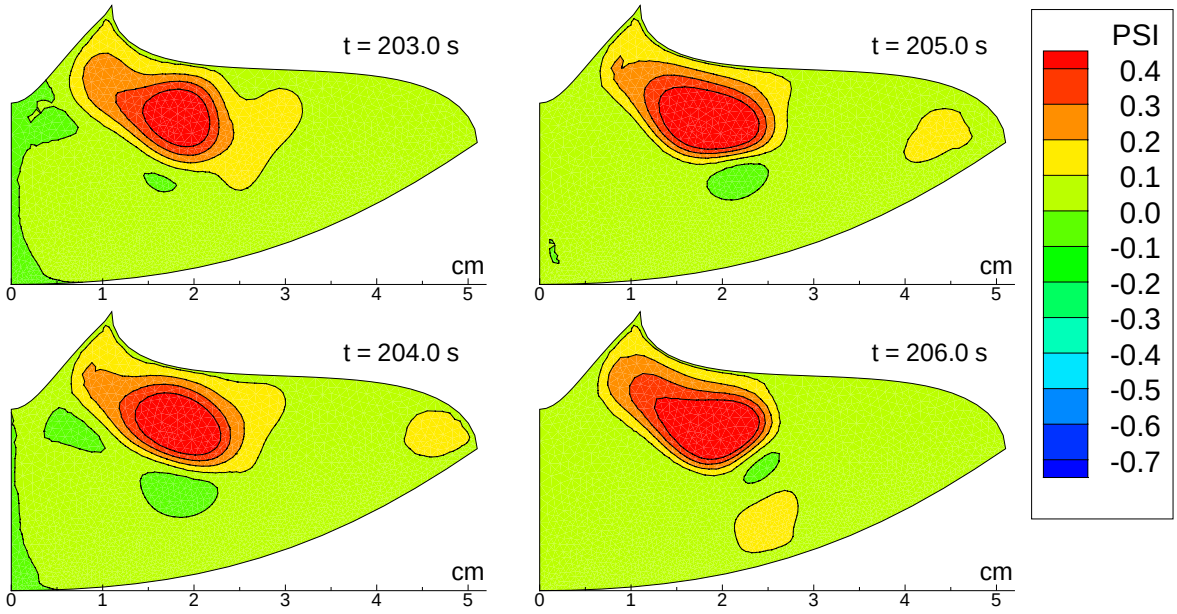

Figure 5.7. *Unsteady flow of the IKZ 4" - 10 rpm configuration. The stream function (psi) is positive for counter-clockwise and negative for clockwise rotation.*

The outer vortex is driven by the buoyancy and Marangoni forces and counteracted by the electromagnetic and rotational forces, see figure 5.1 - 5.4. An increased rate of rotation therefore represses the outer vortex and at higher rates, the entire flow field.

The unsteady simulation of the IKZ 4" configuration with 10 rpm crystal rotation is shown in figure 5.7. The inner vortex is smaller and pushed towards the upper phase boundary, compared to 5 rpm rotation, and the outer vortex is almost completely repressed. Furthermore the instabilities of the flow are diminished and the emerging vortexes do not sweep the phase boundary, as seen by the 5 rpm configuration.

The trend of the damped flow at 10 rpm compared with 5 rpm rotation, is continued at 15 rpm, as shown in figure 5.8. Here all flow at the outer part of the molten zone has ceased and the inner vortex is repressed further. The flow is now virtually steady. Note that the same legend is used in figures 5.6 - 5.8, so the velocities in the (r, z) plane are diminished at higher rates of rotation. The maximum velocities are given in table 5.2.

Melt convection of the IKZ 4" configuration has been simulated in [46, 57, 85], where the tendency of a repressed outer vortex is also seen for increased rotation. The outer vortex in the flow simulations presented here is, however, almost completely repressed at 10 rpm,

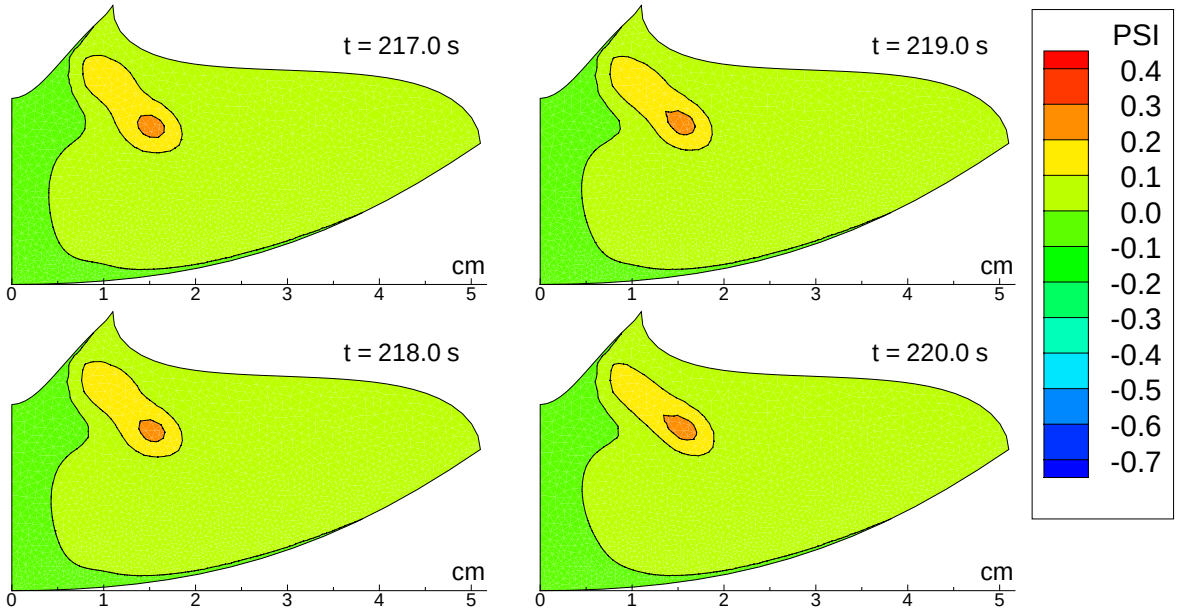

Figure 5.8. *Unsteady flow of the IKZ 4" - 15 rpm configuration. The stream function (psi) is positive for counter-clockwise and negative for clockwise rotation.*

which in the quoted references first takes place at rotations of 15-20 rpm. This discrepancy is believed to be caused by differences in the flow solvers, especially in the implementation of and input to the electromagnetic force.

The unsteady melt convection for the Topsil 4" configuration is shown in figure 5.9. As with the most comparable of the IKZ 4" configurations, the 5 rpm, the overall flow pattern has two counter rotating vortices. This configuration is almost steady, except for a small vortex being generated at the outer (blue) vortex, that moves inward and up. So compared to the IKZ 4", the instability is at the outer vortex ($3 < r < 4$), instead of at the inner vortex, and the Topsil 4" configuration is more stable, note same graduation of the streamfunction.

Maximum velocity	IKZ 4"-5 rpm	IKZ 4"-10 rpm	IKZ 4"-15 rpm	Topsil 4"
(r,z) plane [cm/s]	2.1	1.5	1.2	2.4
(r,θ,z) plane [cm/s]	2.7	5.3	8.0	3.3

Table 5.2. *The maximum velocities. In the (r,θ,z) plane the max velocity is realized at the lower triple point in all cases.*

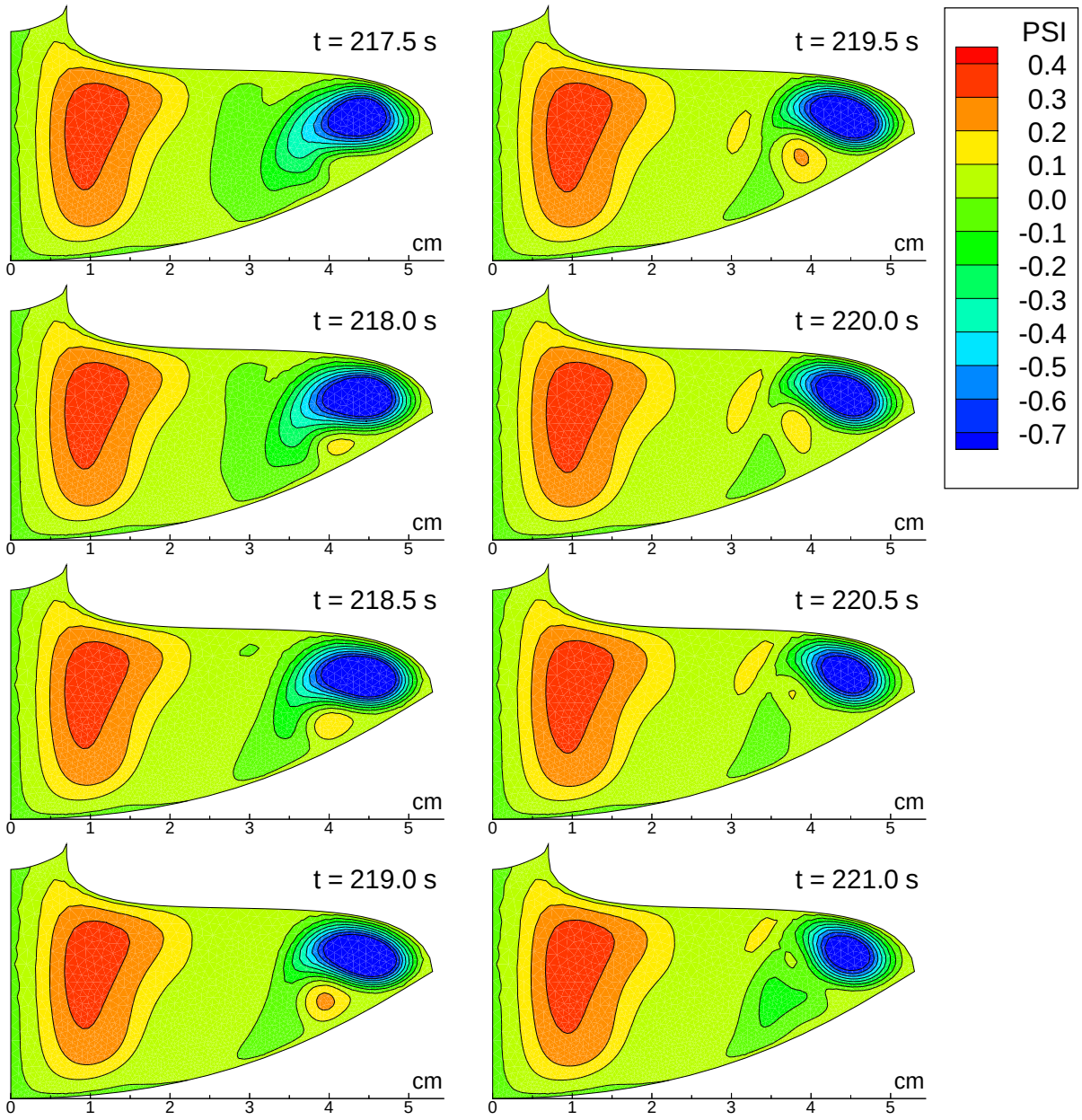

Figure 5.9. *Unsteady flow of the Topsil 4" configuration. The stream function (psi) is positive for counter-clockwise and negative for clockwise rotation.*

5.3 Unsteady dopant transport

The transport of dopant, controlled by the time-dependent flow, is described in this section. The dopant concentration field throughout the molten zone is calculated and the incorporated dopant at the lower phase boundary used to determine the radial resistivity distribution is described in section 5.3.1. The dopant transport simulated in this work will only encompass *phosphorus*, but other dopants such as boron could be simulated just by changing the diffusivity and the segregation constant.

The low diffusivity of phosphorus results in convection dominated transport even at these relative low velocities, with a solutal Peclet number about $Pe_C \approx 1.5 \cdot 10^4$, see appendix B. Even though the solutal Peclet number is high, the diffusion still affects the transport. According to [59] the diffusivity of phosphorus in silicon is not known precisely ($2.3 - 5.1 \cdot 10^{-8}\,\mathrm{m}^2/\mathrm{s}$), hence some inaccuracy could be contributed to the magnitude of the diffusivity. The purpose of this work is not a parameter study, so this assumption is not investigated in this thesis.

For the incorporation of dopant into the crystal, the decisive part of the flow field is the dynamically changing *momentum boundary layer* in the vicinity of the lower phase boundary, since the dopant incorporation *does not* take place under equilibrium conditions. The concentration directly at the phase boundary, which accounts for the amount of incorporated dopant and hence the local resistivity, depends strongly on the thickness of the concentration boundary layer. The buildup of the only diffusion related concentration boundary layer, resulting from the segregation, demands quiescent fluid and is therefore restricted by the thickness of the momentum boundary layer. This yields thicker concentration boundary layers and thereby higher concentrations, at the phase boundary in stagnation areas of the flow as shown in [46].

In the numerical solution the buildup of the concentration boundary layer to a quasi stationary state takes time, since it is done within the momentum boundary layer and hence governed by diffusion. To deal with the buildup, without wasting too much computational effort, the time step size is artificially increased by a factor 100 in the first few time steps. In this manner, the first time steps provides a very good initial guess, with respect to the concentration boundary layer, but of course not a physically correct solution. Some detail on the start up of the calculation is given in appendix C.

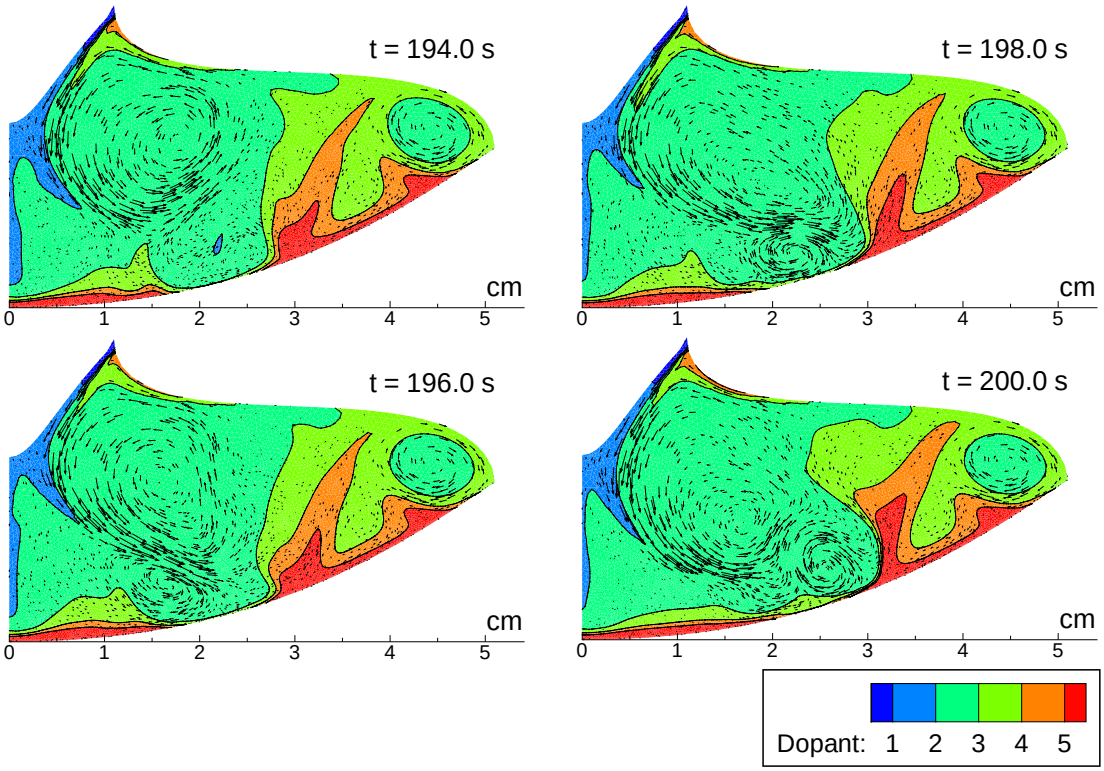

Figure 5.10. *Unsteady dimensionless dopant concentration field for the IKZ 4"-5 rpm configuration.*

In an attempt to simulate the real gas phase doping of the process, the dopant is added by prescribing a flux (5.1) through the inner part of the free surface.

$$q = \begin{cases} q_0 \sin\left(\pi \frac{r-r_1}{r_2-r_1}\right) & r_1 \leq r \leq r_2 \\ 0 & r > r_2 \end{cases} \tag{5.1}$$

where $r_1 = 1.1\,\text{cm}$, $r_2 = 2.4\,\text{cm}$ and $q_0 = -0.03$. The concentrations and fluxes are dimensionless, since the interest is in the relative differences, not the absolute levels. No significance should therefore be attributed to the absolute levels of concentration in figures 5.10 - 5.12.

The unsteady dopant concentration field of the IKZ 4"-5 rpm configuration is shown in figure 5.10. The first observation to make, is the increased dopant concentration at the lower phase boundary, caused by the segregation. The extent of this dopant concentration

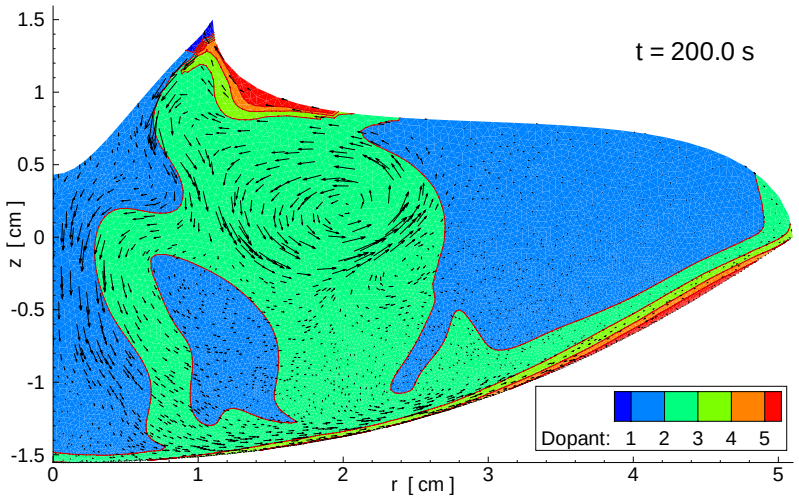

Figure 5.11. *Unsteady dimensionless dopant concentration field for the IKZ 4"-10rpm configuration.*

layer is seen to be flow-dependent, it is allowed to build up in more tranquil regions e.g. $3 < r < 4$. The increased concentration at $r = 4$ is caused by vortices carrying the higher concentration at the boundary layer, outwards. The buildup at $0 < r < 1.5$ is caused by a separation point at $r = 1.5$ carrying the dopant outwards and a stagnation area at $r = 0$ yielding a diffusive buildup.

The 5 rpm configuration is the most oscillating of the ones simulated, so as expected there is a distinct influence from the instability of the melt convection on the dopant concentration field. The oscillations in the concentration field are especially seen in the region $1 < r < 3$, where the vortices sweep the lower phase boundary. The oscillations will also be seen in section 5.3.1, focusing on the concentration *at* the phase boundary.

The flow field for the IKZ 4"- 10 rpm configuration is more stable, than for the 5 rpm rotation, hence only one time step is shown.. The concentration field, shown in figure 5.11, therefore only encompasses *one time step*, since the changes are hard to see. The concentration field reveals a well-defined concentration boundary layer in the more quiescent outer region ($3 < r < 5$). The more calm flow of the 10 rpm configuration also results in lower concentrations in the molten zone, because of the reduced convective mixing. The reduced mixing can especially be seen at the part of the free surface, where the gas phase doping takes place.

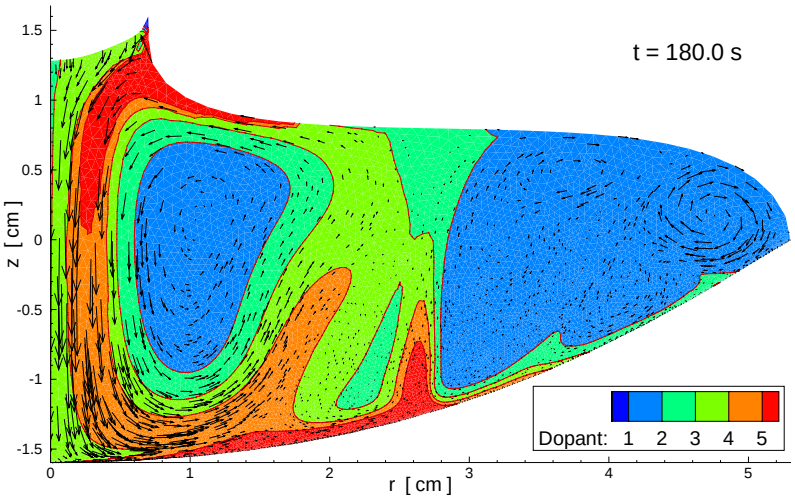

Figure 5.12. *Unsteady dopant concentration field for the Topsil 4" configuration.*

The dopant concentration field for the IKZ 4" - 15 rpm configuration is similar to the concentration field of the 10 rpm, as can also be seen from the resistivity profile in figure 5.13. It is therefore not included.

The instabilities of the melt convection for the Topsil 4" configuration (figure 5.9), do not result in noticeable oscillation of the fully developed concentration field, hence only *one time step* is shown in figure 5.12. The doping method is given by (5.1), but with $r_1 = 0.7\,\mathrm{cm}$ and $r_2 = 2.0\,\mathrm{cm}$, due to geometrical differences. For this configuration there is a strong flow past the doping area, so as for the IKZ 4" - 5 rpm configuration, there is a significant convective mixing of the dopant entering through the free surface. The vortices extend all the way to the lower phase boundary, pulling the concentration boundary layer away from the lower phase boundary both at $1 < r < 2$ and the $r = 4.6$. By closer inspection, it can be established that the concentration buildup at $r = 2.6$, is at the separation point of two vortices. Hence the concentration boundary layer is not to the same extent repressed by the momentum boundary layer and is therefore allowed to grow, furthermore there is also a convective transport away from the phase boundary from the two vortices.

In summary, for the case without any convection, the solution is a uniform concentration boundary layer of about 1 mm in thickness as described by the Burton, Prim, Slichter theory [9], whereas the dynamics of the convection and the non-equilibrium segregation yields a more complex result. The thickness of the concentration boundary layer is strongly

affected by the melt convection, so if the flow sweeps the phase boundary resulting in a thin momentum boundary layer, then the concentration boundary layer is restricted to this thin region. The melt convection can furthermore pull the concentration boundary layer into the free stream, for instance, at a separation point of a vortex, reaching all the way to the lower phase boundary.

5.3.1 Resistivity profiles

The convective dominance of the dopant transport yields a possibility of indirect verification of the flow calculations by measuring resistivity profiles. Molten silicon is opaque to visible light and very hot, so besides comparison with other numerical codes and comparison of calculated and measured resistivity profiles, there are limited means of verifying the flow calculations. The reason for the interest in calculation of resistivity profiles, besides for validation purposes, is that a uniform dopant distribution is one of the prime quality parameters of the crystals grown by the industry. Calculated resistivity profiles can therefore be used for optimization of a given configuration.

Resistivity profiles are usually measured from the cut crystal or from a wafer in radial direction over a diameter. In calculating the resistivity profiles by (2.28), the concentration at the lower phase boundary is normalized by the average of the concentration at the phase boundary. The calculated resistivity profiles are mirrored in $r = 0$ to display the resistivity over a diameter as it is common in the measurements.

The calculated resistivity profiles for all three IKZ 4" configurations are shown in figure 5.13, each with 10 curves, that are 2 seconds apart. The inclusion of several curves is done to be able to describe the instability of the calculated processes. It is quite clear that the 5 rpm is the most unstable of the three, especially in the region from $1 < r < 3$, as also seen in the convection calculations. The 10 rpm as well as the 15 rpm do also exhibit some instability in the region $r < 3$, however, not to the same extent as the 5 rpm.

The measured resistivity profiles for the IKZ 4" configurations are shown in figure 5.14. It should be noted that the experimental data for the IKZ 4" configurations only consists of *one measurement*, and therefore is the equivalent of *one* of the calculated curves in figure 5.13. The calculated axisymmetric instabilities give an indication of the variations

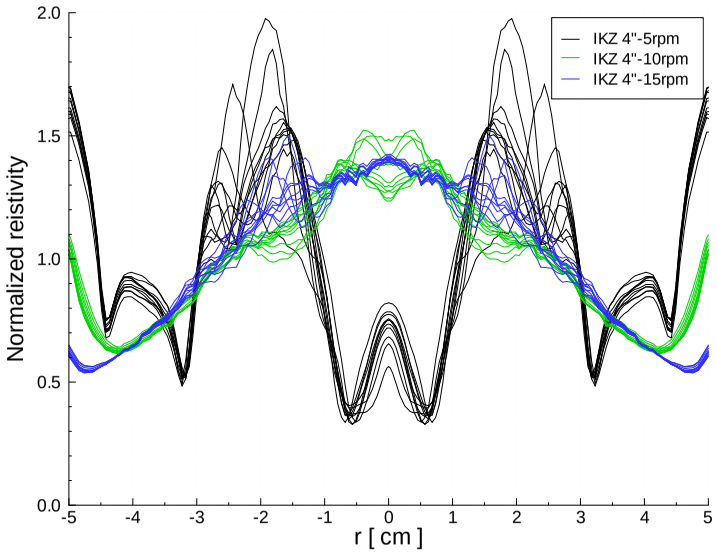

Figure 5.13. *Calculated normalized radial resistivity profile for the all three IKZ 4" configurations. For each configuration there are resistivity profiles for 10 different time steps within 20 seconds.*

of the resistivity profile, but even for the Topsil 4", which is quite stable the measured resistivity profile (figure 5.16) reveals instabilities beyond the calculated.

Comparison of the calculated 5 rpm profile with the measured reveals differences especially at the center, where the calculation seems to be stable, but with low resistivity contradicting the measurement. The minimum of the measured profile is at about $r = 2$, whereas the calculated is at $r = 3$, both with an increase in resistivity towards the edge of the crystal. The 10 rpm and 15 rpm both have the high resistivity in the center as the measured, but the minimum is shifted outwards. The 10 rpm differs from the 15 rpm by having the minimum a little closer to the center, as is also the case for the measured profiles.

Resistivity profiles for the IKZ 4" configurations have also been calculated by The Institute for Electroheat [56], with results differing from the ones obtained here. The differences are attributed to differences in the flow field, see page 66, as well as a different method of doping. The absence of the outer vortex for the higher rates of rotation, does influence the stagnation point and therefore also the point of minimum resistivity.

The calculated resistivity profile for the Topsil 4" configuration, that corresponds to the flow fields shown in figure 5.9, can be found on figure 5.15. The measured resistivity profile,

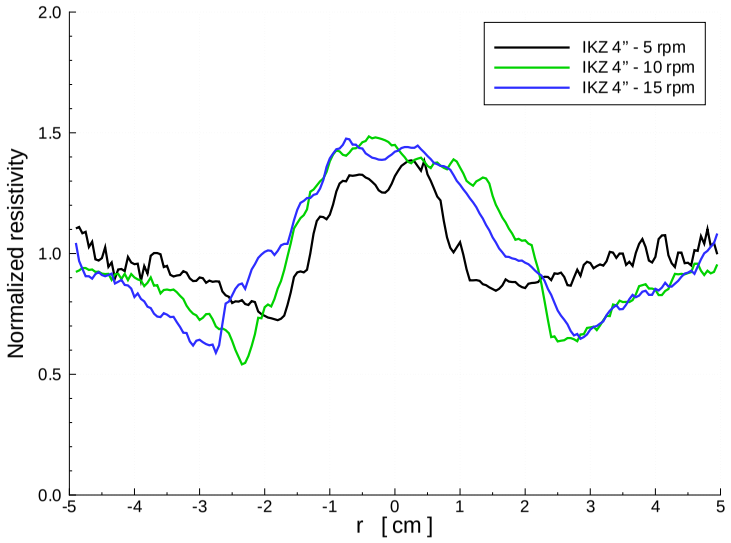

Figure 5.14. *Experimental normalized radial resistivity profile for the IKZ 4" configuration at the three rates of rotation. The curves each represent* one *measurement, not an average.*

shown in figure 5.16, is made up of measurements of 18 different wafers, which provides some insight on the instabilities of the real process, that the model tries to simulate. The calculated profile show a local maximum in the center like the measured, then a decrease towards a minimum at $r = 2.5$, which is shifted outwards compared to the experiment. Then the resistivity is increasing towards the edge, with good agreement with the measured, e.g. at $r = 4$. Note that the calculated resistivity profiles are very stable, except for a small region around $r = 3.5$, corresponding to the small vortex being generated at the outer more stable vortex in figure 5.9.

In common for all the calculated profiles is therefore an agreement with the measured profiles to an extent, as could be expected, given the restrictions of the model and the reservations of the measurements. One common characteristic is the jagged shape of the calculated profiles, with many local minima and maxima. In the Topsil 4" configuration for instance, the calculated profile should be comparable to the red average curve, but it is not quite as smooth. This type of discrepancy could be attributed to, a too low diffusivity in the calculations, but these local minima and maxima are more likely caused by the rotational symmetric melt convection calculation, being more stable a the real process, allowing these isolated extremes.

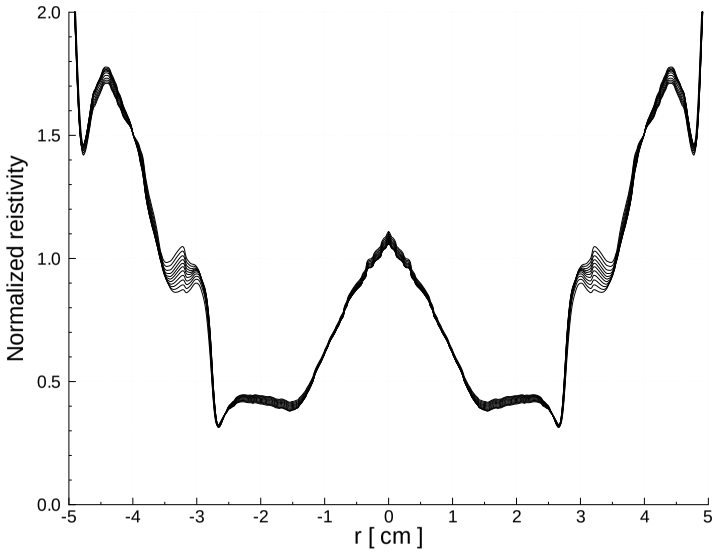

Figure 5.15. *Calculated normalized radial resistivity profile for the Topsil 4" configuration. The black curves are calculations of 10 different time steps within 20 seconds.*

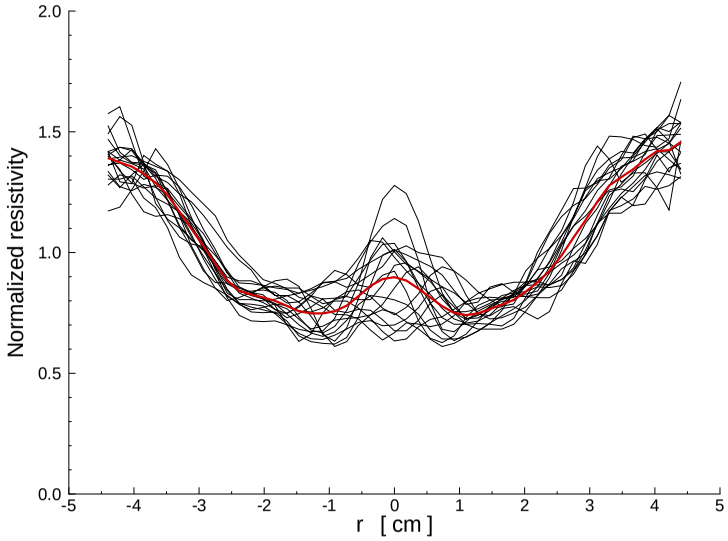

Figure 5.16. *Experimental normalized radial resistivity profile for the Topsil 4" configuration. The black curves are measurements of 18 different wafers and the red curve is the average.*

Chapter 6

Defects

This chapter deals with the transport of point defects. First the basic theory of Voronkov, for determining whether a grown crystal is dominated by vacancies or interstitials, is outlined in section 6.1. Then the defect model is used to calculate defect transport for the IKZ 0.8" configuration in section 6.2, where the calculation is compared with DLTS measurements from [41], confirming the model. Finally section 6.3 extends the model to the IKZ 4" and Topsil 4" configurations and determines the levels of vacancies and interstitials.

6.1 Voronkov theory

This section gives a short overview of the Voronkov theory, for determining which type of point defect will prevail in the grown crystal depending on the growth parameter ξ (6.1)

$$\xi = V_{crystal}/G \tag{6.1}$$

where G is the axial temperature gradient and $V_{crystal}$ is the pull speed. The theory, published in [86], is not restricted to any particular growth process. In short it states

$\xi < \xi_{crit}$: *Interstitial* type point defects dominate.

$\xi = \xi_{crit}$: No defects, vacancies and interstitials neutralize each other.

$\xi > \xi_{crit}$: *Vacancy* type point defects dominate.

Voronkov reported a value of $\xi_{crit} = 3.3 \cdot 10^{-5} cm^2/K \cdot s$, but more recent measurements of crystals grown with the Czochralski process [16], puts the value of the critical growth parameter[1] to $\xi_{crit} = 2.23 \cdot 10^{-5} cm^2/K \cdot s$. This later value has experimentally been supported for small diameter float zone crystals by [71].

The simplified physical explanation of the significance of the growth parameter given here is taken from [16]. At the lower phase boundary both vacancy and interstitial type point defects are incorporated at equilibrium concentrations, and then transported by convection and diffusion into the crystal. For the transport away from the phase boundary (at melting point temperature), there are two significant differences between vacancies and interstitials, that are decisive for their transport, see equations (A.1 -A.4) in appendix A.

$$D_I \approx 10\ D_V$$
$$C_V^{eq} \approx 1.2\ C_I^{eq}$$

Since the recombination process is very fast at temperatures just below the melting point, the concentrations of vacancies and interstitials will predominantly follow the equilibrium concentration in the first hot part of the crystal. The equilibrium concentrations are purely functions of temperature and therefore, there is a direct coupling between the temperature gradient at the lower phase boundary and the concentration gradient, governing the diffusion. High temperature gradients, therefore, imply high diffusion and vise versa.

The two extreme situations are therefore.

$\xi \ll \xi_{crit}$ **:** Low pull speed, vanishing convective transport and therefore *interstitial dominance*, because of the higher diffusivity of interstitials.

$\xi \gg \xi_{crit}$ **:** Isothermal crystal, no diffusion and therefore *vacancy dominance*, because of the higher initial concentration of vacancies.

The ratio of the pull speed $V_{crystal}$ and the temperature gradient G at the phase boundary is therefore the decisive parameter in determining which of the two situations prevails. In theory the situation, where the growth parameter equals the critical value, corresponds to an equal amount of the two types of defects being transported into the crystal, which at high recombination causes them to neutralize each other completely.

[1] Note that SI units are used as in [86], the *numerical value* therefore differs from [16].

6.2 Thin crystal - 0.8"

The fundamental difference between the thin 0.8" crystal and the thicker 4", is the larger temperature gradients in the 0.8" crystal and therefore, since the crystals were grown with the same pull velocity, the lower growth parameter. Figure 6.1 shows ξ given by (6.1), for the IKZ 0.8" configuration. It is seen that, according to the Voronkov theory, the entire crystal is expected to be dominated by interstitials, but with concentrations of vacancies at a comparable level in the center.

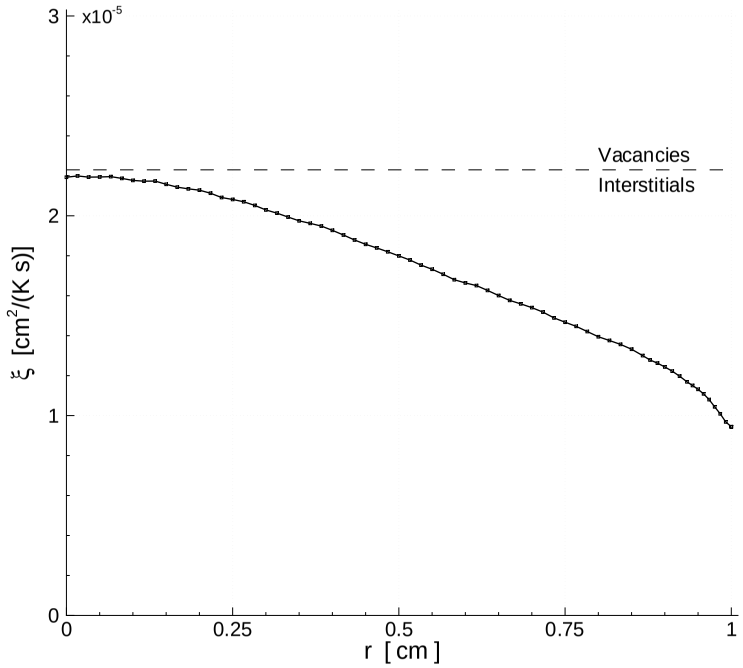

Figure 6.1. *The growth parameter ξ for the IKZ 0.8" configuration, $\xi_{crit} = 2.23 \cdot 10^{-5} cm^2/K \cdot s$ taken from [16].*

In doing the simulation of the defect transport there are a number of uncertainties in the physical parameters that needs some attention. In the transport equation (2.29) there are several physical parameters: diffusivities (D_V and D_I), equilibrium concentrations (C_V^{eq} and C_I^{eq}) and the recombination factor k_{IV}, that have to be estimated from atomistic simulation [47, 48, 79] or correlated from experiments [16, 40, 77, 78]. Both the diffusivity and the equilibrium concentrations are only known within some level of certainty, but with fair agreement throughout the literature [8, 19, 40, 78]. Older articles, however, have quite

different values of the equilibrium concentrations and diffusivities [23,83,86], indicating that this is a new area of research, and that these parameters have not been well established for a long time.

The correlations for the recombination factor are still quite different throughout the literature. Appendix A, describes the different physical parameters in the model and figure A.1, page 108, gives some of the correlations found in the literature for the recombination factor. In this work two different recombination factors will be applied

- *Dornberger* [17], given by (A.5).
- *Lemke* [40], given by (A.6)

The IKZ 0.8" configuration is particularly interesting since it has been examined using DLTS measurements and that experimental results therefore exist for comparison with the simulations, see section 6.2.1

The calculated concentrations of vacancy C_V and interstitial C_I type defects, using the recombination factor from Lemke, are shown on figure 6.2. The incorporation of defects at the phase boundary is at equilibrium concentrations of $C_V^{eq}(T_{melt}) = 1.22 \cdot 10^{15}\,\mathrm{cm}^{-3}$ and $C_I^{eq}(T_{melt}) = 9.92 \cdot 10^{14}\,\mathrm{cm}^{-3}$, respectively. At the high temperature the recombination is fast and the concentration of both defect types drop rapidly within the first 2 cm of the crystal. The crystal is seen to be dominated by interstitial-type defects everywhere, with vacancy concentrations in radial direction from $5 \cdot 10^{10}\,\mathrm{cm}^{-3}$ to below $1 \cdot 10^{9}\,\mathrm{cm}^{-3}$ and interstitial concentrations from $5 \cdot 10^{13}\,\mathrm{cm}^{-3}$ to $1 \cdot 10^{14}\,\mathrm{cm}^{-3}$. The calculation with the Lemke recombination factor therefore contradicts the Voronkov theory, predicting comparable levels of vacancies and interstitials in the center.

As expected from the radial distribution of the growth parameter ξ in figure 6.1, the concentration of vacancies is largest in the center and declining outwards, whereas the opposite is the case for the interstitial concentration. It has to be noted that both, the diffusivities as well as the recombination factor, drop rapidly for decreasing temperatures, hence only the first part of the crystal is shown, whereafter the defects are immobilized and the concentration therefore remains unchanged.

The defect concentrations for the IKZ 0.8" configuration using the Dornberger recombination factor are shown in figure 6.3. The recombination at high temperature is seen to be

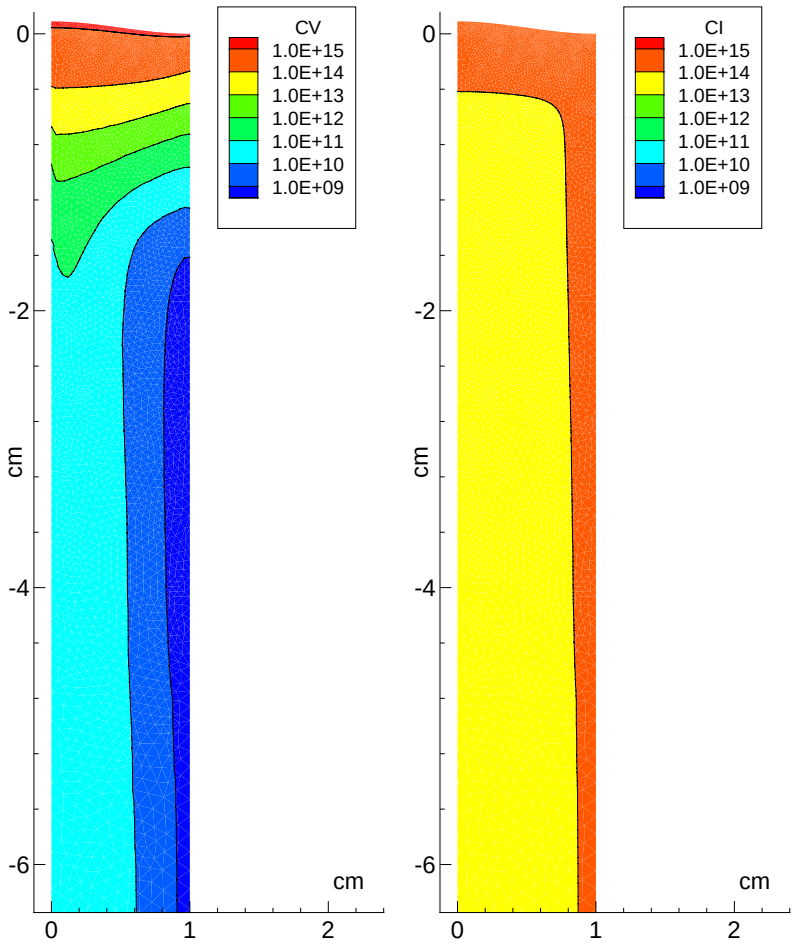

Figure 6.2. *Defect concentrations for the IKZ 0.8” configuration, using the recombination factor from Lemke (A.6). Concentrations in* $[\mathrm{cm}^{-3}]$.

substantially slower than for the Lemke recombination factor, as expected from figure A.1. The recombination procedure continues further down in temperature. The defects are for instance not immobilized at a distance of 4 cm corresponding to a temperature of approximately 950 K (figure 4.8, page 53).

The end result in the relatively cool crystal, at a distance of 10 cm from the phase boundary ($T = 680\,\mathrm{K}$), yields vacancy concentrations from $1.2 \cdot 10^{13}\,\mathrm{cm}^{-3}$ to $1.5 \cdot 10^{12}\,\mathrm{cm}^{-3}$ in radial direction and interstitial concentrations from $1.3 \cdot 10^{13}\,\mathrm{cm}^{-3}$ to $4.4 \cdot 10^{13}\,\mathrm{cm}^{-3}$. The result is therefore still interstitial domination throughout the crystal, but with comparable levels of vacancies in the center, as predicted by the Voronkov theory.

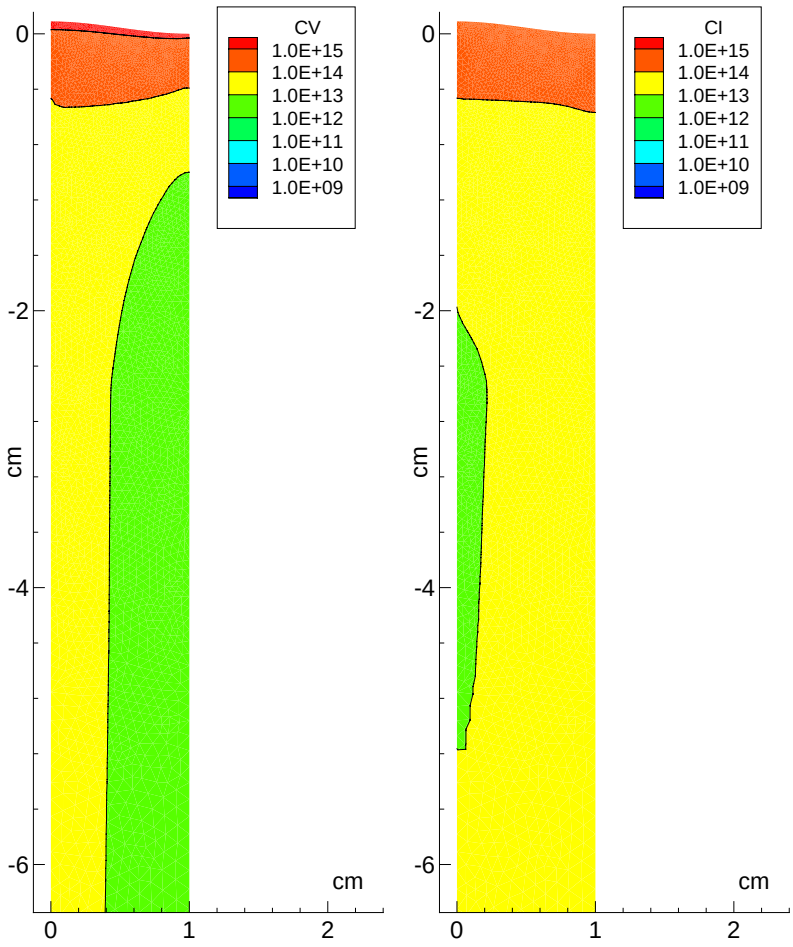

Figure 6.3. *Defect concentrations for the IKZ 0.8" configuration, using the recombination factor from Dornberger (A.5). Concentrations in* [cm^{-3}].

The good compliance with the Voronkov theory is not unexpected, since the Dornberger recombination factor, was fitted to measurements of the oxidation-induced stacking-fault or OSF ring in [78]. Note, however, that the Voronkov theory *does not* predict quantitative concentration levels, only the dominating defect type. The calculation in figure 6.3 does, however, support the assumption that the Voronkov theory is not restricted to crystals grown by the Czochralski technique, but that it is indeed applicable to at least small diameter float zone crystals.

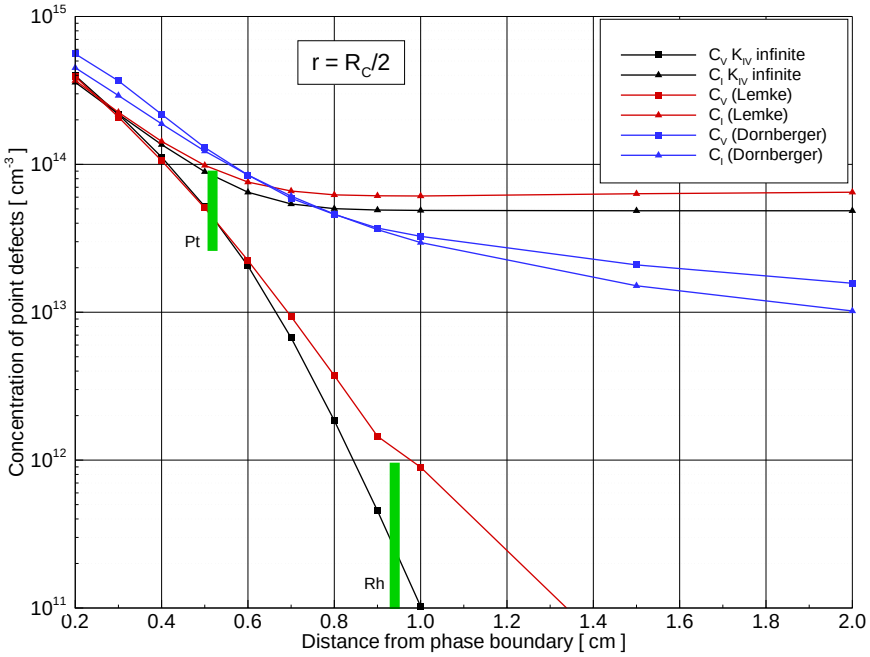

Figure 6.4. *Comparison of calculations and DLTS measurements for the IKZ 0.8” configuration, reproduced with the courtesy of H. Lemke. Concentrations of vacancies C_V and interstitials C_I at $r = R_{crystal}/2$. The green zone represents the concentrations of vacancies at the capture temperatures of Pt and Rh, given with the uncertainty of the capture temperatures and the DLTS measurements. The k_{IV} infinite are taken from [40] and the Lemke and Dornberger concentrations from figures 6.2 and 6.3 respectively.*

6.2.1 Comparison with DLTS measurement

Concentrations of point defects are not easy to obtain experimentally, however, one way to get a hint is through DLTS (Deep Level Transient Spectroscopy). DLTS measurements of two crystals grown with the IKZ 0.8” configuration were conducted in [40]. The crystals were doped with transition metals, one with Rhodium and one with Platinum. Transition metals are captured in the vacancy defects at temperatures characteristic for each metal, the capture temperatures. The concentration of vacancies at the capture temperature of rhodium can therefore be estimated by measuring the concentration of substitutional rhodium in the cold crystal. With a known temperature field, a given temperature can be translated to an axial position in the crystal. With two crystals, one doped with rhodium and one with platinum, the DLTS measurements, gives the vacancy concentration at two different positions in the crystal.

The concentrations of vacancies and interstitials as functions of axial distance (z) from the lower phase boundary, at $r = R_{crystal}/2$, are shown in figure 6.4. The figure includes calculations with the two different recombination factors of Lemke and Dornberger from figures 6.2 and 6.3, as well as an analytic calculation from [40] assuming infinite recombination. The DLTS measurements were added in green, with a span of approximately an order of magnitude, estimating the experimental uncertainty.

The recombination process within the first 1 cm of the crystal is from the experiments seen to be very fast, in fact the best match to the experiments is from the analytical calculation assuming infinite recombination. The Lemke recombination factor is a correlation from these experiments and is therefore seen to be in good accordance with the measurements. The recombination factor from Dornberger is, however, too low in the high-temperature area of the first 2 cm of the crystal ($1685\,\mathrm{K} < T < 1200\,\mathrm{K}$, see figure A.1, page 108). The span of about two orders of magnitude between the calculation with the Dornberger k_{IV} and the experiment, cannot be explained by an experimental uncertainty, but can only be attributed to, too low recombination at high temperature.

In summary, the concentration of point defects can be calculated using the proposed model. However, there are large differences in the physical parameters that need to be clarified, if the calculation should be used quantitatively. This is indeed the severe obstacle in the investigation of point defects, because the experimental results needed for correlation are difficult to obtain. The simulations include two different recombination factors, that have been correlated from two different experiments. The Lemke recombination factor matches the DLTS measurements, but produces distinct interstitial dominance in the center, which is in disagreement with the Voronkov theory. The recombination factor from Dornberger on the other hand, produces a concentration field in the cold crystal, that corresponds to what can be predicted from the Voronkov theory, however, the simulation has too high vacancy concentrations in the first part of the crystal, where the vacancy concentrations were determined using DLTS.

6.3 Thick crystal - 4”

The two 4” configurations are grown at pull speeds comparable to the thin crystal, so the difference is the smaller temperature gradients, due to the smaller surface to volume ratio.

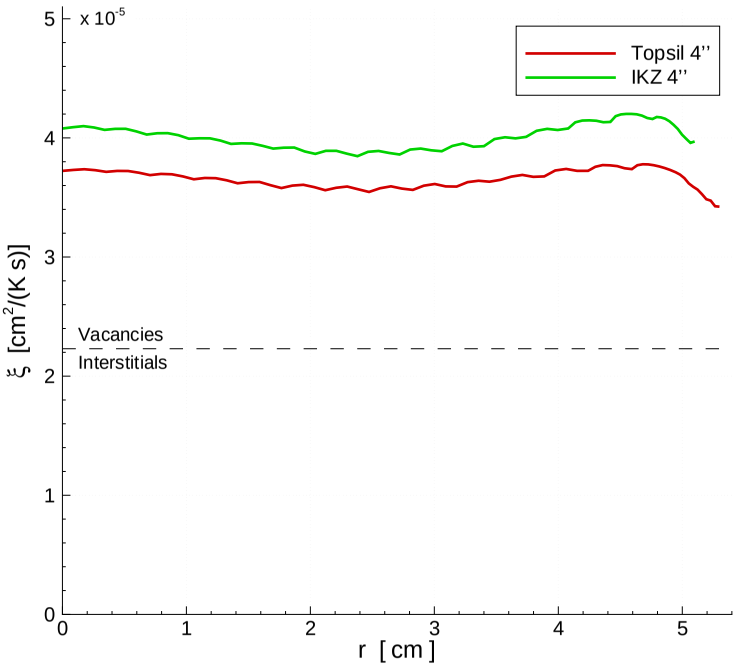

Figure 6.5. *The growth parameter ξ for the IKZ 4” and Topsil 4” configurations, grown at pull speeds of* 3.4 mm/min *and* 3.2 mm/min *respectively.* $\xi_{crit} = 2.23 \cdot 10^{-5} cm^2/K \cdot s$ *taken from [16].*

This results in higher values of the growth parameter and therefore crystals that are more prone to vacancy domination. The growth parameter both 4” configurations are clearly in the vacancy region, as seen in figure 6.5, so a vacancy domination throughout the crystal is expected regardless of the choice of recombination factor.

As for the thin crystal, calculations for the 4” crystals have been conducted with the recombination factors of both, Lemke and Dornberger. The results still differ, but since the considered crystals have both been grown in the vacancy regime, the difference is mainly the level of depletion of the interstitial defects. The crystal length in both, the IKZ 4” and the Topsil 4” configuration have been extended to 90 cm to avoid any effects from the end of the crystal. The no-flux condition at the end, interferes with the defect transport, hence the crystal was made longer. The longer crystal does have some effect on the cooling, as shown in chapter 4, but compared with the longest version of the two configurations (IKZ 4”-15rpm and Topsil 4”-3.3bar), the change should be minimal.

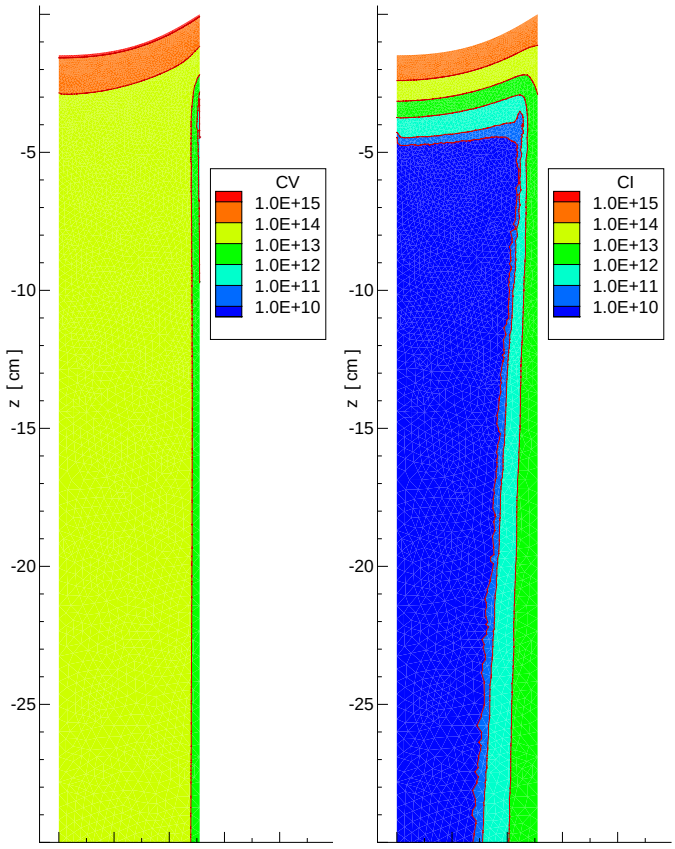

Figure 6.6. *Defect concentration for the IKZ 4" configuration, using the recombination factor from Lemke (A.6). Concentrations in* $[\mathrm{cm}^{-3}]$.

Figure 6.6 shows the calculated defect distribution for the IKZ 4" configuration using the recombination factor from Lemke. The result is vacancy domination throughout the crystal, except for a region of about 0.2 mm at the crystal rim, where the concentration of interstitials exceeds the concentration of vacancies. This outer region with interstitial domination, is probably numerically caused, because very large changes in the concentrations of both species exist just inside the crystal surface at $z = -4$, in an area where the recombination is strong. The level of vacancy concentration is from $5 \cdot 10^{13}\,\mathrm{cm}^{-3}$ in the center to $2 \cdot 10^{12}\,\mathrm{cm}^{-3}$ at the surface, whereas the interstitials range from being completely depleted in the center to $3 \cdot 10^{12}\,\mathrm{cm}^{-3}$ at the surface of the crystal.

The distribution of defects for the IKZ 4" configuration, using the Dornberger recombination factor, is shown in figure 6.7. As expected from the lower value of the recombination factor,

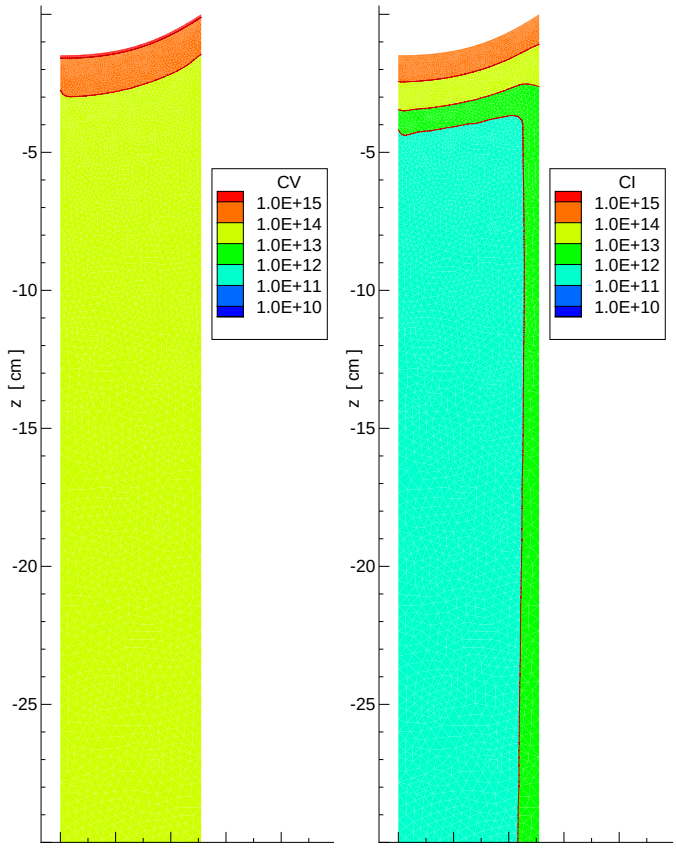

Figure 6.7. *Defect concentration for the IKZ 4” configuration, using the recombination factor from Dornberger (A.5). Concentrations in* [cm^{-3}].

the depletion of the interstitials is not as complete, as when using the Lemke recombination factor. The presumed numerical problem at the rim is absent, probably because of the reduced recombination. The concentrations of vacancies range from $3 \cdot 10^{13}\,\mathrm{cm}^{-3}$ in the center to $1 \cdot 10^{13}\,\mathrm{cm}^{-3}$ at the surface. Interstitial concentrations are $5 \cdot 10^{11}\,\mathrm{cm}^{-3}$ in the center to $1 \cdot 10^{12}\,\mathrm{cm}^{-3}$ at the surface. So as with the Lemke recombination factor the solution matches the prediction from the Voronkov theory, see figure 6.5.

The Topsil 4” is grown slightly slower then the IKZ 4”, and the value of the growth parameter in figure 6.5 is therefore lower, but still in the vacancy region. The simulation of the Topsil 4” configuration using the Lemke recombination factor is shown in figure 6.8. The same presumed numerical problem is seen in the vicinity of the crystal surface, where the vacancy concentration drops below the interstitial concentration. It can be observed that

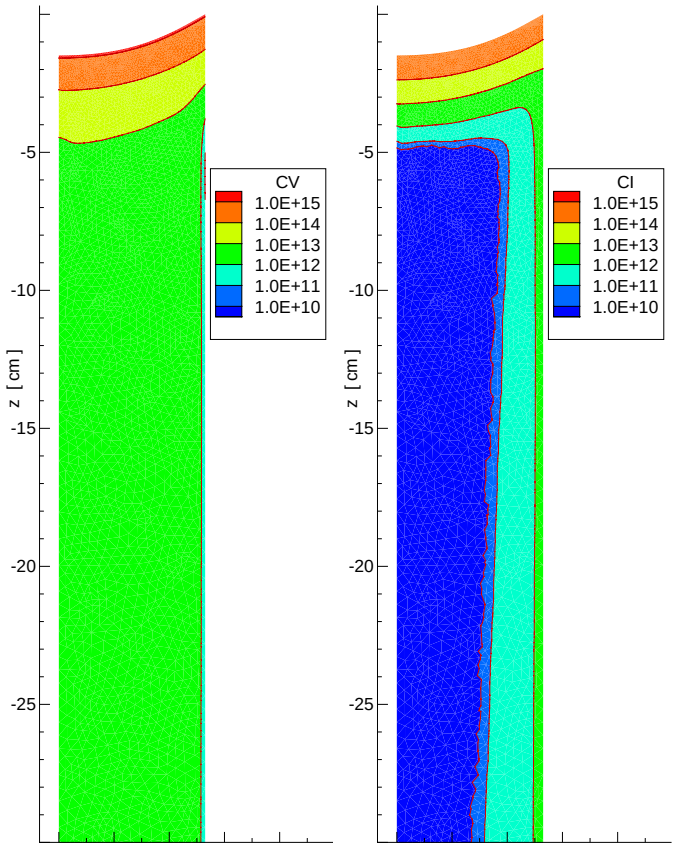

Figure 6.8. *Defect concentration for the Topsil 4" configuration, using the recombination factor from Lemke (A.6). Concentrations in* $[\mathrm{cm}^{-3}]$.

the crystal is still vacancy dominated, but since the growth parameter is lower, the mutual neutralization of the two species is better. Note that the Topsil 4" is not completely comparable to the IKZ 4", but the result that the concentrations of both species should be lower due to the lower growth parameter, is in accordance with the Voronkov theory. Vacancy concentrations in figure 6.8 are at levels of $7 \cdot 10^{12}\,\mathrm{cm}^{-3}$ in the center and $5 \cdot 10^{11}\,\mathrm{cm}^{-3}$ at the surface. Interstitials are completely depleted in the center and $1 \cdot 10^{12}\,\mathrm{cm}^{-3}$ at the surface.

Finally, figure 6.9 shows the defect distribution for the Topsil 4" configuration, using the recombination factor from Dornberger. The vacancy concentrations are here $5 \cdot 10^{13}\,\mathrm{cm}^{-3}$ in the center and $1 \cdot 10^{13}\,\mathrm{cm}^{-3}$ at the surface. Interstitials are at $1 \cdot 10^{10}\,\mathrm{cm}^{-3}$ in the center and $1 \cdot 10^{12}\,\mathrm{cm}^{-3}$ at the surface. That the IKZ 4" and Topsil 4" configurations are not completely comparable, can for the Dornberger recombination factor be seen by the fact

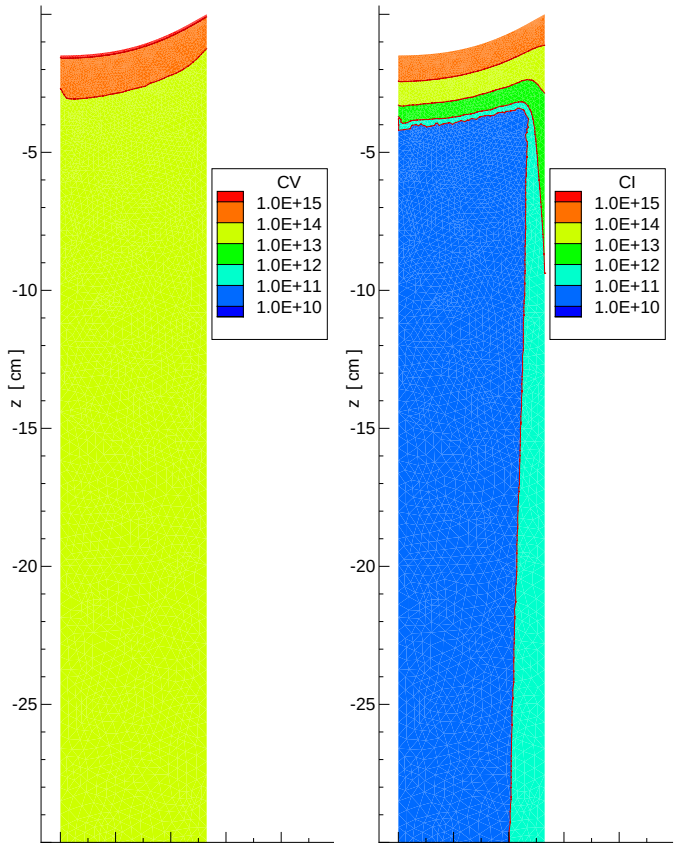

Figure 6.9. *Defect concentration for the Topsil 4” configuration, using the recombination factor from Dornberger (A.5). Concentrations in* [cm^{-3}].

that the concentration of vacancies is slightly higher in the center of the Topsil crystal than in the center of the IKZ crystal, contradicting the lower growth parameter.

In summary, it can be seen that the high growth parameters of both the IKZ 4” and the Topsil 4” processes produce vacancy dominated crystals. The concentration of vacancies is in the order of $10^{13}\,\mathrm{cm}^{-3}$ and the concentration of interstitials is below $10^{12}\,\mathrm{cm}^{-3}$, for both configurations and both recombination factors. Generally the concentrations of vacancies are declining outwards, whereas concentrations of interstitials increase for larger radius. For the high values of the growth parameter encountered in the 4” configurations, the recombination factor is not as crucial, as for the cases with the growth parameter near the critical value. The difference is mainly in the level of depletion.

Chapter 7

Conclusion

The purpose of this Ph.D project was to develop a global simulation of the needle-eye float zone process for growing silicon single crystals. This goal has been achieved by combining commercially available software for the heat transfer and melt convection, with software developed within this project for transport of dopant and defects. The main conclusions of the work will be outlined here, grouped as they were in the different chapters of the thesis and completed by a look at the future aspects of the project.

Conduction solution

Free surface shapes have been determined for two different 4" configurations (IKZ 4" and Topsil 4"), as well as the thin IKZ 0.8" configuration, by solving the coupled electromagnetic and free surface models. The induced electric surface current, determined by these models, were used as input for the heat transfer calculations. The solution to the heat transfer is the global temperature field, along with the shape of the two phase boundaries. The shape of the lower phase boundary has been measured using the LPS technique at the IKZ, and was compared with the calculated shapes. From the good agreement between the measured and calculated phase boundaries, it can be concluded that the conduction solution includes the relevant physics, and that the influence on the shape of the lower phase boundary from melt convection is negligible. It was additionally seen, that the surface area is the limiting factor

in the cooling of the crystal, and a larger surface to volume ratio gives a faster cooling, and hence increased temperature gradients.

A study of the convective cooling of the crystal, caused by natural convection in the pressurized surrounding argon atmosphere, has been conducted. The result is that the increased pressure implies additional cooling, which influences the depth of the lower phase boundary. The simulations were accompanied by LPS measurements, comparing the changes in the depth of the lower phase boundary, for a crystal the grown at 1.9 and 3.3 bar absolute pressure. The influence from the pressure change is small, i.e. little change in phase boundary depth. The influence from increased pressure in the calculation, is the same as in the measurements, indicating the physical effect has been modelled correctly.

Melt convection and dopant transport

The simulations of melt convection includes centrifugal, buoyancy, thermocapillary and electromagnetic driving forces, which have all been simulated alone to show their individual impact on the complex flow field. Unsteady convection calculations have been conducted for both of the 4" configurations in four different setups, one for the Topsil 4" and three, with different rates of rotation, for the IKZ 4" configuration. The general flow pattern is two counter rotating vortices, with a stagnation area in between. The flow is laminar, but unsteady. The unsteadiness is seen be to damped by increasing rotation, so that the flow at 15 rpm crystal rotation is virtually steady state.

In the dopant transport the unsteady velocity field of the melt was taken as input and gas doping was simulated by prescribing a flux of dopant through the free surface. The result are dopant concentration fields, with instabilities in the same areas where the flow fields oscillates, and with distinct concentration boundary layers caused by segregation. The thickness of the concentration boundary layer and thereby the concentration buildup at the lower phase boundary, was seen to be controlled by the momentum boundary layer. Local concentration peaks, at the lower phase boundary, were therefore located at stagnation points and enhanced by convective transport into the free stream at separation points.

The concentration at the lower phase boundary was used to calculate radial resistivity profiles, for comparison with measurements. The agreement is fair, exhibiting the same

characteristic properties as the measurements. The calculated resistivity profiles have more local maxima and minima then the measurements, which is presumably caused by non-rotational symmetric instabilities in the real process, stirring the concentration boundary layer.

Defects

The transport of point defects of vacancy and interstitial type, have been simulated using two transport equations coupled by the recombination of the two defect types to neutralize each other. Simulations using the thin IKZ 0.8" configuration, with a growth parameter in the critical region, was conducted for two different recombination factors and compared to DLTS measurements. One of the recombination factors have been correlated from the position of the OSF ring in a Czochralski experiment, whereas the other one have been correlated from DLTS measurements on this crystal. The investigation is inconclusive as to which of the recombination factors are the better, since they each matched the experiment they have been correlated to, but not the other.

Both recombination factors were applied in the simulation of defect transport for both of the 4" configurations. Because of the slower cooling of the larger crystals, the growth parameter was in the vacancy region and the difference in the recombination factor, therefore only influenced the level of depletion of the interstitials. Numerical simulation of defect transport is a relative new and increasingly interesting area for float zone crystals, but the accuracy of the physical parameters and the difficulty of experiments are still obstacles for the study of defects.

Future aspects

From a commercial point of view, a tool has been developed, where the geometrical and process data can be used to calculate temperature fields and gradients, growth parameter values, flow fields and resistivity profiles. The tool can be used as it is, but features as external forces varying in time, e.g. magnetic fields, would be desirable. From an academic point of view implementing external forces is not a formidable task, it involves some changes to the MHAC code, but it has no novelty.

In the simulation of defects, the surface has only been scratched, it is a new field for the float zone process and here are opportunities of academic contributions. Of interest would be, to expand the simulations to larger crystals, to investigate how reduced temperature gradients, due to the smaller surface to volume ratio, affects the incorporation of defects. It is expected that larger diameter processes will have higher growth parameters, and means to repress the presumed large vacancy domination, would therefore be an interesting study. In defect studies, there is also an experimental task as well as an numerical, to provide experimental data, that the simulations can be compared to, and to create a more solid foundation for the physical parameters used in the simulations.

Bibliography

[1] T. Abe, H. Harada, and J. Chikawa. Swirl defects in float-zoned silicon crystals. *Physica B*, 116:139–147, 1983.

[2] AEA Technology, B552 Harwell, Oxfordshire, England, OX11 ORA. *Harwell Subroutine Library - MA41*, 1995.

[3] G. E. Anner. *Planar processing primer.* Van Nordstrand Reinhold, 1. edition, 1990.

[4] R. Assaker. *Magnetohydrodynamics in Crystal Growth.* PhD thesis, Faculté des Sciences Appliquées, Départment de Machanique, Université catholique de Louvain, Belgium, 1998.

[5] O. Axelsson and V. A. Barker. *Finite element solution of boundary value problems.* Academic Press, 1. edition, 1984.

[6] V. A. Barker and J. Reffstrup. The finite element method for partial differential equations. Unpublished notes from Department of Mathematical Modelling, Technichal University of Denmark, 1998.

[7] W. Blanke, editor. *Thermophysikalische Stoffgrössen.* Springer Verlag, 1989. In German.

[8] R. A. Brown, D. Maroudas, and T. Sinno. Modelling point defect dynamics in the crystal growth of silicon. *Journal of Crystal Growth*, 137:12–25, 1994.

[9] J. A. Burton, R. C. Prim, and W. P. Slichter. The distribution of solute in crystals grown from the melt. *Journal of Chemical Physics*, 21:1987, 1953.

[10] Cape Simulations Inc., One Bridge Street, Newton, MA 02158, USA. *FZ - Sim, A finite element simulator for float zone growth of Si*, 1995. `www.capesim.com`.

[11] Cape Simulations Inc., One Bridge Street, Newton, MA 02158, USA. *MHACPRE ver. 2.1*, 1999. `www.capesim.com`.

[12] C. E. Chang and R. Wilcox. Inhomogeneities due to thermocapillary flow in floating zone melting. *International Journal of Heat and Mass Transfer*, 28:8–12, 1975.

[13] C. E. Chang and R. Wilcox. Analysis of surface tension driven flow in floating zone melting. *International Journal of Heat and Mass Transfer*, 19:355–366, 1976.

[14] S. R. Coriell and M. R. Cordes. Theory of molten zone shape and stability. *Journal of Crystal Growth*, 42:466–472, 1977.

[15] A. Cröll, P. Dold, Th. Kaiser, F. R. Szofran, and K. W. Benz. The influence of static and rotating magnetic fields on heat and mass transfer in silicon floating zones. *Journal of Electrochemical Society*, 146(6):2270–2275, 1999.

[16] E. Dornberger, T. Sinno, J. Esfandyari, J. Vanhellemont, R. A. Brown, and W. von Ammon. Determination of intrinsic point defect properties on silicon by analyzing OSF ring dynamics and void formation. In C. L. Claeys, P. Rai-Choudhury, M. Watanabe, P. Stallhofer, and H. J. Dawson, editors, *High Purity Silicon V*, volume 98-13, pages 170–187. The Electrochemical Society Inc., 1998.

[17] E. Dornberger and W. von Ammon. The dependence of ring-like distributed stacking faults on the axial temperature gradient of growing Czochralski silicon crystals. *Journal of Electrochemical Society*, 143(5):1648–1653, 1996.

[18] I. S. Duff, A. M. Erisman, and J. K. Reid. *Direct methods for sparse matrices*. Oxford science publications, 1986.

[19] T. Ebe. Factors determining te saturation of point defects in growing silicon crystals. *Journal of Crystal Growth*, 203:387–399, 1999.

[20] E. R. G. Eckert and R. M Drake Jr. *Heat and Mass Transfer*. McGraw Hill, 2 edition, 1959.

[21] K. Ericksson, D. Estep, P. Hansbo, and C. Johnson. *Computational differential equations*. Cambridge university press, 1. edition, 1996.

[22] P. M. Fahey, P. B. Griffin, and J. D. Plummer. Point defects and dopant diffusion in silicon. *Reviews of modern physics*, 61(2):289–384, 1989.

[23] R. Habu, T. Iwasaki, H. Harada, and A. Tomiura. Diffusion behavior of point defects in Si crystal during melt growth IV: Numerical analysis. *Japan journal of applied physics*, 33:1234–1242, 1994.

[24] J. C. Heinrich, P. S. Huyakorn, O. C. Zienkiewicz, and A. R. Mitchel. An 'upwind' finite element scheme for two-dimensional convective transport equation. *International Journal for Numerical Methods in Engineering*, 11:131–143, 1977.

[25] D. T. J. Hurle, editor. *Bulk crystal growth*, volume 2A of *Handbook of crystal growth*, chapter 4, pages 213–259. North-Holland, 1994.

[26] P. S. Huyakorn and K. Nilkuha. Solution of transient transport equation using an upstream finite element scheme. *Applied Mathematical Modelling*, 5:7–17, 1979.

[27] F. P. Incropera and D. P. De Witt. *Introduction to heat transfer*. Wiley, 1. edition, 1990.

[28] T. Izumi. Model analysis of segregation phenomena for silicon crystal growth from the melt. *Journal of Crystal Growth*, 181:210–217, 1997.

[29] C. Johnson. *Numerical solution of partial differential equations by the finite element method*. Studentlitteratur, 1. edition, 1987.

[30] W. Keller and A. Mühlbauer. *Float-zone silicon*. Marcel Dekker, 1981. vol. 5 in Preparation and properties of solid state materials.

[31] E. N. Kolesnikova, Yu. A. Polokov, V. S. Yuferev, and A. I. Zhmakin. Influence of coriolis force on thermal convection and impurity segregation during crystal growth under microgravity. *Journal of Crystal Growth*, 180:578–586, 1997.

[32] Zh. Kozhoukhaova and S. Slavchev. Computer simulation of the thermocapillary convection in a non-cylindrical floating zone. *Journal of Crystal Growth*, 74:236–246, 1986.

[33] Scientific division L'Air Liquid. *Gas Encyclopaedia.* Elsevier, 1976.

[34] C. W. Lan. Newtons's method for solving heat transfer, fluid flow and interface shapes in a floating molten zone. *International Journal for Numerical Methods in fluids*, 19:41–65, 1994.

[35] C. W. Lan. Effects of axisymmetric magnetic fields on radial dopant segregation of floating-zone silicon growth in a mirror furnace. *Journal of Crystal Growth*, 169:269–278, 1996.

[36] C. W. Lan and S. Kou. Thermocapillary flow and melt / solid interfaces in floating-zone crystal growth under microgravity. *Journal of Crystal Growth*, 102:1043–1058, 1990.

[37] C. W. Lan and M. C. Liang. Modulation dopant segregation in floating-zone silicon growth in magnetic fields using rotation. *Journal of Crystal Growth*, 180:381–387, 1997.

[38] T. L. Larsen, L. Jensen, and M. P Sørensen. Simulation of float-zone silicon single crystal growth. In L. Arkeryd, J. Bergh, P. Brenner, and R. Pettersson, editors, *Progress in Industrial Mathematics at ECMI 98*, pages 70–77. B. G. Teubner, 1999.

[39] T. L. Larsen, A. Lüdge, H. Riemann, L. Jensen, A. Nielsen, and M. P Sørensen. Convective cooling of floating zone silicon crystal during growth. In *Proceedings of the International Colloquium, Modelling of Material Processing*, pages 18–23, 1999.

[40] H. Lemke and W. Südkamp. Analytic approximations for the distributions of intrinsic point defects in grown silicon crystals. *Physica status solidi - A - Applied research*, 176(2):843–866, 1999.

[41] H. Lemke and W. Zulehner. Impact of vacancies and self-interstitials on the formation of substitutional transition metal defects in float-zone silicon crystals. *Physica B condensed matter*, 273-274:398–403, 1999.

[42] M. Levenstam. *Thermocapillary Convection in Floatzones.* PhD thesis, Royal Institute of Technology, Department of Mechanics, Stockholm, 1994.

[43] M. Levenstam and G. Amberg. Hydrodynamical instabilities of thermocapillary flow in a half-zone. *Journal of Fluid Mechanics*, 297:357–372, 1995.

[44] M. Levenstam, G. Amberg, T. Carlberg, and M. Andersson. Experimental and numerical studies of thermocapillary convection in a floating zone like configuration. *Journal of Crystal Growth*, 158:224–230, 1996.

[45] K. H. Lie, J. S. Walker, and D. N. Riahi. Free surface shape and AC electric current distribution for float zone silicon growth with a radio frequency induction coil. *Journal of Crystal Growth*, 100:450–458, 1990.

[46] A. Lüdge, H. Riemann, W. Schröder, A. Mühlbauer, A. Muiznieks, and G. Raming. Experimental confirmation of a numerical model of doping distribution for floating-zone silicon growth with the needle eye technique. In 8^{TH} *International symposium on silicon materials science and technology*, volume 98, San Diego, May 3-8 1998.

[47] D. Maroudas and R. A. Brown. Atomistic calculation of the self-interstitial diffusivity in silicon. *Applied Physics letters*, 62(2):172–174, 1993.

[48] D. Maroudas and R. A. Brown. Calculation of thermodynamic and transport properties of intrinsic point defects in silicon. *Physical review B*, 47(23):562–577, 1993.

[49] M. Meyyappan, editor. *Computational modeling in semiconductor processing.* Artech House, 1. edition, 1995.

[50] T. E. Morthland and J. S. Walker. Thermocapillary convection during floating-zone silicon growth with a uniform or non-uniform magnetic field. *Journal of Crystal Growth*, 158:471–479, 1996.

[51] T. E. Morthland and J. S. Walker. Convective heat transfer due to thermocapillary convection with a strong magnetic field parallel to the free surface. *International Journal of Heat and Mass Transfer*, 40(14):3283–3291, 1997.

[52] A. Mühlbauer, W. Erdmann, and W. Keller. Electrodynamic convection in silicon floating zones. *Journal of Crystal Growth*, 64:529–545, 1983.

[53] A. Mühlbauer, A. Muiznieks, A. Jakowitsch, and J. Virbulis. Berechnung des dreidimensionalen Hochfrequenzfeldes beim Zonenschmelzen von Silicium. *Archiv für Elektrotechnik*, 76:161–168, 1993. In German.

[54] A. Mühlbauer, A. Muiznieks, and H. J. Lessmann. The calculation of 3D high-frequency electromagnetic fields during induction heating using the BEM. *IEEE transactions on magnetics*, 29(2):1566–1569, 1993.

[55] A. Mühlbauer, A. Muiznieks, and G. Raming. System of mathematical models for the analysis of industrial FZ-Si-crystal growth processes. *Crystal Research Technology*, 34(2):217–226, 1999.

[56] A. Mühlbauer, A. Muiznieks, G. Raming, H. Riemann, and A. Lüdge. Numerical modelling of the microscopic inhomogeneities during FZ silicon growth. *Journal of Crystal Growth*, 198/199:107–113, 1999.

[57] A. Mühlbauer, A. Muiznieks, and J. Virbulis. Analysis of the dopant segregation effects at the floating zone growth of large silicon crystals. *Journal of Crystal Growth*, 180:372–380, 1997.

[58] A. Mühlbauer, A. Muiznieks, J. Virbulis, A. Lüdge, and H. Riemann. Interface shape, heat transfer and fluid flow in the floating zone growth of large silicon crystals with the needle-eye technique. *Journal of Crystal Growth*, 151:66–79, 1995.

[59] G. Müller. *Crystals grown from the melt / 12 Crystal growth, properties and application.* Springer-Verlag, 1. edition, 1988.

[60] J. Patankar. *Numerical Heat Transfer and Fluid Flow.* Hemisphere Publishing Company, 1980.

[61] R. Peyret and T. D. Taylor. *Computational methods for fluid flow.* Springer-Verlag, 1. edition, 1983.

[62] L. Råde and B. Westergren. *Beta - Mathematics handbook.* Studentlitteratur, 2. edition, 1990.

[63] C. V. Ramakrishnan. An upwind finite element scheme for the unsteady convective diffusive transport equation. *Applied Mathematical Modelling*, 3:280–284, 1979.

[64] G. Raming, A. Muiznieks, and A. Mühlbauer. Numerical modelling of the influence of different types of magnetic fields on fluid motion and resistivity profiles during FZ-silicon growth. In *Proceedings of the International Colloquium, Modelling of Material Processing*, pages 24–29, 1999.

[65] M. M. Rao and W. Shyy. Moving boundary computation of the float-zone process. *International Journal for Numerical Methods in Engineering*, 40:1231–1261, 1997.

[66] G. Ratnieks, A. Muiznieks, L. Buligins, G. Raming, A. Mühlbauer, A. Lüdge, and H. Riemann. Influence of three-dimensionality of the HF electromagnetic field on resistivity variations in si single crystal during FZ-growth. *Journal of Crystal Growth*. To be published.

[67] G. Ratnieks, A. Muiznieks, G. Raming, A. Mühlbauer, and L. Buligins. 3D modelling of magnetic, temperature, hydrodynamic and dopant concentration fields during FZ silicon crystal growth. In *Proceedings of the International Colloquium, Modelling of Material Processing*, pages 30–35, 1999.

[68] J. N. Reddy. *An introduction to the finite element method*. McGraw-Hill, 2. edition, 1993.

[69] D. N. Riahi and J. S. Walker. Float zone shape and stability with the electromagnetic body force due to a radio-frequency induction coil. *Journal of Crystal Growth*, 94:635–642, 1989.

[70] J. G. Rice and R. J. Schnipke. A monotone streamline upwind finite element method for convection-dominated flows. *Computer methods in applied mechanics and engineering*, 48:313–327, 1985.

[71] H. Riemann and A. Lüdge. Intrinsic defects in FZ silicon and their impact on z-ray pin sensor parameters. In *High Purity Silicon VI*. The Electrochemical Society Inc. To be published.

[72] H. Riemann, A. Lüdge, K. Böttcher, H. Rost, B. Hallmann, W. Schröder, W. Hensel, and B. Schleusener. Silicon floating zone process: Numerical modelling of RF field, heat transfer, thermal stress and experimental proof for 4" crystal. *Journal of Electrochemical Society*, 142(3):1007–1014, 1995.

[73] H. Sasaki, K. Terashima, E. Tokizaki, and S. Kimura. Density variation of molten silicon and influence on crystal perfection. In *Semiconductor silion, seventh international symposium on silicon materials science and technology*. Electrochemical Society, 1994.

[74] T. W. H. Sheu, S. F. Tsai, and M. M. T. Wang. A monotone multidimensional upwind finite element method for advection-diffusion problems. *Numerical heat transfer, Part B*, 29:325–344, 1996.

[75] W. Shyy and M. M. Rao. Calculation of meniscus shapes and transport processes in float zone. *International Journal of Heat and Mass Transfer*, 38(12):2281–2295, 1995.

[76] W. Shyy, H. S. Udaykumar, M. M. Rao, and R. W. Smith. *Computational fluid dynamics with moving boundaries.* Taylor & Francis, 1. edition, 1996.

[77] T. Sinno, R. A. Brown, W. von Ammon, and E. Dornberger. On the dynamics of the oxidation-induced stacking-fault ring in as-grown Czochralski silicon crystals. *Applied physics letters*, 70(17):2250–2252, 1997.

[78] T. Sinno, R. A. Brown, W. von Ammon, and E. Dornberger. Point defect dynamics and the oxidation-induced stacking-fault ring in Czochralski-grown silicon crystals. *Journal of Electrochemical Society*, 145(1):302–318, 1998.

[79] T. Sinno, Z. K. Jiang, and R. A. Brown. Atomistic simulation of point defects in silicon at high temperature. *Applied Physics letters*, 68(21):3028–3030, 1996.

[80] W. R. Smythe. *Static and dynamic electricity.* McGraw-Hill, 3. edition, 1968.

[81] T. Surek and S. R. Coriell. Shape stability in float zoning of silicon crystals. *Journal of Crystal Growth*, 37:253–271, 1977.

[82] E. Takasuka, E. Tokizaki, K. Terashima, and S. Kimura. Emissivity of liquid silicon in visible and infrared regions. *Journal of Applied Physics*, 81(9):6384–6389, 1997.

[83] T. Y. Tan and U. Gösele. Point defects, diffusion processes and swirl defect formation in silicon. *Applied Physics A*, 37:1–17, 1985.

[84] S. Togawa, Y. Nishi, and M. Kobayashi. Estimation of radial resistivity profile of FZ Si crystals by numerical simulation. *Electrochemical Society Proceedings*, 98-13:67–78, 1998.

[85] J. Virbulis. *Numerische Simulation der Phasengrenzen und Schmelzenströmung bei der Züchtung von Siliziumkristallen mit dem Floating-Zone Verfahren.* PhD thesis, Fakultät für Physik und Mathematik, University of Latvia, Latvia, 1994. In German.

[86] V. V. Voronkov. The mechanism of swirl defects formation in silicon. *Journal of Crystal Growth*, 59:625–643, 1982.

[87] F. M. White. *Viscous fluid flow.* McGraw-Hill, 1. edition, 1991.

[88] L. O. Wilson. A new look at the Burton, Prim, and Slichter model of segregation during crystal growth from the melt. *Journal of Crystal Growth*, 44:371–378, 1978.

[89] G. W. Young and A. Chait. Surface tension driven heat, mass and momentum transport in a two-dimensional float-zone. *Journal of Crystal Growth*, 106:445–466, 1990.

Appendix A

Physical properties

Physical properties of silicon

Variable		Value		Unit	Ref
β	*compressibility*	$1.5 \cdot 10^{-4}$		K^{-1}	[85]
ϵ	*emissivity (s)*	0.64	$(T < 1000K)$	-	[85]
		$0.9 - 2.6 \cdot 10^{-4} \cdot \mathrm{T}$	$(T > 1000K)$	-	[85]
	emissivity (l)	0.27		-	[82]
γ	*surface tension*	0.74		N/m	[85]
$\partial\gamma/\partial T$	*deriv. of surf. tension*	$-2.8 \cdot 10^{-4}$		$N/(m \cdot K)$	[85]
ℓ	*latent enthalpy*	$1.8 \cdot 10^{6}$		J/kg	[85]
λ	*heat conductivity (s)*	$98.9 - 0.0943 \cdot \mathrm{T}$	$+2.89 \cdot 10^{-5} \cdot \mathrm{T}^2$	$W/(m \cdot K)$	[85]
	heat conductivity (l)	67.0		$W/(m \cdot K)$	[85]
ν	*kinematic viscosity*	$3.4 \cdot 10^{-7}$		m^2/s	[85]
ρ	*density (s)*	$2.33 \cdot 10^{3}$		kg/m^3	[85]
	density (l)	$2.53 \cdot 10^{3}$		kg/m^3	[73]
σ	*electrical conductivity (s)*	$5 \cdot 10^{4}$		S/m	[85]
	electrical conductivity (l)	$1.2 \cdot 10^{6}$		S/m	[85]
c_p	*specific heat capacity*	$1 \cdot 10^{3}$		$J/(kg \cdot K)$	[85]
T_{melt}	*melting point temperature*	1685		K	[85]

The extensive use of [85] as reference for the physical parameters, is because the models within this work have been compared with numerical simulations by the group of Institute

for Electroheat led by prof. Mühlbauer and this reference represents their well documented set of parameters.

Properties of dopant transport

Variable		Value	Unit	Ref
D	*Diffusivity of P in Si*	$3.4 \cdot 10^{-8}$	m^2/s	[57]
g	*Gravitational acceleration*	9.80	m/s^2	-
k_0	*Segregation coefficient of P in Si*	0.35	kg/m^3	[3]

Properties of point defects in silicon

The diffusivities of vacancies D_V and self-interstitials D_I in solid silicon are according to [78] given by

$$D_V = 1.0 \cdot 10^{-3} \exp\left(-\frac{0.457}{kT}\right) \tag{A.1}$$

$$D_I = 0.242 \exp\left(-\frac{0.937}{kT}\right) \tag{A.2}$$

The unit of the diffusivities is $[\mathrm{cm}^2/\mathrm{s}]$. k is the Boltzman constant ($k = 8.617 \cdot 10^{-5}\ eV/K$). Equilibrium concentrations of point defects are only functions of temperature and given by [78].

$$C_V^{eq} = 4.97 \cdot 10^{22} \exp\left(-3.7 + 3.53 \cdot 10^{-3}\ T\right) \cdot \exp\left(-\frac{2.48 + 2.33 \cdot 10^{-4}\ T}{kT}\right) \tag{A.3}$$

$$C_I^{eq} = 2.97 \cdot 10^{23} \exp\left(1.40 + 3.85 \cdot 10^{-3}\ T\right) \cdot \exp\left(-\frac{3.46 + 3.08 \cdot 10^{-4}\ T}{kT}\right) \tag{A.4}$$

The unit of the equilibrium concentrations is $[\mathrm{cm}^{-3}]$. The values at melt point are: $C_V^{eq}(T_{melt}) = 1.22 \cdot 10^{15}\,\mathrm{cm}^{-3}$ and $C_I^{eq}(T_{melt}) = 9.92 \cdot 10^{14}\,\mathrm{cm}^{-3}$. Pure silicon consists of approximately $5 \cdot 10^{22}\,\mathrm{atoms/cm}^3$.

The recombination factor k_{IV} is also a pure function of temperature, but the correlations varies throughout the literature. This appendix includes four correlations from three different recent sources. Dornberger et. al [17], (A.5)

$$k_{IV} = 1.2 \cdot 10^{-6}(D_V + D_I) \cdot \exp\left(-\frac{0.61 + kT(-2.3 + 7.38 \cdot 10^{-3}\ T)}{kT}\right) \tag{A.5}$$

k_{IV} has the unit $[\mathrm{cm}^3/\mathrm{s}]$. From Lemke and Südkamp [40] comes an experimentally fitted correlation for k_{IV}, (A.6)

$$k_{IV} = \frac{20}{C_V^{eq}} \exp\left(-\frac{1.25}{kT_{melt}}\left(\frac{T_{melt}}{T} - 1\right)\right) \tag{A.6}$$

Finally the last two (A.7-A.8) from Ebe [19] states

$$k_{IV} = 4 \cdot 10^{-7}\pi(D_V + D_I)\exp(-11.5) \tag{A.7}$$

$$k_{IV} = 4 \cdot 10^{-7}\pi(D_V + D_I)\exp\left(-\frac{1.4}{kT}\right) \tag{A.8}$$

The different correlations are shown as functions of temperature from melt point down to $500K$ in figure A.1.

Penetration of electromagnetic field

The frequency-dependent penetration depth of the electromagnetic field into the silicon is very important to the practical process of growing the crystal. Figure A.2 shows the dependency of frequency given by equation (2.1) on page 10.

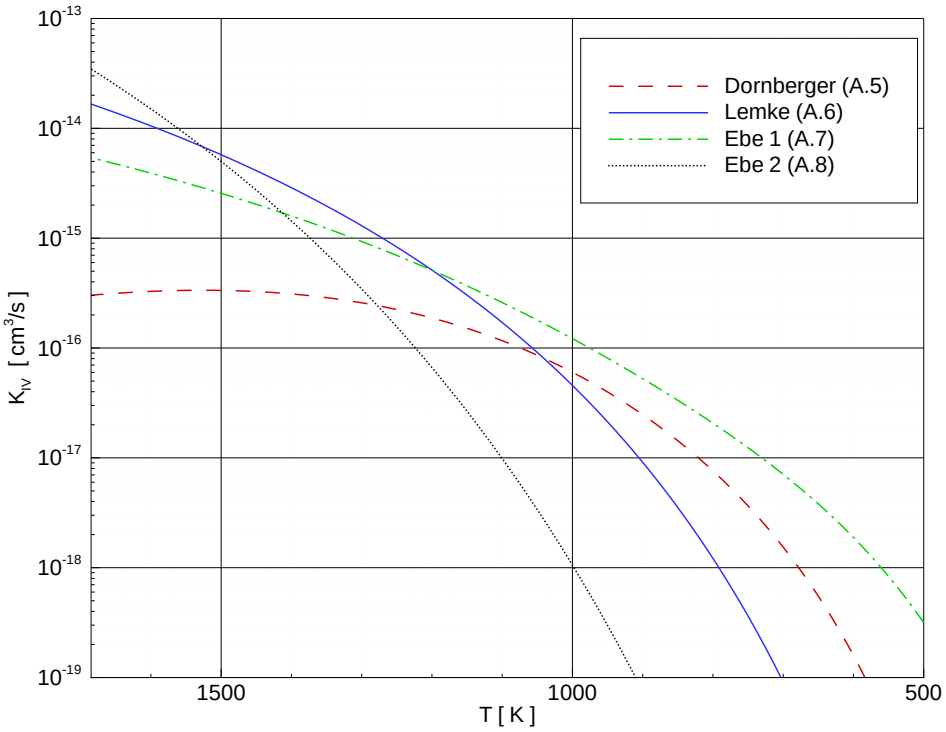

Figure A.1. *The recombination factor k_{IV} as given by (A.5-A.8).*

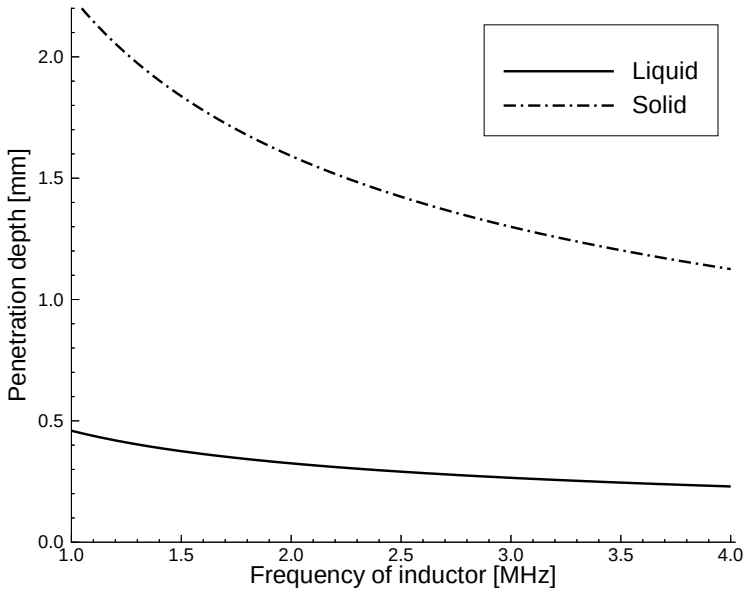

Figure A.2. *The penetration depth as function of frequency for silicon.*

Appendix B

Dimensional analysis

A dimensional analysis is given in this appendix to describe the order of magnitude of the individual forces involved in this physical context. A dimensional analysis for a 3" floating-zone configuration is given in [52] and an exhaustive list of relevant dimensionless groups can be found in [49].

If dimensional parameters are not directly specified in the context then the are to be found in appendix A. The dimensionless groups are calculated for the 4" IKZ configuration with respect to length scales ($R_{crystal} = 5\,\mathrm{cm}$) and velocities.

Free surface

On the free surface the parametric description (2.12c), see page 14, has a *Bond number* Bo, which is the ratio of gravitational to surface tension force, and an *Electromagnetic Bond number* Bo_ϵ which is the ratio of the normal electromagnetic force to the surface tension force [69].

$$Bo = \frac{g\Delta\rho R_{crystal}^2}{\gamma} \approx 84 \tag{B.1}$$

$$Bo_\epsilon = \frac{\mu_0 I_0^2}{4\gamma R_{crystal}} \approx 30 \tag{B.2}$$

Where $I_0 = 1870\,\mathrm{A}$ is the current in the inductor. By comparing the ratio of the two Bond numbers it is seen that the influence from gravitational forces is about 3 times as strong as

the influence from the normal electromagnetic force. A third Bond number, the *Rotational Bond number* [49], relating the rotational force to the surface tension force, is included to justify neglecting centrifugal forces from the calculation of the free surface shape. The calculation is for a 5 rpm rate of rotation.

$$Bo_\omega = \frac{\rho\omega^2 R_{crystal}^3}{2\gamma} \approx 1.5 \cdot 10^{-3} \tag{B.3}$$

Conduction within the crystal and molten zone

For the conduction in the solid silicon the *Peclét number* Pe is the ratio of convective and diffusive heat transfer. The convective heat transfer comes through a finite growth velocity, for the configuration investigated a velocity $V_{crystal} = 3.4mm/min$ is used. A temperature of $T = 1000K$ is used to calculate the specific heat conductivity λ[1].

$$Pe = \frac{V_{crystal} R_{crystal}}{\alpha} \approx 0.19 \tag{B.4}$$

$$\alpha = \frac{\lambda}{\rho c_p}$$

Besides the effect of convective heat transfer described by the Peclét number, the release and absorption of latent enthalpy is also dependent on the growth velocity, see (2.16) page 16, so overall the temperature field is strongly dependent on $V_{crystal}$. The *Prandtl number* Pr is the ratio of momentum and thermal diffusivity, describing the heat transfer within the molten zone.

$$Pr = \frac{\nu}{\alpha} \approx 0.013 \tag{B.5}$$

The low Prandtl number results in a weak dependence of the temperature field on the flow field. It is from experiments well established that the shape of the phase boundaries is virtually unchanged by flow conditions, hence this influence is neglected in the calculations.

Melt convection

An early part of this work [38] includes a dimensional analysis of the relative magnitude of the Marangoni and natural convections. This work is completed here by determining

[1] λ varies from 22 W/(m · K) at 1685 K to 60 W/(m · K) at 500 K, see appendix A.

the remaining dimensionless groups. For the four driving forces three dimensionless groups were found in the literature all relating the forces to the viscous momentum transfer. The *Grashof number Gr* describes buoyancy forces, the *Marangoni number* forces due to surface tension gradients and the *Rotational Reynolds number* Re_ω centrifugal forces, all as ratios to the viscous momentum transfer.

$$Gr = \frac{g\beta R_{crystal}^3 \Delta T}{\nu^2} \quad \approx \quad 4.8 \cdot 10^7 \tag{B.6}$$

$$Ma = \frac{(\partial\gamma/\partial T) R_{crystal} \Delta T}{\rho\nu^2} \quad \approx \quad 1.7 \cdot 10^6 \tag{B.7}$$

$$Re_\omega = \frac{2\pi\omega R_{crystal}^2}{\nu} \quad \approx \quad 3.8 \cdot 10^3 \tag{B.8}$$

For the Grashof number, a temperature difference of $\Delta T = 30\,\mathrm{K}$ is used [38]. Comparison of the order of magnitude reveals a ratio between bouyancy and Marangoni forces of about 30, and a ratio of bouyancy and rotational forces of about 3[1]. This complies with the simulations of the three driving forces shown on figures 5.1, 5.2 and 5.4. Note for the 4" IKZ configuration at a 5 rpm rate of rotation that buoyancy is the dominating driving force, but since the rotational Reynolds number scales linearly with the rotation, the centrifugal forces are essential for the flow pattern at higher rates of rotation.

Finally the Reynolds number describes the convective momentum transfer to the viscous momentum transfer. A characteristic velocity is chosen to be $V = 1cm/s$

$$Re = \frac{V R_{crystal}}{\nu} \quad \approx \quad 1.5 \cdot 10^3 \tag{B.9}$$

Dopant transport

Of importance to the numerical simulation of dopant transport is the *solutal Peclét number* Pe_C, being the ratio of convective and diffusive species transport

$$Pe_C = \frac{V R_{crystal}}{D} \quad \approx \quad 1.5 \cdot 10^4 \tag{B.10}$$

The high value implies convective dominance giving numerical difficulties for the convective terms in the transport equation. Another effect of the convection dominated transport is high concentration gradients across streamline, since diffusive transport is slow.

[1] In comparing the rotational Reynolds number and the Grashof number Re_ω is squared to obtain the same denominator.

Appendix C

Stability and robustness of the numerical models

The examination of the stability and robustness of the numerical models provided in this appendix is not intended to be exhaustive or complete. It is included to illuminate some of the issues of the accuracy of applied numerical simulation.

The undoubtedly best way of validating or verifying a numerical model, is to compare it with the reality that it simulates, this is however difficult to do in a direct manner for the float zone process. Indirect verification can be done by comparing the shape of the lower phase boundary with LPS measurements or by comparing calculated resistivity profiles with measured ones. These are the primary verifications and they are provided within chapters 4 and 5. An indirect verification of the defect model is given in chapter 6 in the form of comparison with DLTS measurements. The purpose of this appendix is therefore to illustrate, that the results are robust and with the accuracy expected by the applied numerical models.

Conduction solution

The initial guess on the free surface is a straight line between the lower an upper triple points, as shown on figure 3.1, page 26, but because of the relative weak coupling between the electromagnetic and free surface models, the solution is insensitive to the initial guess.

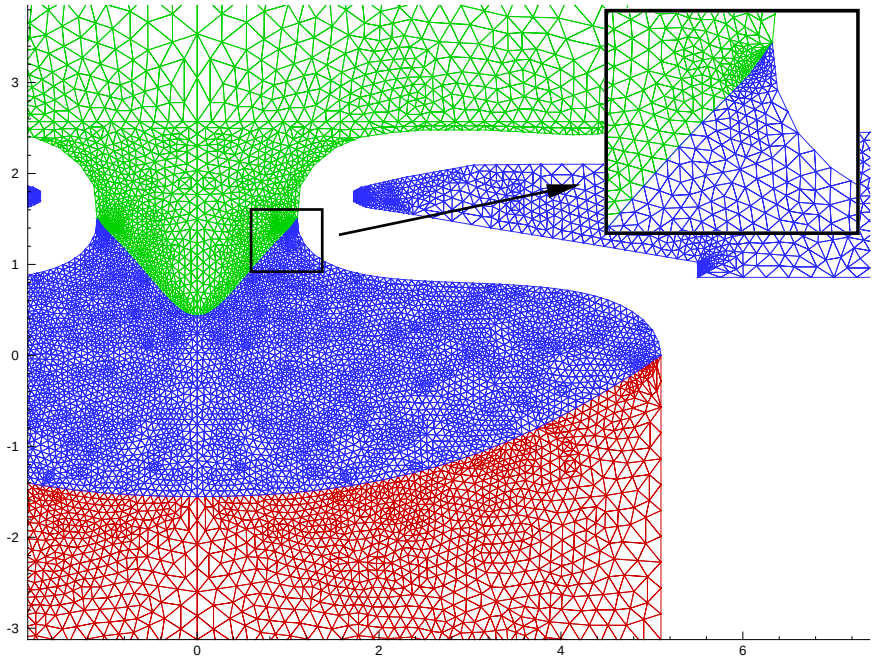

Figure C.1. *The mesh used for the heat transfer calculation of the IKZ 4" configurations. Green zone is feed, blue is melt and red is the crystal. The density is increased in the vicinity of the phase boundaries and at the ends of the free surface.*

The convergence criterion for the shape of the free surface is to run the iterations, until no change can be seen. With respect to the density of the boundary elements, the procedure used to find an optimum, was just to increase the density until no change could be seen.

The density of the mesh used in the *heat transfer* calculations is definitely of importance to the quality of the solution. Especially the upper phase boundary has to be refined, but also the areas at the end of the free surface, because of the change in boundary conditions. The mesh applied for calculation of the heat transfer for the IKZ 4" configurations is shown in figure C.1.

Melt convection

The stability of the melt convection calculations using MHAC has been tested by mesh-refinement studies and varying time step lengths. Note that implicit time stepping is used, so the time stepping is more stable then for instance with the dopant calculations, where

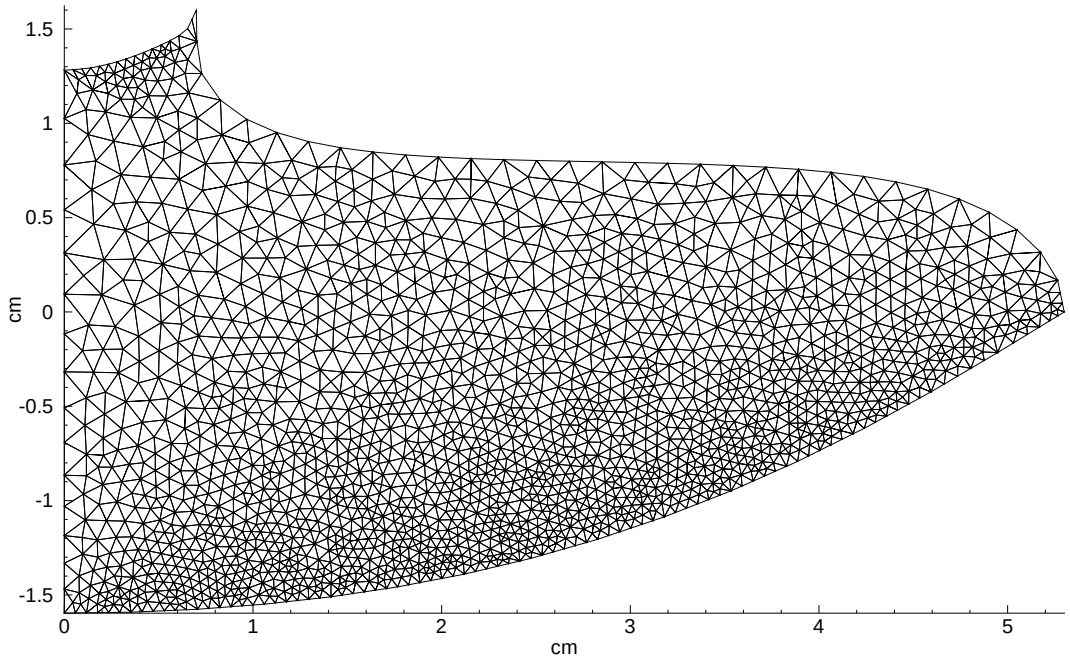

Figure C.2. *The mesh used for the melt convection calculation of the Topsil 4" configuration. The mesh consists of 3831 six-node triangles and 7816 nodes.*

explicit time stepping is used. The simulations delivered (input files) by Cape Simulation Inc, has been taken as a starting point and then the time stepping and mesh has been adjusted until no changes in the solution where found. The mesh used for calculation of the Topsil 4" configuration is shown in figure C.2, note that the triangles are six-node elements.

A time step of $\Delta t = 0.25\,\mathrm{s}$ is used, since the velocity field calculated by MHAC is used by FEM-CD, hence a velocity field is needed for every 0.25 s, as shall be shown in the next section.

Dopant transport

A substantial mesh refinement is required in order to resolve the concentration boundary layer in the dopant calculations. A minimum element size of less then 0.1 mm is recommended. The applied refinement algorithm is described in section 3.4.5, page 39. In principle the refinement procedure could be continued indefinitely, but using explicit time

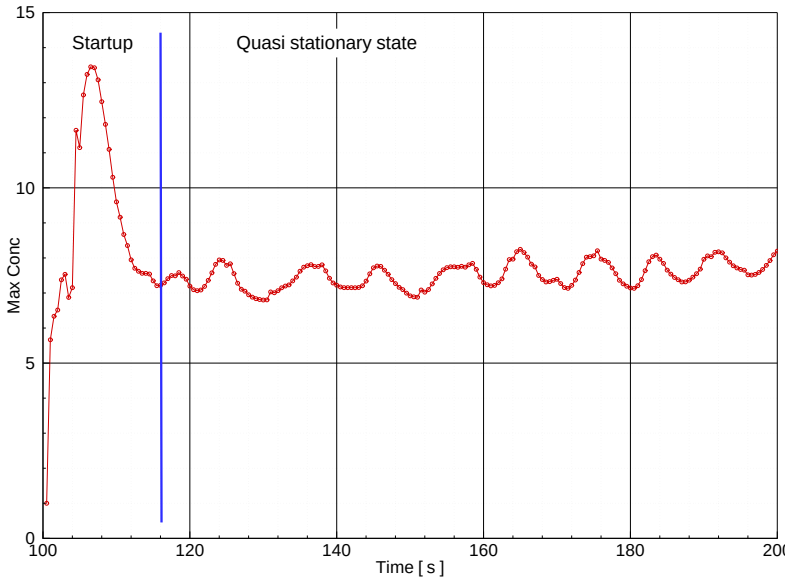

Figure C.3. *Buildup of the concentration boundary layer for the IKZ 4" - 10 rpm configuration, represented by the maximum concentration in the molten zone, which is on the lower phase boundary.*

stepping, this leads to stability problems, due to the requirements within the CFL (Courant-Friedrichs-Lewy) criterion (C.1), see [61].

$$\frac{v\Delta t}{L} < 1 \tag{C.1}$$

The significant area of the dopant transport is the concentration boundary layer, where for the Topsil 4" configuration the pull speed is $v = 0.0053\,\mathrm{cm/s}$ and the minimum element size is $L = 0.03\,\mathrm{mm}$, this results in a requirement that time steps are less then

$$\Delta t < \frac{0.003}{0.0053} = 0.56\,\mathrm{s}$$

A time step size of $\Delta t = 0.25\,\mathrm{s}$ is therefore applied.

The *startup of the calculation* is done be artificially increasing the time step size by a factor of 100. This gives inaccurate approximations to the convection, but speeds up the diffusion, and therefore the buildup of the concentration boundary layer. Figure C.3 shows the maximum concentration in the molten zone, which is somewhere on the lower phase boundary. It can be seen that the startup procedure actually overshoots, but that the convective transport out of the molten zone and into the crystal thereafter lowers the concentration to the quasi stationary level.

Index